SILICON PHOTONIC DEVICES FOR MICROWAVE SIGNAL GENERATION AND PROCESSING

By

Nasrin Ehteshami

Thesis submitted to the Faculty of Graduate and
Postdoctoral studies in partial fulfillment of the
requirements for the Master of Applied Science degree in
Electrical and Computer Engineering

Ottawa-Carleton Institute of Electrical and Computer Engineering
School of Electrical Engineering and Computer Science
Faculty of Engineering
University of Ottawa

uOttawa

ACKNOWLEDGMENTS

I would like to thank all the people who contributed in some way to the work described in this thesis.

First and foremost, I thank my academic advisor, Professor Jianping Yao for accepting me into his group, for the continuous support of my research by giving me intellectual freedom in my work, supporting my attendance at various workshops, engaging me in new ideas, and demanding a high quality of work in all my endeavors. His guidance helped me in all the time of research and writing of this thesis. I could not have imagined having a better advisor and mentor for my study.

I would also like to thank all of my colleagues who were working with me in the Microwave Photonics Research Laboratory at the department of Electrical Engineering and Computer Science, University of Ottawa. They provided a friendly and cooperative atmosphere at work and also useful feedback and insightful comments on my work.

I would like to acknowledge CMC Microsystems for providing the design tools and enabling the fabrication of silicon photonics chips through Institute of Microelectronics (IME) in Singapore and the Inter-university Microelectronics Centre (IMEC) in Leuven, Belgium.

Finally, I would like to acknowledge my family who supported me during my time here. First and foremost I would like to thank Mom, Dad, Brother and Sisters, for their constant love and support. Words cannot express how grateful I am to my family for all of the sacrifices that they've made on my behalf. Last but not the least, I would like to express appreciation to my beloved husband Vahid.

ABSTRACT

Silicon photonics as a one of the most promising photonic integration technologies has attracted many attentions in recent years. The major feature of this technology is its compatibility with complementary metal-oxide semiconductor (CMOS) processes which makes it possible to integrate optical and electronic devices in a same chip and reduce the cost significantly. Another reason of using silicon photonics is the high index contrast between the silicon core and silicon dioxide cladding which ensures the high density integration of photonic devices on a single chip. Monolithic integration with electronic and optical circuits makes silicon photonics technology suitable for numerous applications. One example is microwave photonics (MWP). MWP is an area that studies the interaction between microwave and optical signal for the generation, processing, control and distribution of microwave signals by means of photonics. Silicon photonics offers a reduction in footprint, losses, packaging cost and power dissipation in MWP systems.

This research in this thesis is focused on the design and fabrication of the silicon photonic devices for MWP signal processing and generation. Four MWP systems based on silicon photonic devices are proposed and experimentally demonstrated.

1) A single pass-band frequency-tunable MWP filter based on phase-modulation to intensity-modulation conversion in an optically pumped silicon-on-insulator (SOI) microring resonator (MRR) is designed and experimentally demonstrated. In the proposed filter, a phase-modulated optical signal is filtered by the SOI MRR, to have one first-order sideband suppressed by the MRR notch. The phase-modulated optical signal is converted to an intensity-modulated single-sideband (SSB) signal and detected at a photodetector (PD). The entire operation is equivalent to a single pass-band filter. The frequency tunability is achieved by tuning the resonance wavelength of the MRR, which is realized by optically pumping the MRR. A single pass-band MWP filter with a tunable center frequency from 16 to 23 GHz is experimentally demonstrated.

2) A broadband optically tunable MWP phase shifter with a tunable phase shift using three cascaded SOI MRRs that are optically pumped is designed and experimentally demonstrated. A microwave signal to be phase shifted is applied to an optical single-sideband (OSSB) modulator to generate an optical carrier and an optical sideband. The phase shift is introduced to the optical carrier by placing the optical carrier within the bandwidth of

one resonance of the three cascaded MRRs. The experimental results show that by optically pumping the cascaded MRRs, a broadband MWP phase shifter with a bandwidth of 7 GHz with a tunable phase shift covering the entire 360^{o} phase shift range is achieved.

3) A multi tap MWP filter with positive and negative coefficients using a silicon ring resonator modulator (RRM) is proposed and experimentally demonstrated. The RRM is designed and fabricated to operate based on the carrier depletion effect. The positive and negative coefficients are obtained by using opposite slopes of the modulation transmission response of the RRM. Two filter responses with two and three taps are experimentally demonstrated, showing the proof-of-principle for frequencies up to 18 GHz.

4) An approach to generate microwave signal based on enhanced four wave mixing (FWM) in an active silicon waveguide (SiWG) is studied. This SiWG is designed and fabricated, and the use of the active SiWG for MWP frequency multiplication to generate a frequency-sextupled millimeter-wave signal is experimentally demonstrated. Thanks to a reverse-biased p-n junction across the SiWG, the conversion efficiency of the FWM is improved, which leads to the improvement of the microwave frequency multiplication efficiency.

TABLE OF CONTENTS

LIST OF FIGURES

LIST OF TABLES

LIST OF ACRONYMS

CMOS	Complementary metal-oxide semiconductor
CW	Continuous wave
DSB	Double side band
EDFA	Erbium-doped fiber amplifier
ESA	Electrical spectrum analyser
FIR	Finite impulse response
FDTD	Finite time difference domain
FWM	Four-wave mixing
FSR	Free spectral range
FCD	Free-carrier dispersion
FCA	Free carrier absorption
FBG	Fiber Bragg grating
FDFD	Finite difference frequency domain
FWHM	Full width half maximum
GDS	Graphic database system
GC	Grating coupler
HNLF	Highly nonlinear fiber
IMEC	Inter-university Microelectronics Centre
IM	Intensity modulator
IME	Institute of Microelectronics
InP	Indium phosphide
IRR	Infinite impulse response
LD	Laser diode
MWP	Microwave photonics
MPF	Microwave photonic filter

MZM	Mach-Zehnder modulator
MRR	Micro ring resonator
MSMPF	Multiple-source microwave photonic filter
ODL	Optical delay line
OSA	Optical spectrum analyser
PLC	Planar light-wave circuits
PM	Phase modulator
PC	Polarization controller
RF	Radio frequency
SOI	Silicon-on-insulator
SOA	Semiconductor optical amplifiers
SCT	Separate carrier tuning
SPM	Self-phase modulation
SSB	Single side band
SIWG	Silicon waveguide
TPA	Two photon absorption
TLS	Tunable laser source
UWB	Ultra wide bandwidth
VNA	Vector network analyser
XPM	Cross phase modulation

CHAPTER 1 INTRODUCTION

1-1. Microwave photonics

Microwave photonics (MWP) [1] is an area that studies the interaction between microwave and optical waves for application such as radar, communications, sensor networks, warfare systems and instrumentation. In general, the MWP techniques cover the following topics: 1) photonic generation of microwave signals, 2) photonic processing of microwave signals, 3) photonic distribution of microwave signals, and 4) photonic analog-to-digital conversion [1]. An MWP system is implemented using a modulation device for electrical-to-optical (E/O) conversion, a photodetector (PD) that does the optical-to-electrical (O/E) conversion and functionalities between these two conversions (Fig.1.1). Some of the key functionalities in this case are time delay and phase shifting of microwave signals, frequency tunable and high selectivity microwave filtering, frequency up and down conversions and microwave waveform generations. Processing of microwave signal in optical domain has the advantages of the large bandwidth, low loss, small size, light-weight, immunity to electromagnetic interference (EMI) and the potential of large tunability and low-power consumption.

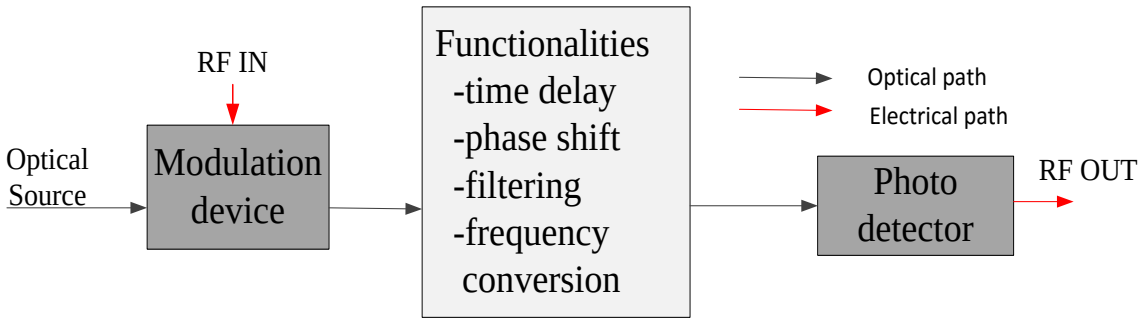

Fig.1.1: The MWP system basically consists of a modulation device for E/O conversion and a PD for O/E conversion. There are functionalities such as time delay, phase shift and filtering which connect two conversions.

The MWP has found widespread applications over the last 20 years. This applications include the generation, distribution, control and processing of the microwave signals. The earliest application for MWP technique was microwave signal distribution which an optical fiber was used as a replacement of coaxial cables in MWP links for connection between

modulators and detectors. Optical fibers have advantages in size, weight, loss and immunity to EMI over coaxial cables. Today, the MWP technique is used for antenna remoting (such as optically controlled beam-forming techniques for phased array antennas) and signal distribution to separate the signal processing core from the antenna, in this way, the signal processing part can be protected in case of antennas deployed in harsh environments.

Although microwave signal distribution is the main driver for MWP, other applications like microwave signal generation and processing have attracted much attention. The generation of the microwave signals and broadband waveforms are the latest development in MWP. The main attraction for signal generation using MWP technique is the large frequency tunability and generation of ultra-wide bandwidth microwave signal. Filtering, tunable true time delay and wideband phase shifting of microwave signals are important issues in microwave signal processing [2],[3]. Implementation of MWP processors for optical beam-forming and phase array antenna systems can be obtained by combining these basic functionalities.

Most of MWP systems are implemented using discrete components, such as lasers, modulators and detectors. Using the discrete components makes the system bulky and complicated and reduces the system reliability and leads to the higher power consumption in the system. Also, the use of discrete components increases the system price since each component will bear packaging cost. These problems can be resolved with photonic integration [4], [5] which provides a reduction in footprint, losses, packaging cost and power dissipation in MWP systems [6]. Potential for photonic integration offers the prospect for low-cost, reliable and energy-efficient MWP systems, on the other hand leads to increasing speed, component counts as well as incorporating as much functionalities (active and passive) in a single chip/technology platform [7-9].

In the past 20 years, three platforms have been frequently used to demonstrate integrated MWP functionalities. They are indium phosphide (InP), silica planar light-wave circuits (PLCs) and silicon-on-insulator (SOI) [6]. The propagation loss in InP passive optical waveguide is higher than SOI based waveguides, thus, semiconductor optical amplifiers (SOAs) should be used in InP based MWP circuits to compensate the losses, but the noise added from the SOAs might limit the MWP system functionality. In MWP systems that are based on silica PLCs, the lowest propagation loss can be achieved on a waveguide with a low

refractive index contrast of 0.7%. This low contrast value leads to the large bending radius and thus, larger chip size which is less attractive for photonic chip integration. In SOI platform a waveguide with extreme low loss down to 0.8dB/cm can be achieved [10], also, the strong optical confinement due to the high index contrast between silicon (n=3.45) and SiO_2 (n=1.45) allows for sharp bending and guarantees the high density integration of photonic devices on a single chip. Among these three available platforms, we focus on the SOI platform for MWP applications in this thesis.

1-2. Silicon photonics

Silicon photonics is the technology of signal generation, processing, transmission and detection where the signal is carried by light in silicon-based components. The complementary metal-oxide semiconductor (CMOS)-compatible SOI substrates excited the development of research activities in silicon photonics. The strong optical confinement in SOI platform allows tight bending in optical waveguide thus making feasible high density integration. Such a high optical confinement in the SOI platform with desirable properties such as high third-order optical nonlinearities enables functionalities like amplification, modulation, lasing, and wavelength conversion.

The past 15 years have seen significant increase of silicon photonics implementation in MWP systems. The following are a few examples of silicon based devices for MWP applications; optical passive components such as rib and strip waveguides, directional couplers, Y branch, microring resonators (MRRs) and Mach-Zehnder interferometers (MZIs), and active optoelectronic components such as modulators, detectors and sometime light sources. Compact silicon modulators based on Mach-Zehnder (MZ) interferometers and microring resonators (MRRs) utilizing the free carrier plasma effect have been demonstrated by Intel [11] and Cornell [12], respectively. Germanium can be grown directly on the SOI wafer to make Ge-on-Si detectors [13]. Nowadays, all the major silicon-based components have been implemented with acceptable performance except light sources. Silicon is usually known as a poor light-emitting material because of its indirect band gap. An optically pumped silicon-based Raman lasers have been demonstrated in [14] in which the power dissipation and efficiency are very low. In the next chapter we will review the most advances in silicon photonics technology for MWP applications.

1-3. Outline of this thesis

Chapter 1: This introduction was aimed at giving a general description of the microwave photonics technique and silicon photonics.

Chapter 2: The background review of important silicon photonic designs which have been proposed up to now to address different MWP applications are presented.

Chapter 3: The fundamental of the SOI passive design including silicon waveguide, directional coupler, and ring resonator are given. A high quality factor SOI MRR is designed and experimentally tested to implement a tunable single pass-band MWP filter. In the proposed filter, a phase-modulated optical signal is filtered by the SOI MRR, to have one first-order sideband suppressed by the MRR notch. The phase-modulated optical signal is converted to an intensity-modulated single-sideband (SSB) signal and detected at a photodetector (PD). The entire operation is equivalent to a single pass-band filter. The frequency tunability is achieved by tuning the resonance wavelength of the MRR, which is realized by optically pumping the MRR.

Chapter 4: Three cascaded MRRs is designed and experimentally tested to implement a tunable MWP phase shifter. A microwave signal to be phase shifted is applied to an optical single-sideband (OSSB) modulator to generate an optical carrier and an optical sideband. The phase shift is introduced to the optical carrier by placing the optical carrier within the bandwidth of one resonance of the three cascaded MRRs. The experimental results show that by optically pumping the cascaded MRRs, a broadband MWP phase shifter with a tunable phase shift covering the entire 360^{o} phase shift range is achieved.

Chapter 5: The main physical mechanism used for optical modulation in silicon is studied. A ring resonator modulator (RRM) is designed and fabricated by embedding a lateral P-N junction in the silicon rib waveguide. A multi tap MWP filter with positive and negative coefficients using the RRM is designed and experimentally demonstrated

Chapter 6: An approach to perform microwave frequency multiplication based on enhanced four wave mixing (FWM) in an active silicon waveguide (SIWG) is studied. This SIWG is designed and fabricated, and the use of the SIWG for MWP frequency multiplication to generate a frequency-sextupled millimeter-wave signal is experimentally demonstrated.

Chapter 7: The summary and future works are given.

CHAPTER 2 BACKGROUND REVIEW OF SILICON PHOTONIC DESIGN FOR MICROWAVE PHOTONIC APPLICATIONS

2-1. SOI based microwave photonic applications

As mentioned earlier in Chapter 1, the MWP applications divided to four categories 1) photonic generation of microwave signals, 2) photonic processing of microwave signals, 3) photonic distribution of microwave signals, and 4) photonic analog-to-digital conversion. Most of the advances in silicon photonics for MWP applications have been focused on photonic processing of microwave signals (which have enabled filtering, tunable true time delay and wideband phase shifting of microwave signals), and photonic generation of microwave signals. Here, we focus on these two applications to show recent development in SOI based devices for MWP applications.

2-1.1 Microwave photonic filter

Fig. 2.1 shows a general layout of a microwave photonic filter. The radio frequency (RF) to optical conversion is achieved by modulating either a single continuous wave (CW) source or a CW source array. Then the modulated signal is sent to an optical subsystem which samples the signal in the time domain using optical delay lines and other photonic elements. At the output, the resulting signal is sent to the receiver producing the output RF signal ($S_o(t)$).

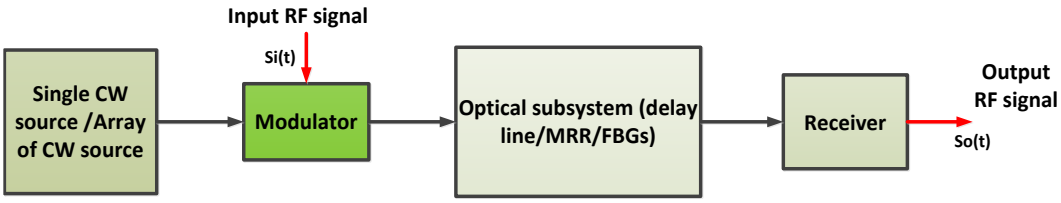

Fig.2.1: General layout of a MWP filter (FBGs: Fiber Bragg Gratings)

The most powerful approach for the implementation of MWP filters is that based on discrete time signal processing [15] where a number of weighted and delayed samples of the RF signal are produced in the optical domain and combined upon detection. In particular, finite impulse response (FIR) filters combine a finite set of delayed and weighted taps of the input optical signal (a RF-modulated optical carrier) at their output while infinite impulse response (IRR) are based on an infinite number of weighted and delayed taps of the input optical signal [16]. For an example the transfer function of FIR filter is given by

$$H(f_{RF}) = \sum_{k=0}^{N-1} a_k e^{-j2\pi k f_{RF} T} \qquad (2\text{-}1)$$

where a_k represents the weight of the sample, N is the number of samples and T the time delay between consecutive samples implies that the filter is periodic in the frequency domain. The period, known as free spectral range (FSR) is given by $f_{FSR} = 1/T$. MWP filters can also operate under coherent and incoherent regime. In the incoherent regime the basic delay T is much greater than the coherence time of the optical source that feeds the filter while in the coherence regime is much smaller. Spectral response can be compressed or stretched by changing T. This is a technique usually used for tuning the notch or pass-band positions of an MWP filters.

One of the key components in the MWP filter structure (Fig.2.1) is the optical subsystems. Several SOI based photonic subsystems have been reported [17-42]. A fully reconfigurable fourth-order RF photonic filter on SOI platform with a tunable 3-dB bandwidth of 0.9–5 GHz, more than 38 dB optical out-of-band rejection, FSR up to 650 GHz, and compact size was demonstrated in [17]. The filter architecture is shown in Fig.2.2 (a). Each unit cell is a Mach-Zehnder interferometer (MZI) and a feedback loop (in this case, a racetrack resonator) that is coupled to the MZI arm using a tunable coupler. The use of ring resonator enables a reduction in size, weight and power of each unit cell, and a large number of these unit cells, can be cascaded on a single chip.

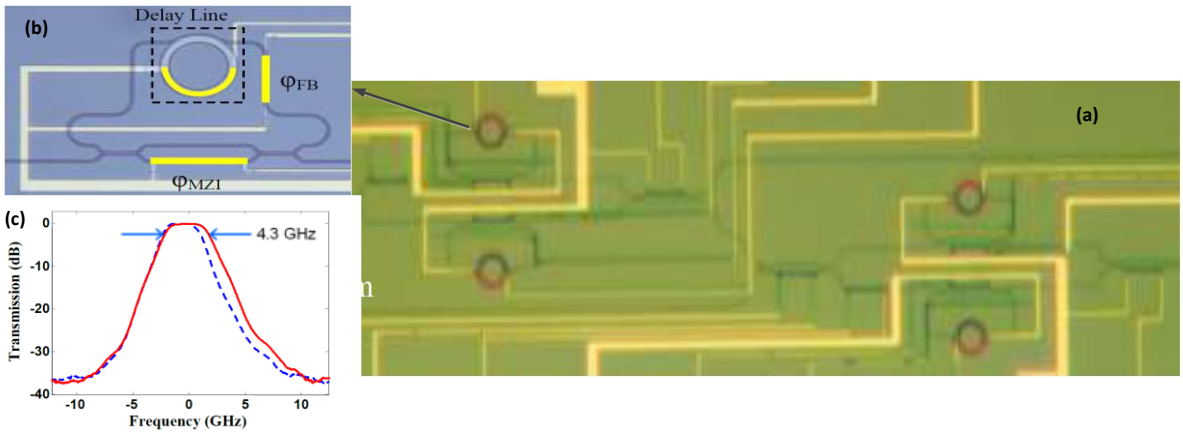

Fig.2.2: (a) optical micrograph of the fourth-order cascade filter implemented by cascading two second-order unit cells. (b) Zoom in view of each unit cell including a racetrack resonator embedded in MZI structure, (c) Band-pass filter response shows the flat top, the blue (dashed) curve shows that the bandwidth can be fine-tuned without affecting the other parameters of the response [17].

In [18] a tunable and reconfigurable pass-band microwave photonic filter based on an integrated optical processor was demonstrated on a SOI substrate. The optical processor based on micro-rings, MZI, and Y-branches (Fig.2.3.) were utilized to produce two pass-band responses for separately processing optical carrier and sideband. Fig. 2.4 shows that the operating frequency and 3-dB bandwidth of filter could be tuned from 18 to 40 GHz and from 4 to 15 GHz, respectively.

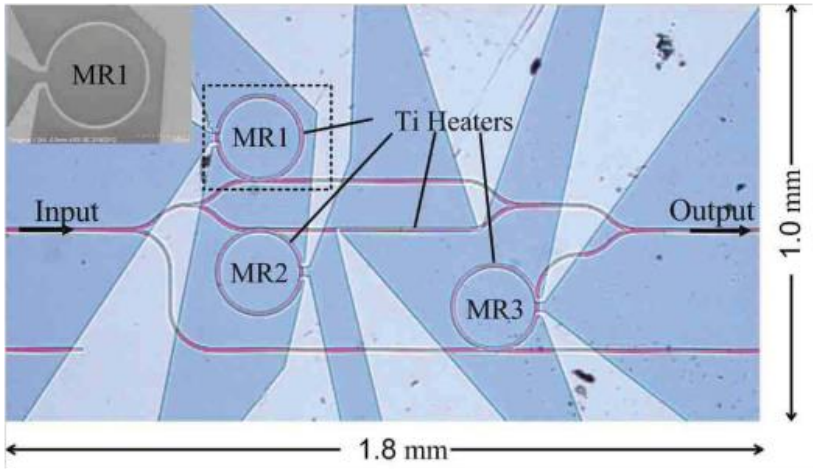

Fig.2.3: Optical micrograph of the proposed optical processor. (MR: microring) [18]

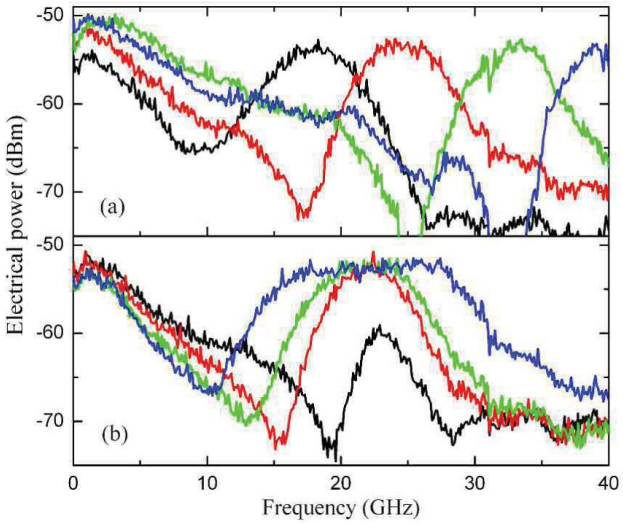

Fig.2.4: (a) Tunable center frequency from 18 to 40 GHz with the 3-dB bandwidth of ~5 GHz. (b) Tunable bandwidth from 4 to 15 GHz while maintaining center frequency of ~22 GHz [18].

Most of the high-order silicon ring filters typically have bandwidths larger than 100 GHz. In some MWP application a flat band-pass and narrow 3 dB bandwidth is necessary. In [19]1-2 GHz-bandwidth filters with very high extinction ratios (~50 dB) was demonstrated based on mutually coupled silicon ring resonator. Mutually coupled resonators have the ability to produce higher-order filter responses with a flat-top. Each ring of a filter was thermally controlled by metal heaters placed on the top of the ring (Fig.2.5). 3dB bandwidth of 1.9 GHz experimentally was achieved as shown in Fig.2.6. In another demonstration [20] a fully-reconfigurable fourth-order silicon optical lattice filter was implemented by cascading unit cells including an MZI and an MRR. The experimental results showed a notch filter with 400 MHz notch width.

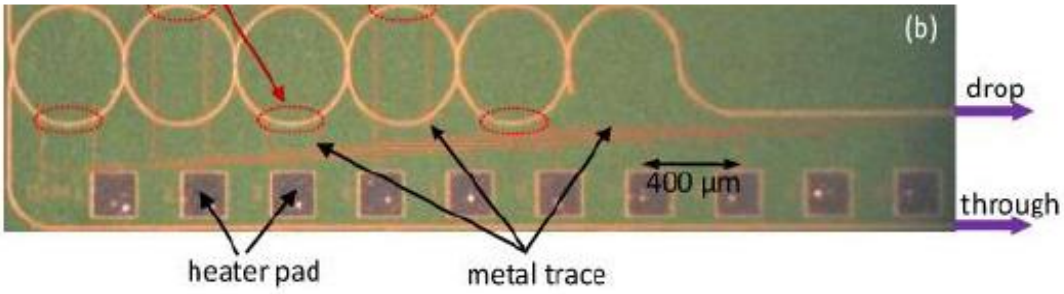

Fig.2.5: Image of the fabricated filter [19].

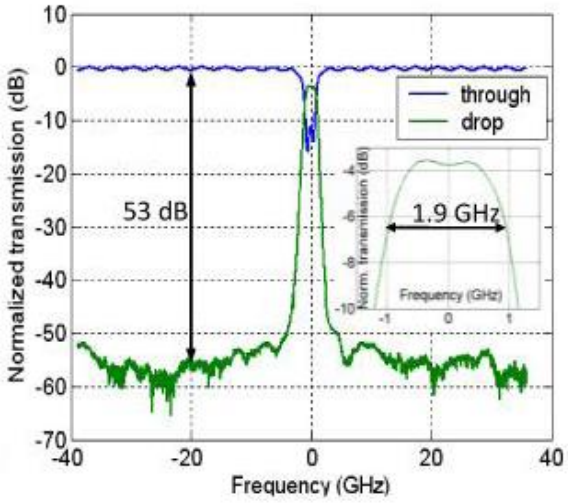

Fig.2.6: Transmission spectra for the 5th-order ring filter [19]

A novel photonic microwave filter implementation based on an asymmetric SOI based Mach-Zehnder modulator (MZM) was demonstrated in [21]. The asymmetry of the MZM has been utilized to achieve positive and negative filter coefficients. Active performance was based on a reverse biased P-N junction that was incorporated in the shorter arm of the MZM as shown in Fig.2.7 (a). Two filter responses with two and three taps were experimentally demonstrated as shown in Fig. 2.7 (b) and (c), respectively.

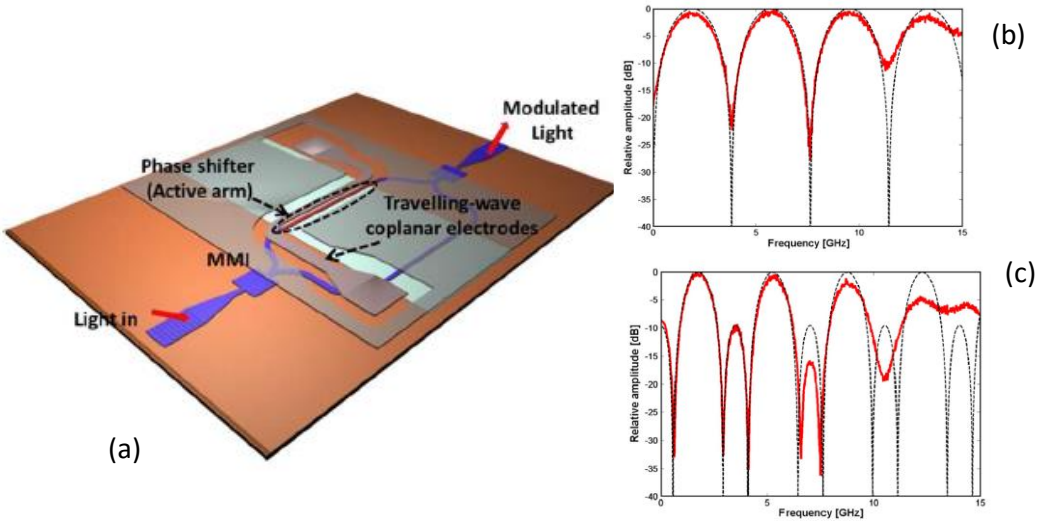

Fig.2.7: (a) Schematic of the silicon Mach-Zehnder modulator for implementing the MWP filter, (b) two-tap response, (c) three-tap response .The solid line represents the experimental results and the dotted the theoretical estimation [21].

2-1.2. Delay line and phase shifter

Optical delay lines (ODL) and wideband tunable phase shifters have substantial importance in some MWP signal processing applications such as optical beam-forming and MWP filter. In 1997 Yegnanarayanan et al. [22] demonstrated the first optical delay line in SOI for true time-delay phased array antenna. They used eight-channel 3μm wide waveguides with a time delay of 12.3ps measured over 2-20GHz frequency range. An electronically tunable optical true-time delay line was proposed in [23], this delay line utilized the combination of apodised gratings and the free-carrier plasma effect to tune the delay of silicon waveguides at a fixed wavelength. The device showed a tuning ranges as high as ~660 ps with a loss of < 2.2 dB when operated in the reflection mode of the gratings. An integrated delay lines based on tapered Bragg gratings in SOI rib waveguides was presented in [24]. A tuning range of 450 ps was achieved using the thermo-optical effect.

Besides delay, phase shifting is also attractive for a number of signal processing applications. Burla et al. [25] demonstrated the separate carrier tuning (SCT) scheme together with optical single sideband filtering monolithically integrated in a single chip. The SCT unit worked as a phase shifter in the system. The SCT unit which was implemented using a pair of cascaded optical ring resonators (ORRs) is shown in Fig 2.8 (a). By adjusting the position of its resonant frequency with respect to the carrier wavelength (2.8(b)), RF phase shift up to 360^{o} was obtained over a less than 2GHz bandwidth (2.8(c)).

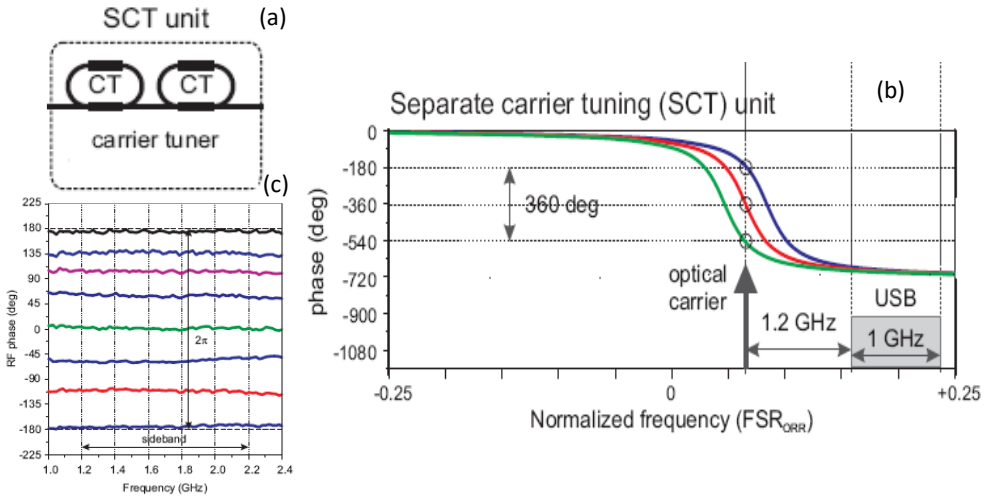

Fig.2.8: (a) separate carrier tuning unit, (b) the phase response, (c) measured RF phase shift. (USB: upper side band) [25]

An electrically tunable MWP phase shifter using a single SOI-MRR or two cascaded SOI-MRRs with a phase shift of 204° or 360° at 40 GHz was demonstrated in [26, 27]. The phase tuning was implemented using an embedded micro-heater. Since the phase shift was achieved at a single frequency, the phase shifter in [26, 27] was, in fact, a true time delay line. In [28], an all-optically tunable MWP phase shifter with a phase shift of 260º was achieved by using a single passive MRR. The tuning was realized by utilizing the thermal nonlinear effect due to two photon absorption (TPA) in the silicon waveguide. The advantage is that no micro-heater is needed, which simplifies the design. However, due to the limited phase tuning range, it is difficult to realize a full 360° phase shift using a single MRR.

2-1.3. Microwave signal generation

The focus of recent research in microwave signal generation is on generating ultra-wide bandwidth (UWB) RF waves and extremely stable and pure microwave carriers. Recently, an integrated ultra-broadband arbitrary microwave waveform generator that incorporates a fully programmable spectral shaper fabricated on a silicon photonic chip was demonstrated in [29]. The spectral shaper was implemented using eight cascaded MRRs, each having a slightly different resonant wavelength on a silicon photonics platform. The resonance wavelengths could be tuned by micro heater. The typical bending radius was 5μm and the waveguide propagation loss was around 3.5dB/cm. The principle of this photonic arbitrary microwave waveform generation system is shown in Fig. 2.9. The input light source was a mode-locked and amplified femtosecond laser, which had a broadband spectrum. The spectral shaper was used to modify the spectrum emitted from a mode-locked laser. Frequency-time mapping was achieved with 5.5 km of optical fiber, and then optical signal converted to the electrical domain using a high-speed photodetector (PD).

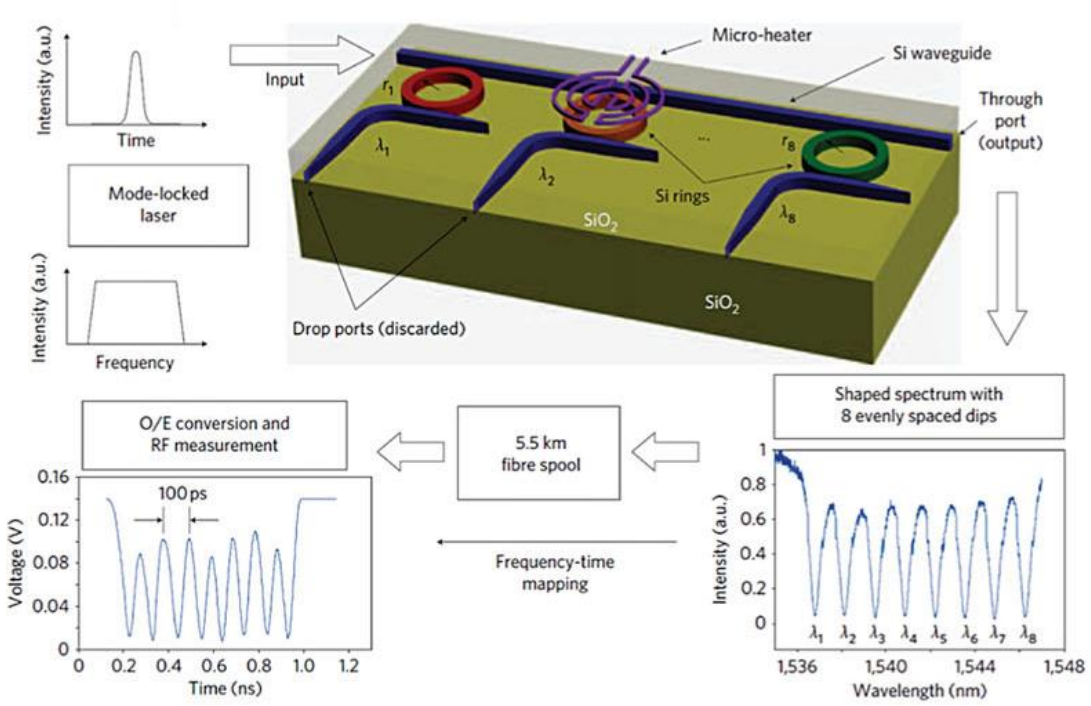

Fig.2.9: On-chip arbitrary waveform generation using cascaded of 8 MRR resonators in SOI platform [29].

A photonic-assisted microwave signal generator based on a silicon MRR modulator was demonstrated in [30]. A PN junction was embedded in the MRR cavity. The DC component of the modulated light was trapped in the cavity, while the high-order sideband components were able to exit the cavity and then generate microwave signals at new frequencies. Experimental results showed that a 10 GHz microwave signal was converted to a 20 GHz signal in the optical domain with an electrical harmonic suppression ratio of 22 dB. Fig. 2.10(a) presents a schematic diagram of the microwave signal generation system. A cross section of the rib waveguide forming the ring is shown in Fig. 2.10 (b). The rib waveguide was embedded with a lateral PN junction whose doping concentration was $1.5 \times 10^{18}/cm^3$. The two ohmic contact regions of the PN junction were heavily doped to $1 \times 10^{20}/cm^3$. The etching depth was 160 nm and the dimension of the rib waveguide accommodating the PN junction was 450 nm × 220 nm.

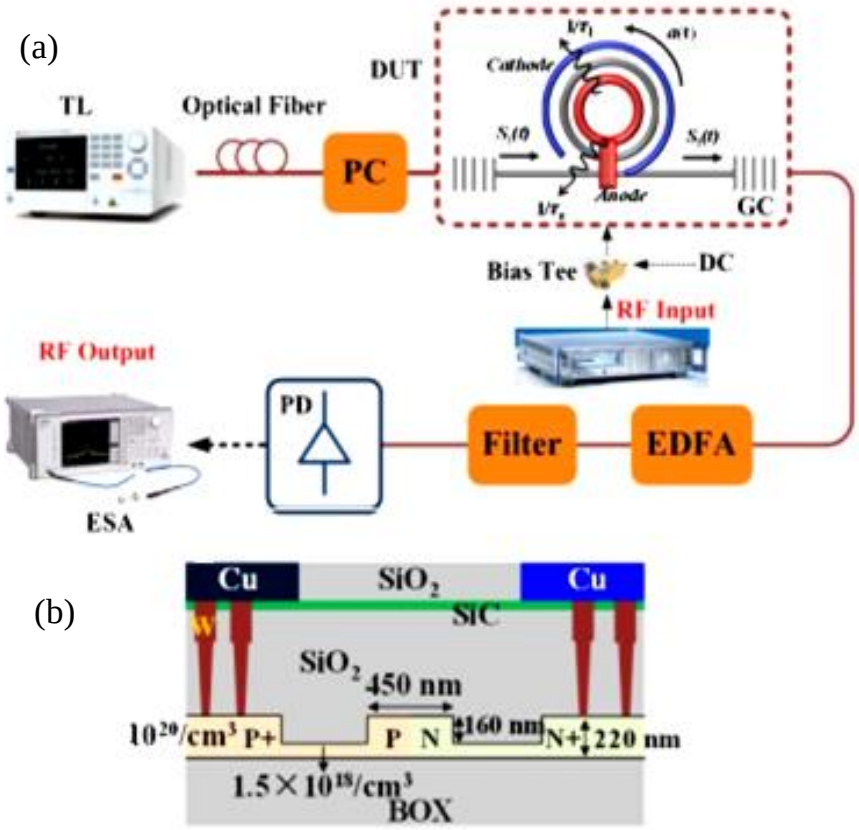

Fig.2.10: (a) Schematic diagram of a typical microring cavity in the microwave signal generation system. (b) Cross section of rib waveguide. TL, tunable laser; PC, polarization controller; DUT, device under test; GC, grating coupler; DC, direct current; EDFA, erbium-doped fiber amplifier; ESA, electrical signal analyzer. Optical fiber is represented by solid lines and the electrical path is represented by dashed lines [30].

2-2. Other emerging applications

On chip microwave frequency conversion is another technique that recently received increasing interest. In this approach, RF frequency mixing for signal up-conversion and down-conversion is performed in a silicon photonic integrated circuit. In [31] the RF mixer was realized in silicon electro optical MZM enhanced via slow-light propagation. An up-conversion from 1 GHz to 10.25 GHz was demonstrated. A summary of some integrated MWP demonstrations based on SOI platform since 2005 until mid-2015 is shown in Table 1.1.

2-3. Objective of this research

Most of the reported MWP filters [18-23] were based on MZMs. In this research an SOI based ring resonator modulator (RRM) is designed to implement a multi tap MWP filter. Compared to MZMs, RRM offers plenty of advantages such as compact footprint, low driving voltage and ultra-low power consumption. Most of the reported MRR based phase shifters [25-28] suffer from insufficient phase shift or narrow bandwidth. Here, we have designed a wide band full 360^{o} MWP phase shifter based on three cascaded MRRs. We also have utilized the nonlinear four-wave mixing (FWM) effect in silicon for MWP signal generation. In addition, the nonlinear thermo-optic effect in silicon is used to add tunability to the passive MWP filter and phase shifter.

Table1.1. Reported results for MWP demonstrations based on SOI platform

Year	Functionality	Key component	Reference
2005	Delay line	Photonic crystal	[32]
2007	MWP filter	MRR, MZI	[33],[34]
2010	Delay line	MRR	[35]
2010	MWP filter	MZI	[36]
2010	MWP filter	MRR	[37]
2012	UWB generator	MRR	[38]
2012	Delay line	Resonator	[39]
2013	MWP filter	MRR	[40]
2014	RF phase shifter	MRR	[41]
2015	RF generator	MRR	[42]

2-4. Silicon photonic design procedure

A complete development process of any silicon photonic structure can be split into four basic steps: design (including modelling, simulation and analysis), mask generation, fabrication and characterization, which are explained in the following sections.

2-4.1. Design

First, we tried to model the performance of the device under study. In silicon based devices due to high index contrast between core and cladding the analytical approach is not the only modeling procedure of photonic structures. In this case, we simulated the device under study to analyze its performance. We have employed the following computational tools to study the behaviour of our designs: the finite difference time domain (FDTD), the finite difference frequency domain (FDFD) and interconnect. In the case of electro-optic modulators design, semiconductor device simulation is used to simulate the electrical structures besides the optical modelling.

2-4.2. Mask generation

We derived appropriate design parameters from the modelling and simulation process. We then generated the mask design for the fabrication. Usually, a set of photonic structures are designed varying the parameters in a wide range. The graphic database system (GDS) generates final file of the mask which finally is sent to the fabrication foundry. Final GDSs corresponding with this research work are shown in Fig. 2.11. The active design (Fig.2.11 (a)) consists of ring modulator, phase modulator, active silicon waveguide, cascaded ring modulator with phase modulator and a Mach-Zehnder modulator. The passive design (Fig.2.11 (b)) includes single and cascaded MRRs with different parameters.

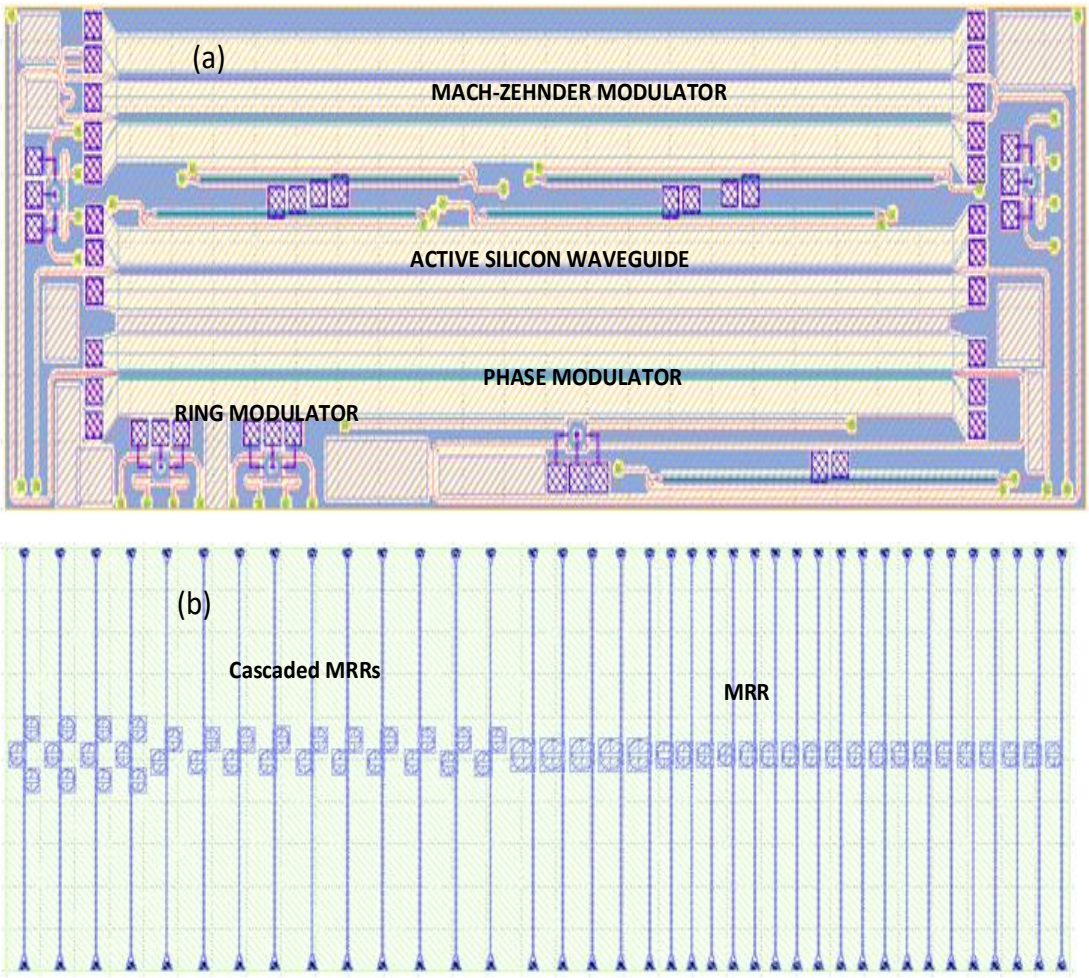

Fig.2.11: Final GDS corresponding to this research work, (a) active design, (b) passive design

2-4.3. Fabrication

For this research, the first silicon photonics foundry services were offered by IMEC (formerly the Inter-university Microelectronics Centre; in Leuven, Belgium). The fabrication process for passive and active silicon photonic process was included using 193nm and 248 nm deep-UV lithography, respectively. The active design was fabricated in the Institute of Microelectronics (IME) in Singapore. The most common impurities used to dope silicon were boron and phosphorus, which are respectively situated in the III column and V column of the periodic table. The dopants implants for the modulators were performed on the exposed silicon, prior to any oxide fill. This was followed by a rapid thermal anneal at 1030 °C for Si dopant activation. The image of the fabricated chips is shown in Fig. 2.12.

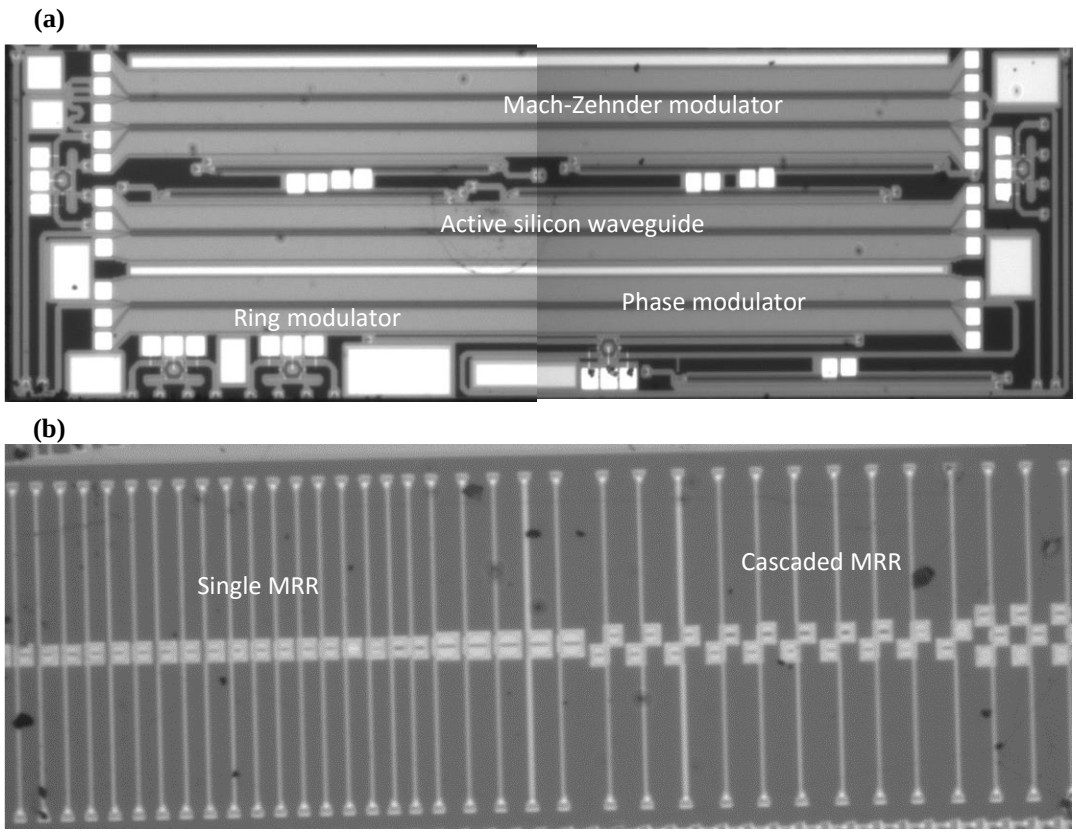

Fig.2.12: Image of the fabricated chips corresponding to this research work, (a) active design, (b) passive design

The general procedure for silicon photonic design has been summarised in Fig. 2.13.

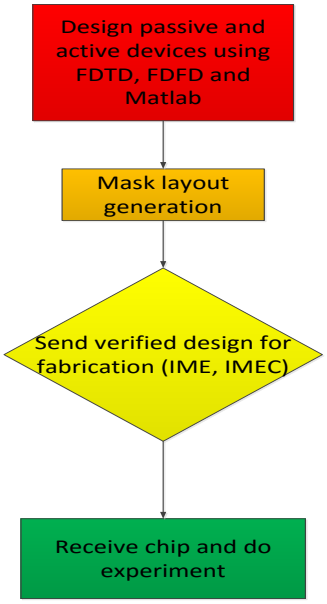

Fig.2.13: Graphical overview of a silicon photonic design workflow, starting from the simulation of the devices, the mask layout generation, verification, fabrication and testing.

CHAPTER 3 AN SOI BASED MICRORING RESONATOR FOR A SINGLE PASS-BAND MICROWAVE PHOTONIC FILTER

3-1. Silicon-on-insulator

The wafers commonly used for silicon photonics are termed silicon-on-insulator (SOI). The typical wafer consists of a 725 μm silicon substrate, 2 μm of oxide (buried oxide, or BOX), and 220 nm of crystalline silicon, as shown in Figure 3.1. The 220 nm thickness has become a standard used in particular by multi project wafer foundries (e.g. IMEC and IME). The height of the BOX layer should be at least 1 μm to ensure minimal substrate leakage losses.

The refractive index wavelength dependence of silicon and silicon dioxide should be considered to describe the dispersion effects. Fig. 3.2 shows the wavelength dependence of the refractive index at a room temperature for both silicon and silicon dioxide using the models determined by Li [43] and Tan and Arndt [44]. Most of the light is confined in the silicon and the silicon dioxide dispersion and temperature dependence does not play an important role in the performance of silicon photonic circuits.

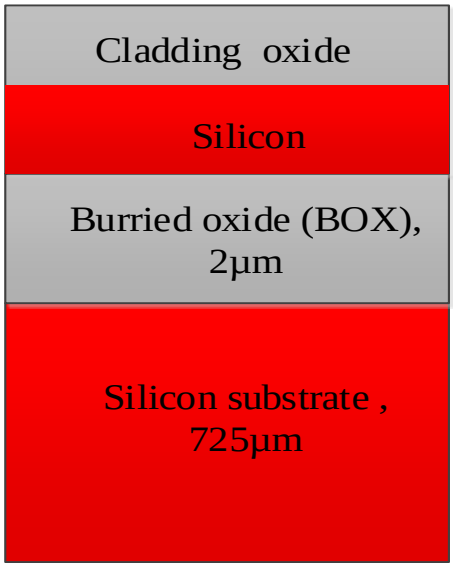

Fig. 3.1: Cross-sectional view of silicon-on-insulator (SOI) wafer.

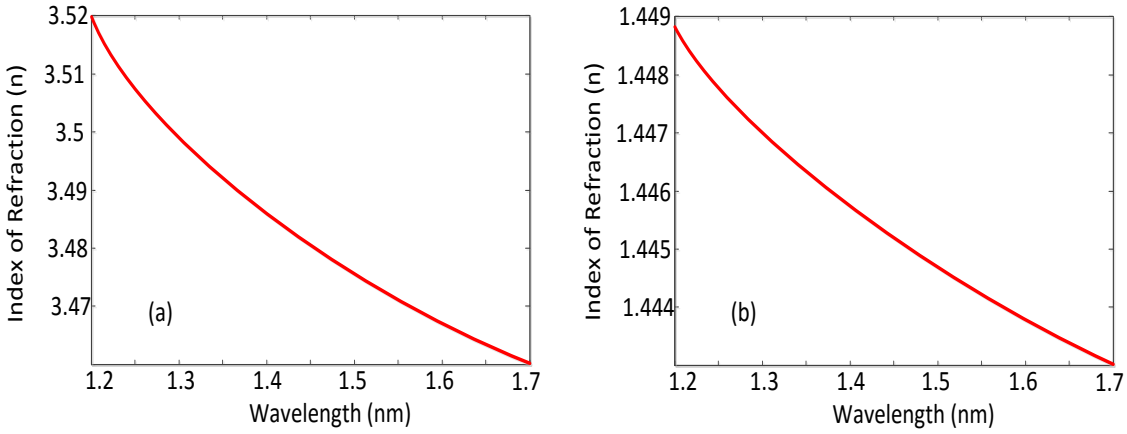

Fig.3.2: Refractive index of (a) silicon and (b) silicon dioxide versus λ at room temperature (T=300K) [43], [44]

3-2. SOI waveguide

The propagation loss in SOI waveguides has a large variation depending on the waveguide dimensions and processing conditions. There are two types of waveguides commonly used in silicon photonics technology: rib and strip waveguides (Fig.3.3). The rib waveguides exhibit relatively low-losses down to 1-2 dB/cm, but limited in bending radius to hundreds of micrometers [45]. Strip waveguides on the other hand show higher losses in the order of 2-3 dB/cm [46] but they allow ultra-compact devices in the order of a few micrometers due to the tight bending radius. Silicon strip waveguide (Fig.3.4) is a basic and crucial component in photonic integrated circuits. The light is guided in the waveguide through total internal reflection and its confinement is largely determined by the refractive index between the waveguide core and the surrounding cladding. The SOI material provides very high refractive index contrast and makes it possible to confine the light tightly to a silicon waveguide. To ensure single mode propagation and low propagation loss, the waveguide core height and width must be carefully chosen.

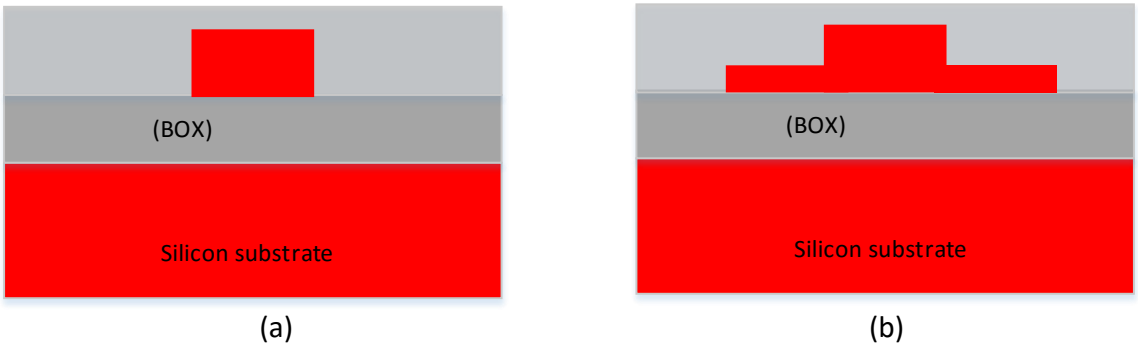

Fig.3.3: Common waveguides in silicon photonics. (a) Strip waveguide, (b) Rib waveguide

If the waveguide width is too large, the higher order modes leak into the silicon dioxide layer because the higher order modes have an effective index closer to that of the silicon dioxide. If the waveguide width is too small, none of the modes can be guided and all of the light radiates into the surrounding media. The silicon thickness is typically constrained to what is available by the foundry (SOI thickness of 220 nm, or etched silicon with a 90 nm thickness). For the given thickness, we find a suitable waveguide width to support only a single TE and TM waveguide mode. Bogaerts [47] measured the propagation losses versus waveguide width with a fixed height of 220 nm as shown in Table 3.1. For width=500nm the propagation loss reaches to the minimum value, also the strip waveguide becomes single mode for TE polarization when the waveguide width is between 550 nm and 440 nm in the wavelength range around 1550 nm. The propagation losses exponentially increase with decreasing waveguide width due to weaker confinement of the optical mode. The strong confinement of light in sub-micrometer SOI waveguides allows sharp bends to be created.

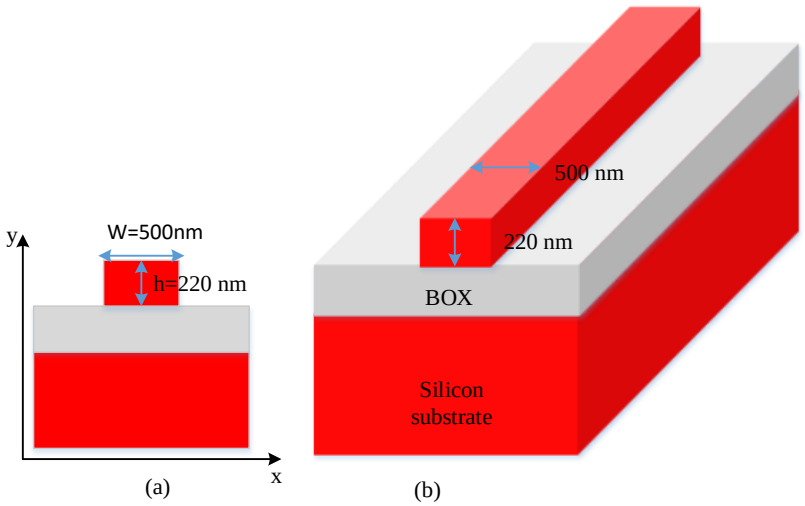

Fig.3.4: Cross-sectional view of silicon-on-insulator (SOI) strip waveguide with air cladding, (a) 2D view, (b) 3D view

Table 3.1: Propagation losses versus waveguide width [47]

Width (nm)	Propagation loss (dB/cm)
400	34± 1.7
440	9.5±1.8
450	7.4±0.9
500	2.4±1.6

Fig. 3.5 shows that how effective index change versus wavelength for different waveguide widths. The effective index decreases with an increase in wavelength for two main reasons: 1) the refractive index of the material decreases with wavelength and 2) the optical mode confinement decrease when the wavelength increases. The effective index increases with an increase in waveguide width because the optical mode confinement increases. Fig.3.6 shows the simulation result of the fundamental mode profile for strip waveguide (500nm×220nm) with a TE-like polarization, the field and energy is strongly confined inside the waveguide, although about 10% of the field is in the cladding. This is the mode used for most silicon photonics devices.

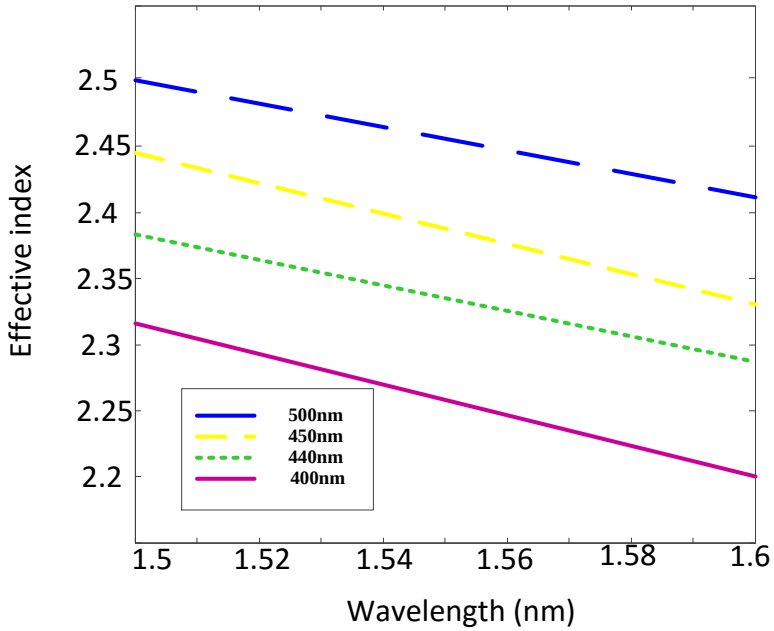

Fig.3.5: Simulation results of the effective index in the strip waveguide versus wavelength, for a silicon thickness of 220 nm, for various waveguide widths.

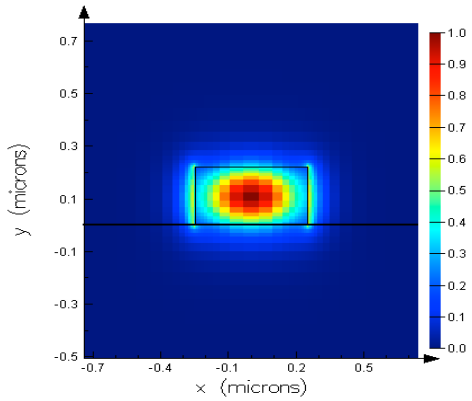

Fig. 3.6: Simulation results of TE (first mode) mode profile of a 500 × 220 nm strip waveguide at 1550 nm, effective index mode is n_{eff} = 2.44.

3.3. Directional coupler

The directional coupler is the most common method of splitting and combining light in photonic systems. The directional coupler consists of two parallel waveguides, where the coupling coefficient is controlled by the length of the coupler and the spacing between the two waveguides (Fig. 3.7). The behaviour of a directional coupler can be found using coupled mode theory [48]. The fraction of the power coupled from one waveguide to the other can be expressed as:

$$k^2 = \frac{P_{cross}}{P_0} = \sin^2(C.L) \tag{3-1}$$

where P_0 is the input optical power, P_{cross} is the power coupled across the directional coupler, L is the length of the coupler, and C is the coupling coefficient. The fraction of the power remaining in the original through waveguide can be expressed as:

$$t^2 = \frac{P_{through}}{P_0} = \cos^2(C.L) \tag{3-2}$$

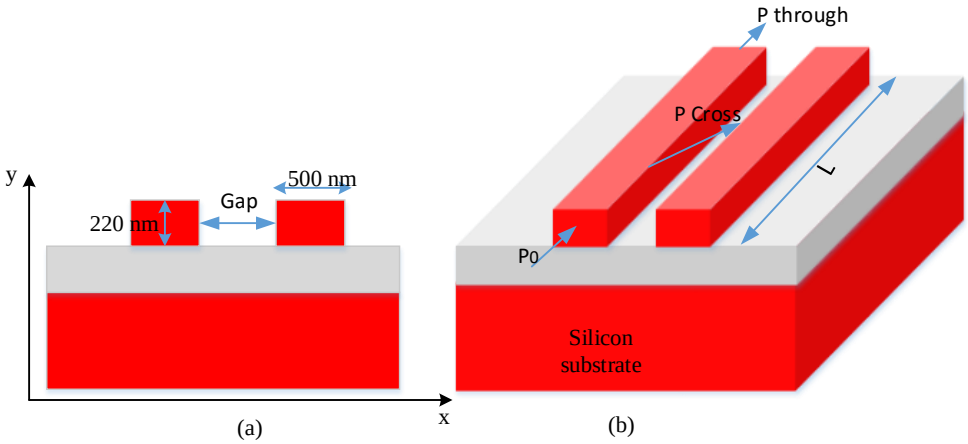

Fig.3.7: Schematic of the SOI directional coupler, (a) 2D view, (b) 3D view

To obtain the coupling coefficient, we use super-mode analysis, to calculate the effective indices (n_1 and n_2) of the two eigen-modes of the coupled waveguides. These two modes, is shown in Fig. 3.8, are known as the symmetric and anti-symmetric super-modes. From these two super-modes, the coupling coefficient is found:

$$C = \frac{\pi \Delta n}{\lambda} \tag{3-3}$$

where Δn is the difference between the effective indices ($n_1 - n_2$) and is calculated using a 2DFD mode solver. All simulations are for a fixed waveguide width and height of 500 nm and 220 nm, respectively. The propagation constant of the two modes are given by:

$$\beta_1 = \frac{2\pi n_1}{\lambda} \tag{3-4}$$

$$\beta_2 = \frac{2\pi n_2}{\lambda} \tag{3-5}$$

When the modes travel along the directional coupler, the field intensity oscillates between the two waveguides. With the two modes in phase, the power is placed in the first waveguides. After a π phase shift difference between two modes, the power becomes localized in the second waveguide. This occurs after a distance called the cross-over length, *Lx*, and is found by:

$$\begin{aligned} \beta_1 L_x - \beta_2 L_x &= \pi \\ L_x[\frac{2\pi n_1}{\lambda} - \frac{2\pi n_2}{\lambda}] &= \pi \\ L_x &= \frac{\lambda}{2\Delta n} \end{aligned} \tag{3-6}$$

Fig. 3.9 shows the difference between the effective indices (n_1-n_2) versus wavelength for gap distances of 200 nm, 300 nm, 400 nm, and 500 nm. As expected, the difference between n_1 and n_2 decreases with increasing gap distance. Also, n_1 is greater than n_2 since the odd mode is less confined. Once the waveguides are sufficiently far apart, the difference between n_1 and n_2 becomes effectively zero, which corresponds to an infinite L_x.

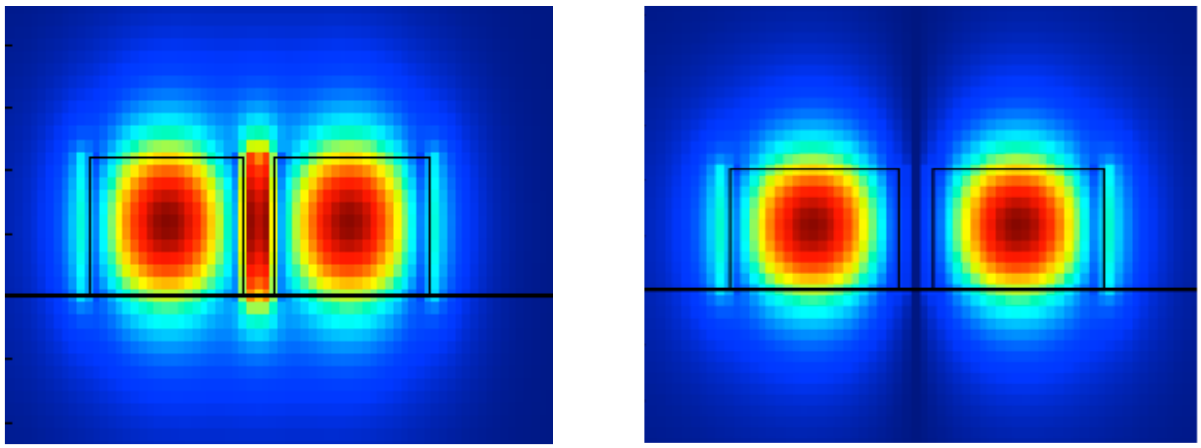

Fig.3.8: Simulated result of two fundamental modes of a directional coupler. (a) Symmetric mode. (b) Antisymmetric mode. The asymmetric nature of the 2nd mode profile is evident in the zero-crossing in the centre of the gap. λ = 1550 nm, coupler gap = 200 nm, waveguide dimension: 500 nm × 220 nm.

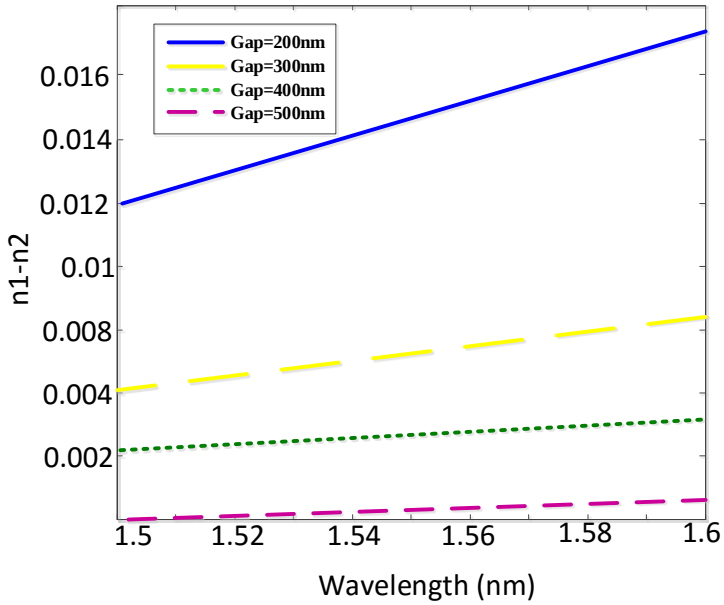

Fig. 3.9: Simulated result for difference between the effective index versus wavelength for gap distances of 200 nm, 300 nm, 400 nm, and 500 nm.

We can calculate the field coupling coefficient (k) using (3-1) for any directional coupler gap or length (L is the coupler length) as:

$$k = [\frac{P_{coupled}}{P_0}]^{1/2} = \left|\sin(\frac{\pi \Delta n}{\lambda}.L)\right| \tag{3-7}$$

If we assume there is no loss in the coupling region, we can write

$$\left|k\right|^2 + \left|t\right|^2 = 1 \tag{3-8}$$

where $|t|^2$ and $|k|^2$ are the power transmission factor and power coupling factor, respectively. Fig. 3.10 shows numerical results for the power coupling factor and power transmission factor versus coupling length for a fixed gap distance of 200 nm. For coupling length equal 20 µm a 50-50 directional coupler can be achieved. Also, the cross over length (L_x) for the gap variation from 50 nm to 300 nm is calculated and the result is shown in Fig. 3.11(a). If the gap distance decreases, the length at which total power transfer occurs will decrease. Fig. 3.11(b) shows the cross over length versus wavelength for gap=200nm.

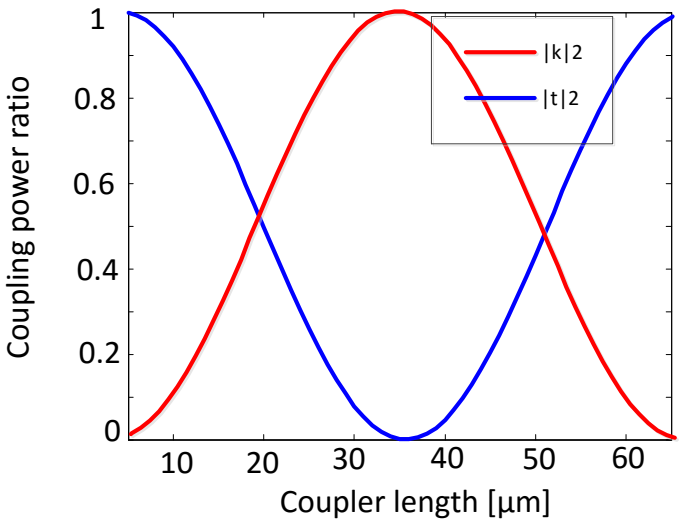

Fig. 3.10: Simulated results for coupling power ratio versus coupling length (L), gap distance = 200 nm, and λ = 1550 nm.

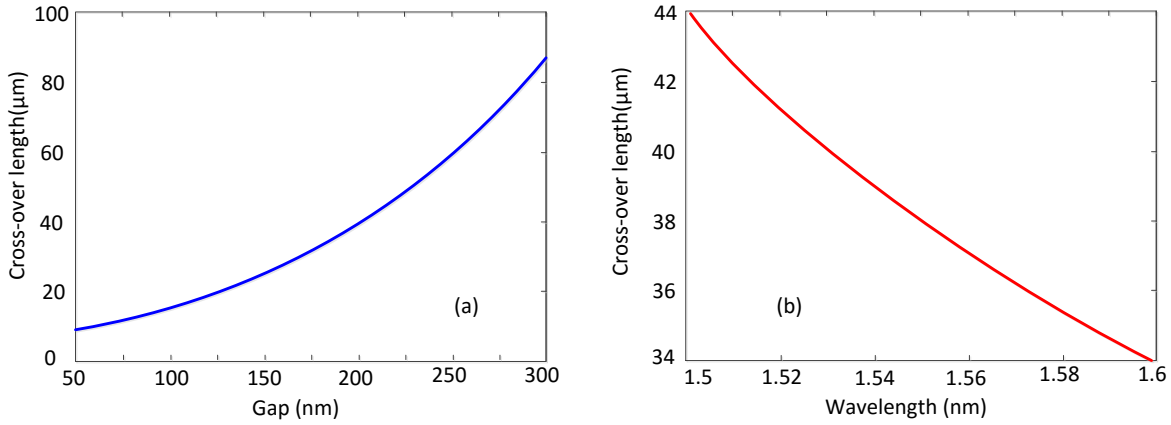

Fig.3.11. Calculations for a strip waveguide directional coupler, 500 × 220 nm. (a) Cross-over length, *Lx*, versus gap space, λ=1550 nm, (b) Wavelength-dependence of the cross-over length for gap = 200 nm.

3.4. Ring resonator

The MRR can be treated as a round waveguide coupled to a straight waveguide. Fig. 3.12 shows a MRR that is coupled to a straight bus waveguide. The optical input E_{i1} travels along the upper straight waveguide and enters the coupling region which is modeled with the lossless coupling matrix [49]

$$\begin{vmatrix} E_{t1} \\ E_{t2} \end{vmatrix} = \begin{vmatrix} t & k \\ -k^* & t^* \end{vmatrix} \begin{vmatrix} E_{i1} \\ E_{i2} \end{vmatrix} \tag{3-9}$$

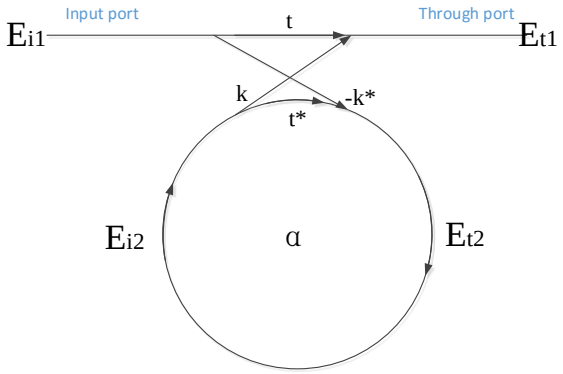

Fig.3.12: Model of a single ring resonator with one waveguide

The $*$ denotes the conjugated complex value of t and k, respectively. A portion of the input wave is coupled into the resonator to form a travelling wave that circulates clockwise around the ring. During a single round-trip, the circulating wave is diminished, due to intrinsic optical losses, by an attenuation factor $a = \exp(-\alpha L/2)$ where α is the attenuation coefficient in the ring and L is the total circumference of the ring. Using (3-9) the ratio of the transmitted and incident field in the bus waveguide is given by

$$\frac{E_{t1}}{E_{i1}} = \left[\frac{t - a\exp(j\varphi)}{1 - ta\exp(j\varphi)} \right] \tag{3-10}$$

$t^2 + k^2 = 1$ for lossless coupling. $\varphi = \beta L$ is the round-trip phase change of the ring and β is the propagation constant ($\beta = kn_{eff} = \frac{2\pi}{\lambda} n_{eff}$), where n_{eff} is the effective refractive index of the waveguide and λ is the wavelength. We find the ring to be on resonance when the phase φ is a multiple of 2π. The total phase shift of the transmitted light for one ring is given by

$$\phi = \pi + \varphi + \arctan\left(\frac{t\sin\varphi}{a - t\cos\varphi} \right) + \arctan\left(\frac{at\sin\varphi}{1 - at\cos\varphi} \right) \tag{3-11}$$

By squaring (3-10), we obtain the intensity transmission T_n as follow,

$$T_n = \left|\frac{E_{t1}}{E_{i1}}\right|^2 = \frac{a^2 - 2ta\cos\phi + t^2}{1 - 2at\cos\phi + (ta)^2} \tag{3-12}$$

When the ring resonator is coupled to two waveguides, the incident field is partly transmitted to the drop port (Fig 3-13). Transmission to the pass and drop port can be obtained as follow

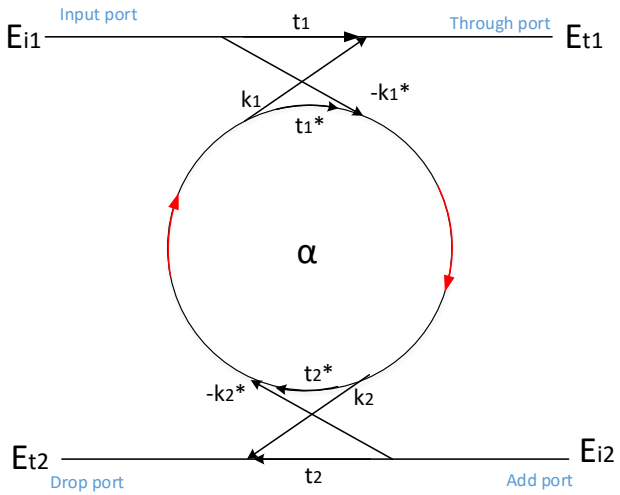

Fig. 3.13: Model of an add-drop MRR with two waveguide

$$T_d = \frac{E_{t1}}{E_{i1}} = \frac{t_1^2 a^2 - 2t_1 t_2 a\cos\phi + t_1^2}{1 - 2at_1 t_2\cos\phi + (t_1 t_2 a)^2} \tag{3-13}$$

$$T_p = \frac{E_{t2}}{E_{i1}} = \frac{(1-t_1^2)(1-t_2^2)a}{1 - 2at_1 t_2\cos\phi + (t_1 t_2 a)^2} \tag{3-14}$$

The transmission function (T_n, T_p and T_d) is shown in Fig. 3.14. The wavelength distance between two resonances or free spectral range (FSR) in function of wavelength equals:

$$FSR = \frac{\lambda_{res}^2}{n_g L} \tag{3-15}$$

The group index takes into account the dispersion of the waveguide and is defined by

$$n_g = n_{eff} - \lambda_{res}\frac{dn_{eff}}{d\lambda} \tag{3-16}$$

The quality factor (Q-factor) is a measure of the sharpness of the resonance relative to its central frequency,

$$Q-factor=\frac{\lambda_{res}}{FWHM} \tag{3-17}$$

λ_{res} is the resonance wavelength and FWHM is the full width at half maximum of the resonance spectrum and for an all-pass ring resonator equals [49]

$$FWHM=\frac{(1-ta)\lambda_{res}^2}{\pi n_g L\sqrt{ta}} \tag{3-18}$$

In (3-12) by setting $t=a$ internal losses are equal to the coupling losses. The transmitted power becomes zero ($T_n=0$), this is known as the critical coupling condition. At critical coupling, the phase response jumps abruptly. By setting $t<a$ the MRR works in over-coupled condition. Compared with the critical-coupling case, the transmission is broadened and the notches are much shallower; the total phase change across one FSR is 2π, but with a reduced slope, which corresponds to a smaller group delay. For under-coupling ($t>a$) condition the phase shift near the resonance shows a strong decrease [49].

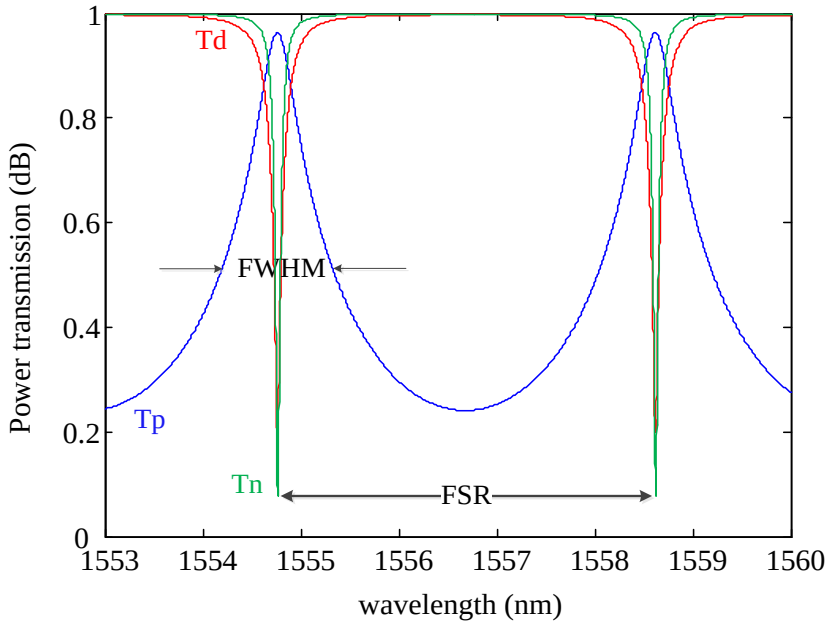

Fig.3.14: Numerical result for transmission spectrum of an all-pass ring and the two outputs of add-drop ring with the important spectral features indicated. a = 0.94, t1=t2=t=0.9. Because of the additional losses introduced by the second coupling section, the add-drop ring has a broader resonance.

3-4.1. Racetrack resonator

To control the coupling parameters we have used a racetrack resonator instead of the ring resonator as shown in Fig. 3.15. There is a parallel length (L) between resonator and bus waveguide. Transmission and phase response at the through port of the racetrack for varying coupling coefficients is shown in Fig. 3.16. Here, we assume the diameter of the ring is 30µm, the effective group index of the SOI waveguide is 4.26 and the ring works in over coupling condition. By increasing the coupling coefficient the notch depth and the slope of the phase response in resonance wavelength will reduce. In next sections, for the sake of simplicity the notation "MRR" has been used for all types of resonator (ring and racetrack).

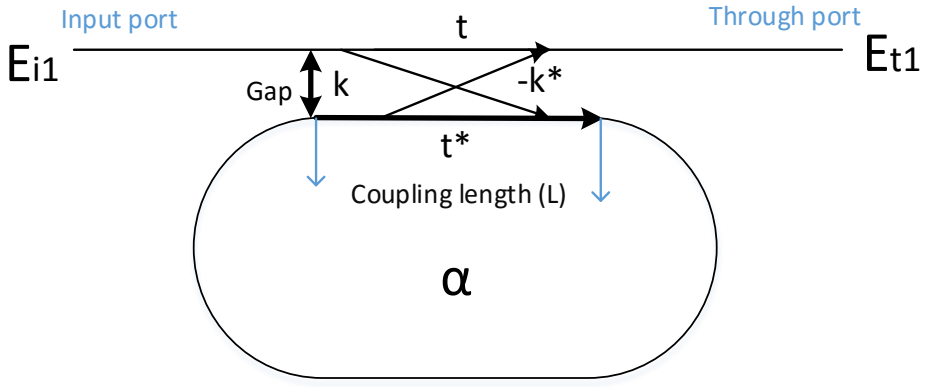

Fig.3.15: Schematic of the racetrack resonator

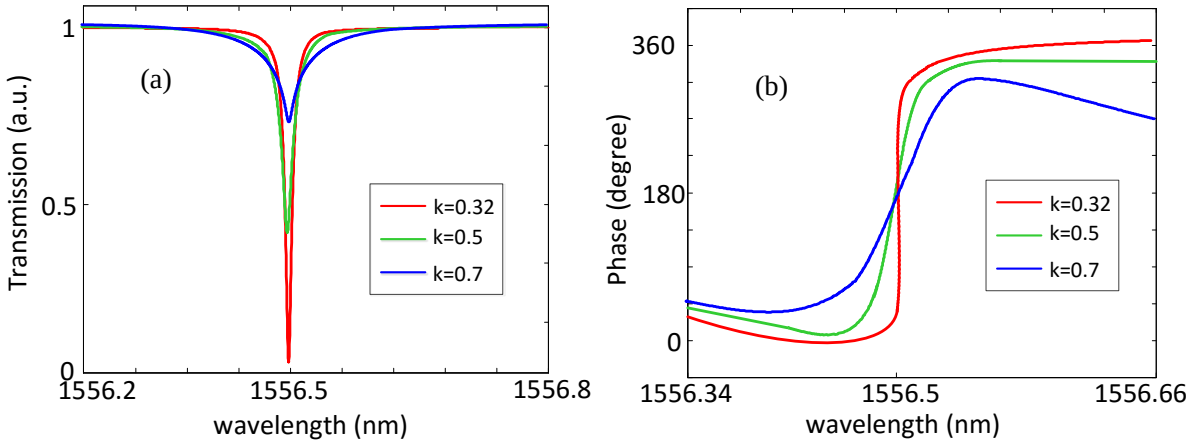

Fig. 3.16: Transmission and phase response at the through port for varying coupling coefficients. (*a*~0.997, R=30µm, L=10µm).

3-4.2 High Q-factor MRR design

MRR with a very high Q factor can be used directly for filter applications. For proper design and optimization of a high-quality resonator, several aspects have to be considered. Q-factor can be rewritten as a function of the physical parameters of an all-pass ring resonator [49]:

$$Q - factor = \frac{\pi n_g L \sqrt{ta}}{\lambda_{res}(1-ta)} \tag{3-19}$$

And for an add-drop ring resonator:

$$Q - factor = \frac{\pi n_g L \sqrt{t_1 t_2 a}}{\lambda_{res}(1-t_1 t_2 a)} \tag{3-20}$$

The Q-factor represents the number of oscillations of the field before the circulating energy is depleted to 1/*e* of the initial energy. In order to increase the Q-factor, it is crucial to reduce the losses in the cavity. The round trip loss as well as coupling loss in the directional couplers is loss factors that need to be reduced to obtain high-Q MRR. Therefore an all-pass resonator will exhibit a higher Q-factor than an add-drop resonator (when both devices operate close to critical coupling). The Eq. (3-19) shows that a higher Q is obtained for large *L* and small cavity loss, but these two terms are not independent since the accumulated propagation loss increases with the cavity length. Propagation loss is set to 2.7dB/cm (corresponding to waveguide losses in a silicon wire with air cladding in the IMEC fabrication process). Our design is based on all pass MRR with 30µm radius and coupling length of 10µm. The numerical result for Q factor versus wavelength for different gap distance is shown in Fig.3.17. As the gap increases, coupling coefficient decreases (*t* increases) which causes an increase in Q-factor. A MRR with the following parameters has been simulated using Mode software and the results are shown in Fig. 3.18. The transmission response for the MRR with R=30µm, L=10µm and gap=280nm is shown in Fig. 3.18 (a) the Q-factor reach around 10^5. With decreasing the gap distance to 240nm the Q factor decreases to 9000 (Fig.3.18 (b))

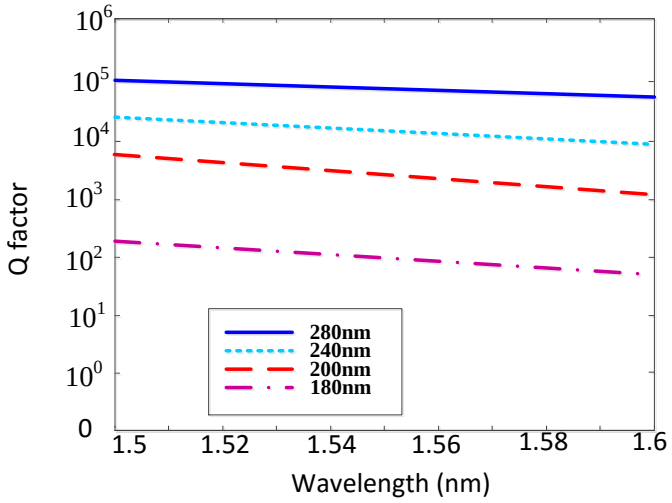

Fig.3.17: Numerical result for Q factor versus wavelength for different gap distance. (R=30µm, coupling length=10µm)

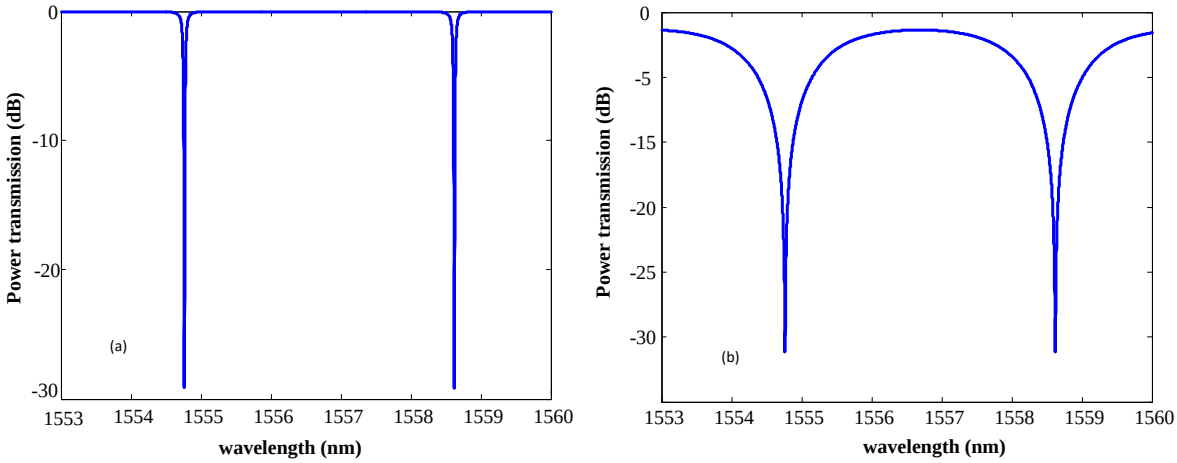

Fig.3.18: Transmission response for the designed MRR (a) Q=10^5, (b) Q=9000

Fabrication process includes a technique (corner analysis) that considers typical process variations for each parameter. For example, the thickness of the SOI layer may be specified as 220 nm, with a ±10 nm variation. Similarly, other fabrication parameters have variations, such as ring radius, coupling length, gap distance and waveguide width. Image of the fabricated MRRs is shown in Fig 3.19, which shows MRRs with different variations. Two grating couplers are incorporated to couple the light into the MRR from a single mode fiber and out of the MRR to another single mode fiber.

Most of the silicon-based devices need an interface between the input and the single-mode optical fibers. In our design, we have used a grating coupler for all of the device inputs. In a grating coupler, the fundamental mode from the silicon waveguide is first expanded laterally by an adiabatic taper into a waveguide of about 10 μm width. This width is match with the mode size of an optical fiber on the y axis as shown in Fig 3.20. The light is then coupled out by the diffraction of shallow-etched gratings into the optical fiber. For most of the grating couplers, the optical fiber is orientated with an angle θ of about 10°. This is to avoid the large second-order Bragg back reflection [50].

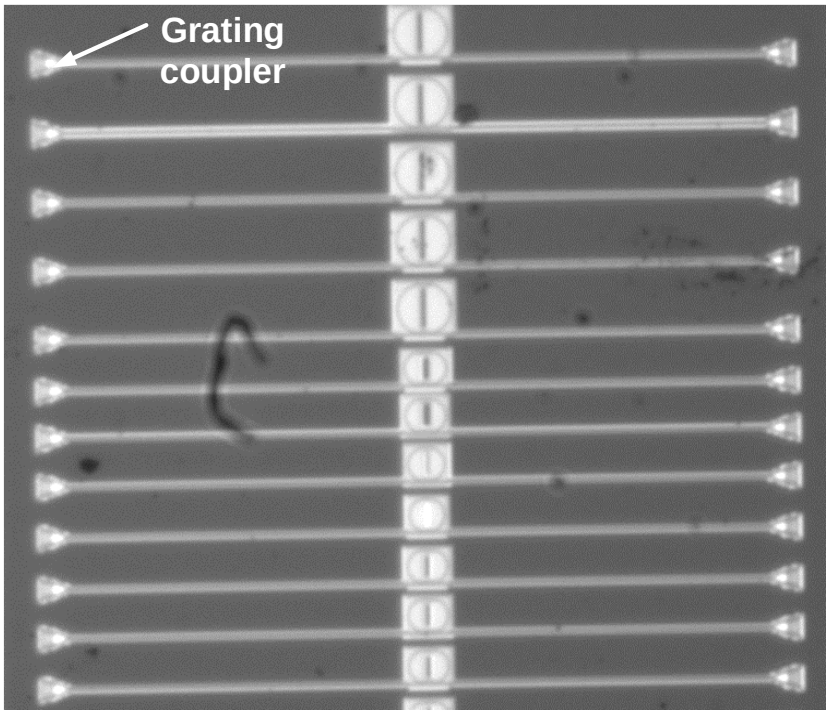

Fig.3.19: Image of the fabricated MRR with different variation in coupling length, radius and gap

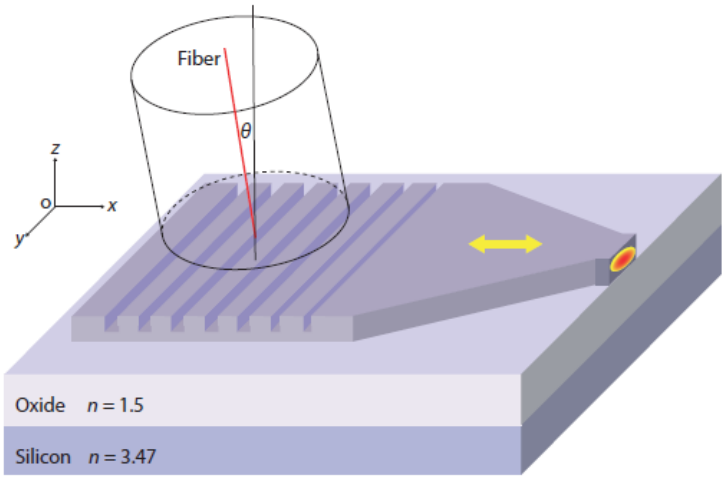

Fig. 3.20: Schematic of a waveguide grating coupler between an optical fiber and silicon waveguide. θ is the angle of the fiber axis to the surface normal of the SOI wafer, and the yellow arrow shows the direction of light propagation [50].

3-5. Experimental setup to measure the transmission response of the MRR

Fig. 3.21 shows the experimental setup that we used in our lab to measure the MRR transmission response. A signal from a broad band source has been sent to the input of the MRR through the polarization controller (PC). We adjust the PC to ensure that the input signal to the MRR is TE polarized. Fig.3.22 shows how the single mode fiber coupled into and out of the MRR. The MRR output is then sent to the optical spectrum analyser (OSA). The measured MRR transmission response is shown in Fig 3.23. As you can see the insertion loss in 1550nm is about 25dBm. Two main factors limit the coupling efficiency of grating couplers and leads to high insertion loss. First is the poor directionality of grating diffraction. Second one is the mode mismatch between the field profiles of the diffracted light from the waveguide gratings and the fiber mode. Because the coupling coefficient is a wavelength-dependent parameter, the notch depth has been changed with wavelength.

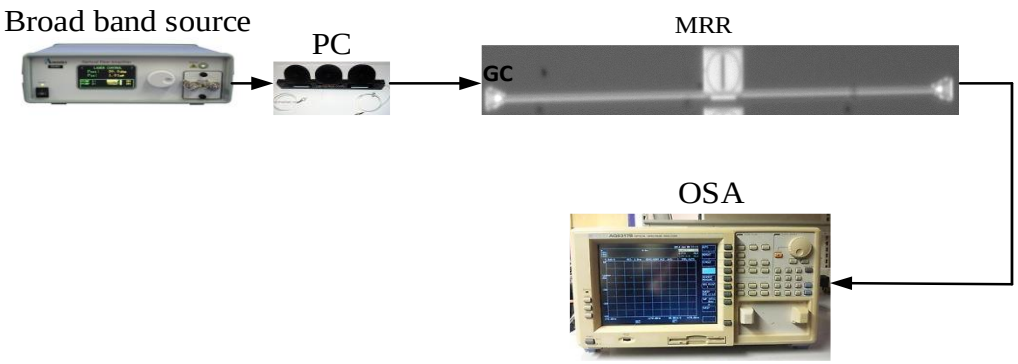

Fig. 3.21: Experimental setup to measure transmission response of the MRR, PC: polarization controller, OSA: optical spectrum analyser, GC: grating coupler.

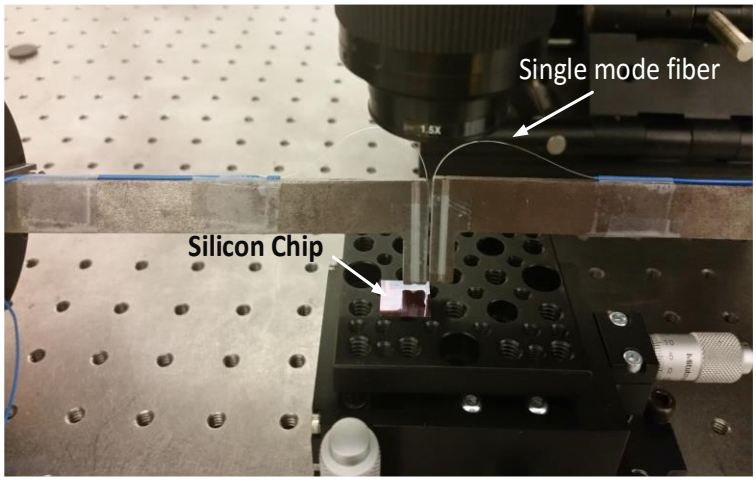

Fig.3.22: Experimental setup which shows how single mode fiber coupled into and out of the MRR

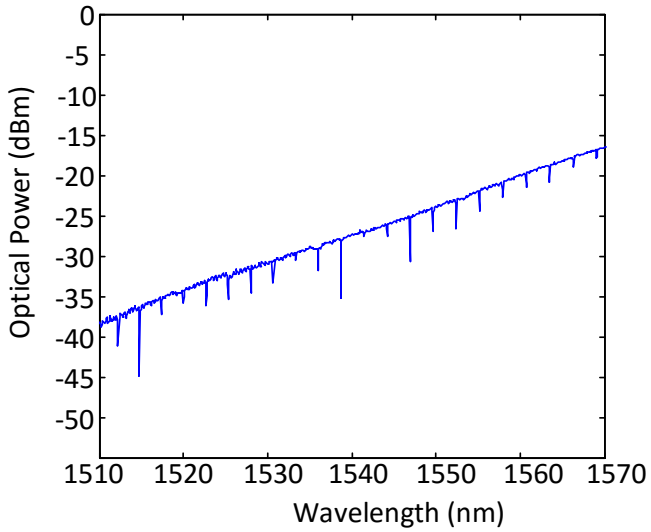

Fig.3.23: Measured transmission response of the MRR over 60 nm bandwidth

3-6. Single pass-band microwave photonic filter

In this part, we propose and demonstrate a single pass-band frequency-tunable microwave photonic filter (MPF) based on phase modulation to intensity modulation (PM-IM) conversion using the high Q-factor SOI MRR which was designed in previous part. The key advantage of an MPF implemented in the optical domain is the large frequency tunable range which is difficult to realize using electronic methods. To avoid optical interference which is extremely sensitive to environmental changes, most of the reported MPFs are implemented in the incoherent regime based on a multi-tap delay-line structure with a finite impulse response (FIR) or infinite impulse response (IIR) in which the multiple taps are usually realized using multiple wavelengths [16]. Due to the discrete time delays, a multi-tap delay-line MPF has a spectral response that is periodic. For many applications, however, it is required that an MPF has only a single pass-band [51]. To implement a single pass-band MPF with a low noise figure, an effective solution is to implement MPFs in the coherence regime [52]. In the proposed MPF, a microwave signal is modulated on an optical carrier at a phase modulator. The phase-modulated signal is then sent to the MRR. One first-order sideband is suppressed by the notch, thus the phase-modulated (PM) signal is converted to an intensity-modulated (IM) signal, and PM-IM conversion is achieved. The detection of the single side band (SSB) signal at a photodetector (PD) would generate a microwave signal. The overall operation is equivalent to a single pass-band MPF with its center frequency determined by the wavelength difference between the optical carrier and the MRR notch.

3-6.1. Principle of operation

Fig.3.24 shows the schematic of the proposed signal pass-band MPF. A light wave from a laser diode is coupled to a phase modulator, to which a RF signal is applied via its RF port to phase modulate the light wave. The modulated signal can be expressed as

$$E(t) = A_0 e^{j\omega_0 t} + A_{-1} e^{j(\omega_0 - \omega_{RF})t} + A_1 e^{j(\omega_0 + \omega_{RF})t} \qquad (3\text{-}21)$$

where A_0 is the optical field of the input light wave, A_1 and A_{-1} are the first order sidebands. The value of the phase modulation index is set small so that the power of the second-order

and higher order sidebands is much smaller than that of the carrier and the first-order sidebands. Therefore, only the optical carrier and the two first-order sidebands are considered, and ω_0 and ω_{RF} are the angular frequencies of the optical carrier and the RF signal, respectively. Then the phase modulated signal send to the MRR, where one of the first-order sidebands falls in the notch of the MRR. The optical carrier and the remained first-order sideband are then applied to a photodetector (PD). The beating between these two components will generate a microwave signal which is equivalent to a single pass-band filter response [53].

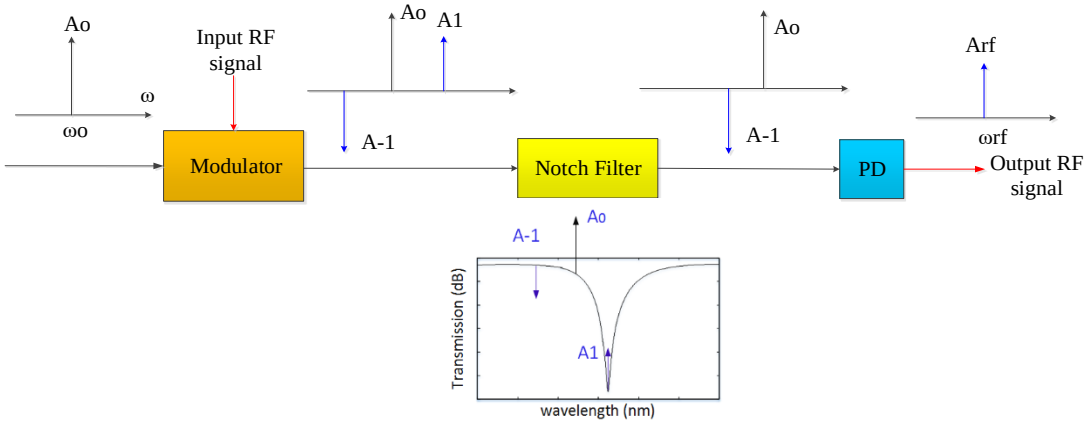

Fig.3.24: Schematic of single pass-band MPF

3-6.2. Tunability of the resonance wavelength

At high powers, the stored light in silicon MRR is absorbed via two photon absorption (TPA) and generates free carriers. The generated carriers lead to free carrier absorption (FCA). At wavelengths near 1550 nm TPA is significant and can result in large TPA induced free carrier index changes. The TPA and FCA nonlinear processes result in the heating of the resonator and this thermo optic (TO) effect causes a red-shift in the resonance [54], [55]. The free-carrier dispersion (FCD) effect due to the TPA also induced free carrier generation and will introduce a blue-shift in the resonance wavelength. The effective resonance shift $\Delta\lambda$ owing to the counteracting effects of FCD and TO processes in the silicon MRR can be expressed as

$$\Delta\lambda \approx \frac{\lambda_0}{n_g}\left(\Delta n_{FCD} + \Delta n_{TO}\right) \qquad (3\text{-}22)$$

where λ_0 is the resonant wavelength, n_g is the group index of the MRR, and Δn_{FCD} and Δn_{TO} are the refractive index changes of the silicon owing to the FCD and TO effects, respectively. Since the TO effect is much greater than the FCD effect, the overall wavelength is red-shifted. Fig.3.25 shows the fabricated SOI MRR. The MRR has a radius of 30 µm, the coupling length between the ring and waveguide is 10 µm and the coupling gap is 280 nm. The transmission response of the MRR is measured and result is shown in Fig.3.26. Two individual resonances are highlighted at the wavelengths λ_1=1535.85 nm and λ_2=1538.56 nm. The FSR is 2.7 nm. The quality factors are determined by fitting the resonances with Lorentzian line shapes which yields Q $\lambda_1 \approx 10^5$ (first resonance) and Q$\lambda_2 \approx 3\times 10^4$ (second resonance).

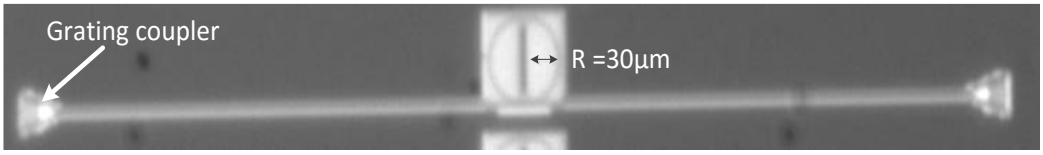

Fig. 3.25: Image of the fabricated MRR with grating coupler

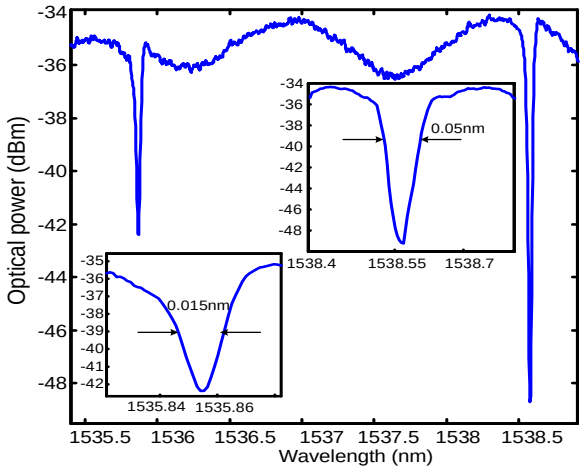

Fig. 3.26: Measured spectrum of the MRR for TE polarization. Inserts: zoom-in views of the two notches at 1535.855 nm and 1538.56 nm with 3dB bandwidth.

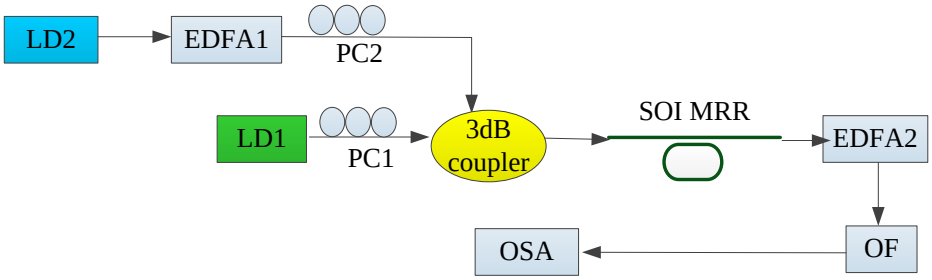

Fig. 3.27: Experimental set-up to measure resonance wavelength shifting. LD: laser diode, PC: polarization controller, EDFA: erbium-doped fiber amplifier, OF: optical filter, OSA: optical spectrum analyser.

To investigate the tunability of the resonances associated with the thermo optic effects, we employed experimental set-up as shown in Fig. 3.27. We position a CW probe (LD1) on λ_2, and then the wavelength of the pump light (LD2) is selected to be at λ_1 to maximize the coupling of the light into the MRR. Note that the Q-factor of the MRR at λ_1 is about 10^5, the mode can be highly localized in high Q MRR and the red-shift will increase. Both the pump and probe beams are coupled into the MRR via a 3dB coupler and the output spectrum is sent to the optical filter (OF) to filter out the pump signal before sending to an optical spectrum analyser (OSA). The measured transmission response of the MRR at different pumping power levels of 34, 31, 28, 25 dBm (This power level is at the output of the EDFA1) is shown in Fig.3.28. The transmission response without pumping is also shown. It can be seen the resonance wavelength is shifted to a longer wavelength with the increase of the pumping power. In fact, the resonance wavelength is red-shifted from about 1538.56 to 1538.62 nm with a total wavelength shift of $\Delta\lambda = 0.06$ nm.

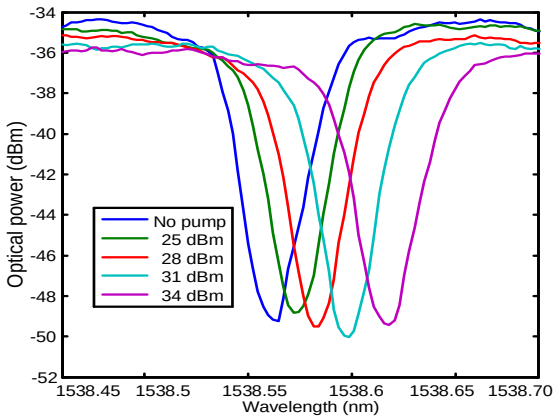

Fig.3.28: Measured transmission spectrum of the MRR showing a net red-shift of resonance with the increase of the pump power from 0 (no pump) to 34 dBm.

3-7. Experimental set up for tunable MPF implementation

An experiment based on the setup shown in Fig. 3.29 is performed. The wavelength of the optical carrier (LD_1) is chosen to be slightly less than the center wavelength of the second notch ($\lambda 2$ = 1538.56 nm). Thus, one sideband will suppress in the notch of the MRR when the microwave frequency is equal to the frequency difference between the optical carrier and the $\lambda 2$. In our system, the phase-modulated light wave is injected into the MRR that is employed to filter out one sideband, to achieve PM-IM conversion. The central frequency of the pass-band MPF is determined by the wavelength difference between the optical carrier and the notch. Therefore, the central frequency of the MPF can be tuned by changing the wavelength of the optical carrier or the wavelength of the notch resonance ($\lambda 2$).

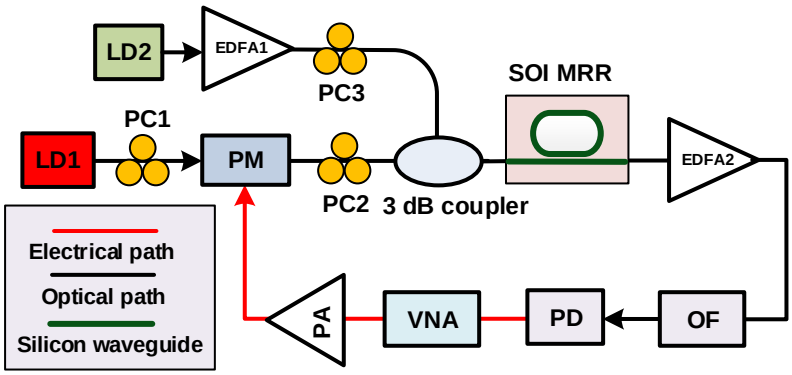

Fig. 3.29: Schematic of the proposed single passband MPF. LD: laser diode, PC: polarization controller, PM: phase modulator, EDFA: erbium-doped fiber amplifier, OF: optical filter, PD: photodetector, VNA: vector network analyzer, PA: power amplifier.

To measure the spectral response of the MPF, a microwave sinusoidal signal generated by the VNA with a frequency sweeping from 45 MHz to 40 GHz is applied to the phase modulator. This MRR is designed to only support the transverse electric (TE) mode. Thus, in the experiment, PC2 and PC3 are adjusted to ensure that the input signal to the MRR is TE polarized. The profile of a notch of the MRR is Lorentzian. The frequency response of the MPF is directly translated from the Lorentzian notch due to the PM-IM conversion, thus the frequency response should also have a Lorentzian shape. The optical carrier and the first-order sideband are then applied to a PD. The beating between these two components will generate a microwave signal which is equivalent to a single pass-band filter response. As can

be seen in Fig. 3.30, the frequency response is fitted using a Lorentzian function [56], good agreement is observed. The central frequency of the MPF is 16 GHz, corresponding to a wavelength difference of about 0.13 nm between the optical carrier and the notch. The free spectral range of the MRR is around 2.7 nm or, equivalently, 337 GHz. Thus, the maximum central frequency of the single passband MPF can be 168.5 GHz, when the optical carrier is placed in the middle of the two resonant notches. The 3-dB bandwidth is around 6 GHz, which is determined by the 3-dB bandwidth of the notch at 1538.56 nm; the slight difference between 3-dB bandwidth of the filter and notch comes from self-phase modulation (SPM) effect which is resulted from TPA [57] causes the spectral broadening in the MPF spectrum response and adds the flatness on top of the filter. The bandwidth of the MPF can be reduced by using an MRR with a narrower notch.

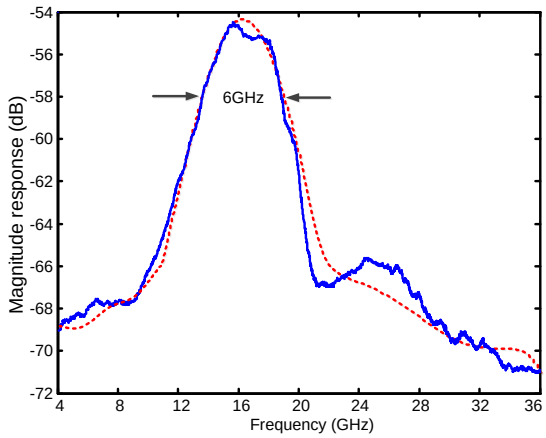

Fig.3.30: Measured frequency response of the MPF and its Lorentzian fit. The center frequency is measured to be 16 GHz and the 3-dB bandwidth is around 6 GHz.

Then, we demonstrate the frequency tunability by optical pumping the MRR. To do so, a pumping light from LD2 and amplified by EDFA2 is applied to the MRR. Since the central frequency of the MPF is equal to the wavelength difference between the optical carrier and the notch, by changing the location of the notch, the central frequency of the MPF is changed. Fig. 3.31 shows the frequency response of the MPF when the central frequency is tuned from 16 to about 23 GHz by changing the pumping power from 0 (no pump) to 34 dBm. The pumping power is measured to be 34 dBm at the output of the EDFA. Due to the low efficiency of the grating coupler, the real input pumping power is about 27 dBm. The

frequency tuning range is about 7 GHz. To increase the frequency tunable range, we may simply use a pumping source with a large tunable power, but a higher pumping power may damage the device, especially at the fiber-chip interface. Another solution is to design an MRR that is more sensitive to the TO effect [58]. The key advantage of this method is that the optical carrier remains constant, which is important for applications where the signal is carried by an optical carrier with a fixed wavelength and cannot be tunable. In addition, the use of a fixed optical carrier wavelength increases the frequency stability of the MPF. Furthermore, the frequency tuning resolution can be significantly increased since the pumping power can be precisely controlled with a high tuning resolution, while the wavelength tuning step of a TLS is usually large.

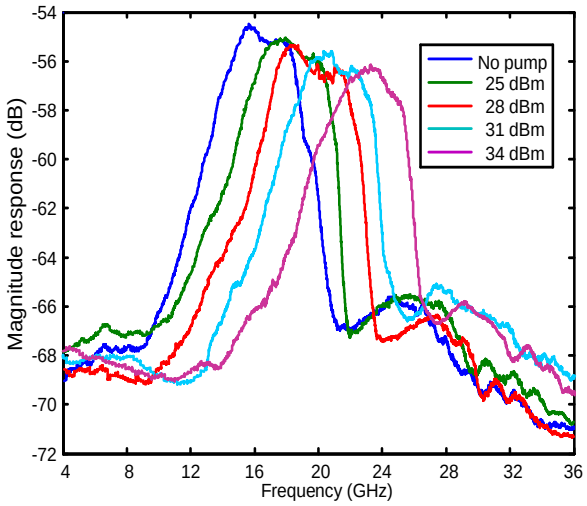

Fig.3.31. Measured frequency response of the MPF with the central frequency tuned from about 16 to 23 GHz by pumping the MRR with a pumping power from 0 (no pump) to 34dBm.

In conclusion a single pass-band and frequency-tunable MPF based on PM-IM conversion in an SOI MRR was proposed and experimentally demonstrated. The fundamental concept of the approach was to filter out one sideband of a phase-modulated signal, to convert the phase-modulated signal to an intensity-modulated SSB signal. The optical carrier and the first-order sideband were then applied to a photodetector (PD). The beating between these two components generates a microwave signal which was equivalent to a single pass-band filter response with the central frequency tunable by tuning the resonance wavelength of the MRR.

CHAPTER 4 Optically Tunable Full 360º MWP Phase Shifter Using Three Cascaded SOI MRRs

4-1. Cascaded MRRs

Fig 4.1 shows the cascaded MRRs configuration, we assume that all the rings are perfectly isolated optically from one another. Each ring has the same circumference. Total transmission response for identical cascaded MRRs is as follow [59]

$$\frac{E_{t(n+1)}}{E_{in}} = \left[\frac{t - a\exp(j\varphi)}{1 - ta\exp(j\varphi)}\right]^n \tag{4-1}$$

n is the number of the cascaded MRRs. The total phase shift of the transmitted light for one ring is given by

$$\phi = \pi + \varphi + \arctan\left(\frac{t\sin\varphi}{a - t\cos\varphi}\right) + \arctan\left(\frac{at\sin\varphi}{1 - at\cos\varphi}\right) \tag{4-2}$$

By increasing the number of the MRRs in a cascaded configuration, the total phase shift can be increased. For *n* identical cascaded MRRs, the total phase shift across one FSR is $n\phi$ [59]. Fig. 4.2 shows numerical results of the transmission and phase response for an MRR at the through port with different coupling condition in MRR. In under-coupling and critical-coupling conditions (Figs. 4.2(a) and (b)) the phase shift cannot reach the maximum value. Whereas, at the over-coupling conditions, as shown in Fig. 4.2(c) the phases experience a 2π shift.

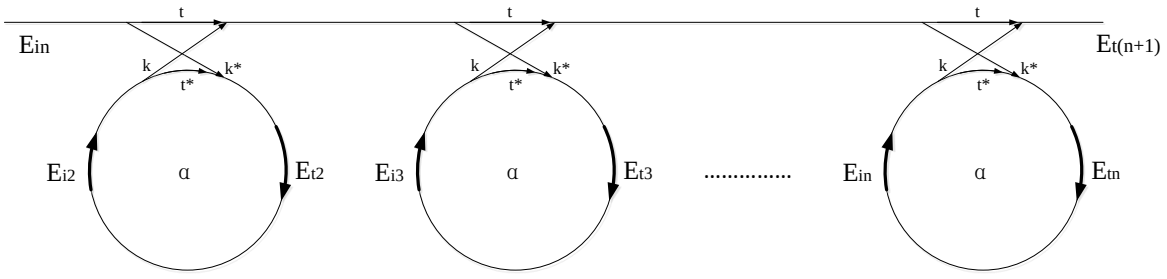

Fig. 4.1. Schematic of cascaded MRRs

As can be seen in Fig. .4.2 (d) as the notch depth decreases the maximum phase shift decreases. Here, we assume the radius of the SOI MRR is 20μm and the effective group index of the SOI waveguide is 4.26.

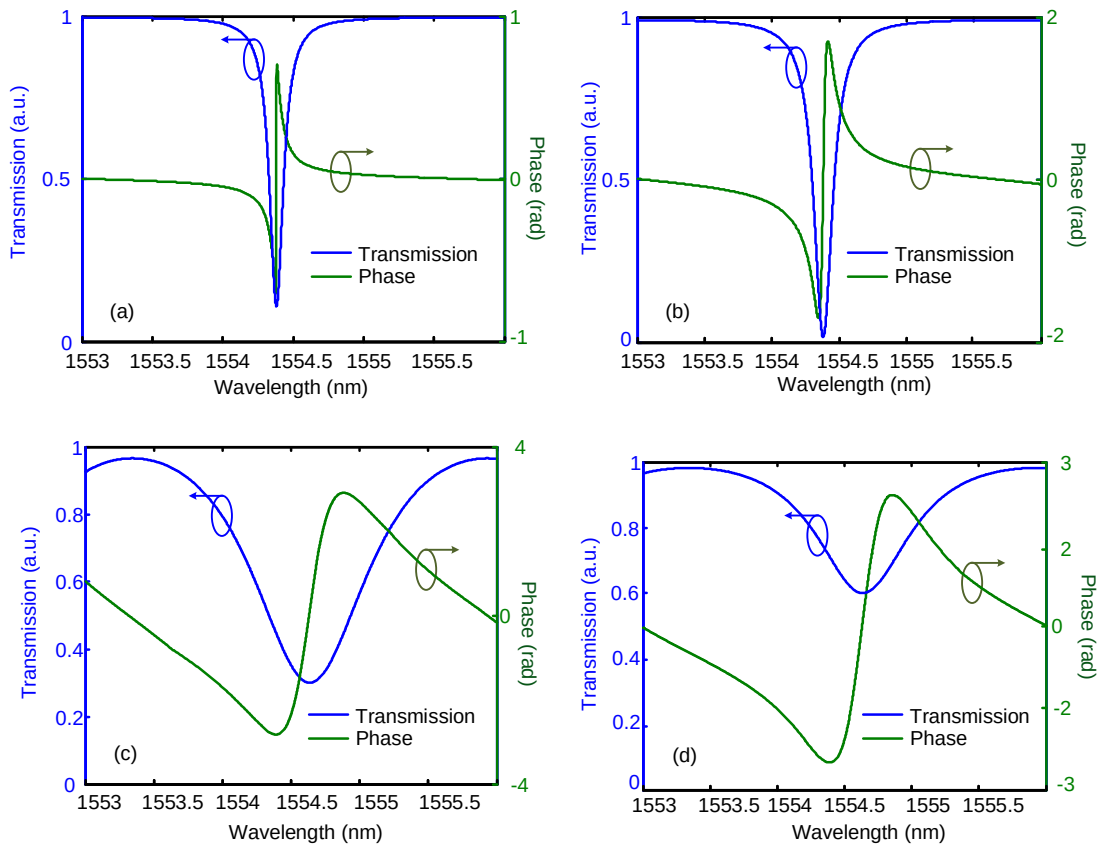

Fig. 4.2: Transmission and phase response at the through port for the MRR under different coupling conditions: (a) under-coupling with k = 0.06, (b) critical-coupling with $k^2 = 1\text{-}a^2 = 0.01$, (c) over coupling with k = 0.3, and (d) over-coupling with k = 0.4 (a~0.997). (R=30μm).

By increasing the number of cascaded MRRs the phase shift increases. For example Fig. 4.3 shows the simulation result in the over-coupling condition for three cascaded MRRs. As expected the phase shift around 6π can be achieved. If, in this case, a single side band modulated signal with two peaks of the desired frequency spacing is input to the MRR, the phase difference of the two peaks can be tuned by changing the central wavelength of the phase response, and thus realizing a microwave phase shift. Therefore, a tunable MRR working in the over-coupling regime is preferred in order to make a microwave phase shifter with large and continuous tuning range.

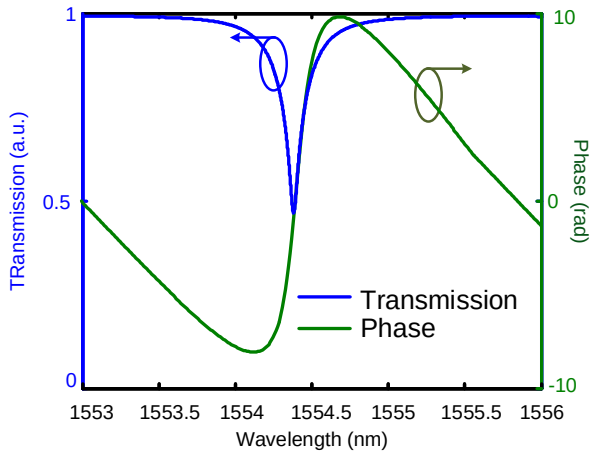

Fig. 4.3: Transmission and phase response at the through port for the three cascaded MRRs under the over-coupling condition with k = 0.4 (a~0.997)

4-2. MWP phase shifter

Microwave phase shifters are one of the key components of microwave systems in applications such as phased array antennas, arrayed signal processors and microwave filters [1]. However, it is difficult to realize phase shifters that can operate over a very wide microwave frequency range using pure electronics phase shifters [60]. The use of photonic solutions to implement microwave phase shifters has the advantages of greater bandwidth due to the ultra-wideband nature of photonics, and large tunability. In this part, we propose and experimentally demonstrate a full 360° optically tunable phase shifter based on three cascaded passive MRRs over a broad bandwidth of 7 GHz. The result for single MRR is also discussed. In order to introduce a phase shift in microwave signal, it is applied to an optical single-sideband (OSSB) modulator to generate an optical carrier and a sideband. The phase shift is introduced to the modulated signal by placing the optical carrier within the bandwidth of one of the MRRs resonances. The phase tuning is implemented based on the thermal nonlinear effect in the MRRs as discussed in chapter 3.

4-3. Principle of operation

Fig.4.4. shows the schematic of a microwave photonic phase shifter using an SOI MRR. A microwave signal to be phase shifted is modulated on an optical carrier at an OSSB modulator. The OSSB-modulated signal with an optical carrier and a sideband is then sent to the SOI-MRR. Mathematically, under small-signal modulation condition the optical field at the output of the OSSB modulator (point B) can be expressed as

$$E(t)_{in} = A_0 \exp(j\omega_0 t) + A_1 \exp\left[j(\omega_0 + \omega_{rf})t\right] \tag{4-3}$$

where A_0 and ω_0 are the amplitude and the frequency of the optical carrier, and A_1 and $\omega_0+\omega_{rf}$ are the amplitude and frequency of the first-order sideband, respectively. The optical field at the output of the SOI MRR (point C) is given by [28]

$$E_{out}(t) = A_0 B \exp(j\omega_0 t)\exp(j\theta_0) + A_1 B' \exp\left[j(\omega_0 + \omega_{rf})t\right] \tag{4-4}$$

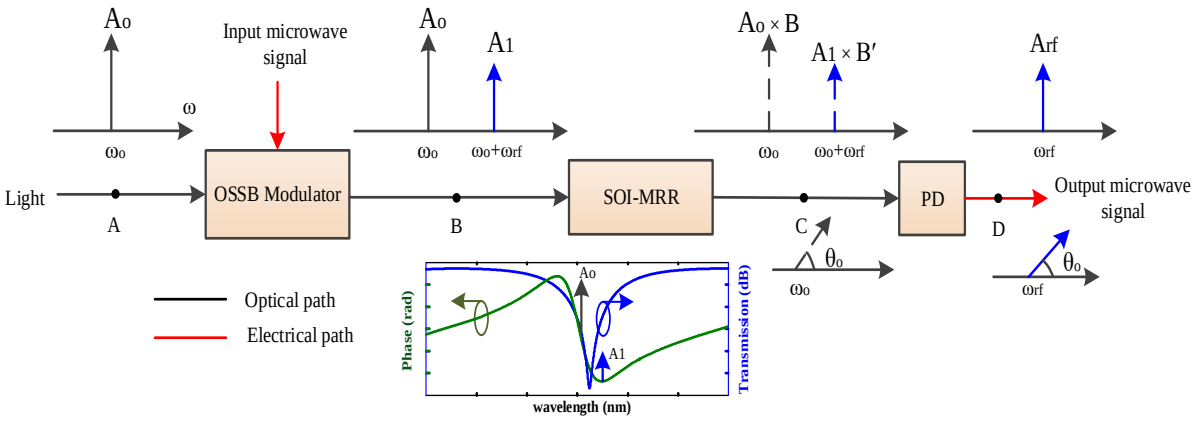

Fig.4.4. Schematic of the proposed microwave photonic phase shifter. OSSB: optical single-sideband, SOI-MRR: silicon-on-insulator microring resonator, PD: photodetector. (The amplitude and phase of the SOI-MRR have been shown)

where B and B' are the amplitudes of the MRR spectral response at ω_0 and $\omega_0+\omega_{rf}$, respectively and θ_0 is the phase shift at ω_0 of the MRR spectral response. The phase shifted optical carrier and the first-order sideband are then applied to the PD. The beating between

these two components will generate a microwave signal (point D) with a phase shift equal to the phase difference between the optical carrier and the first-order sideband. The phase-shifted microwave signal is given by

$$i_{RF}(t) = R\left|E_{out}(t)\right|^2 = RA_0A_1BB'\cos(\omega_{rf}t + \theta_0) \qquad (4\text{-}5)$$

where R is the responsivity of the PD. As can be seen from Eq. (4-5), the phase shift introduced to the optical carrier by the SOI MRR is directly translated to the microwave signal. The value of the phase shift is optically tunable by optically pumping the SOI MRR which would cause a continuous lateral shift of the spectral response and consequently a phase shift.

4-4. Experimental results

The key component in the proposed MWP phase shifter is the SOI MRRs fabricated on an SOI platform. Each MRR has a radius of 20 μm with a 220-nm-thick silicon slab on top of a 2-μm silica buffer layer. The coupling length between a MRR and the waveguide is 10 μm. Two grating couplers are incorporated to couple the light into the MRRs from a single-mode fiber and out of the MRRs to another single-mode fiber. Fig 4.5 shows the images of the fabricated single MMR and three cascaded MRRs. An experiment is performed, which is done based on the experimental setup shown in Fig. 4.6. A light wave from a laser diode (LD1) is coupled via a polarization controller (PC1) to a Mach-Zehnder modulator (MZM), to which a microwave signal from a vector network analyzer (VNA) is applied via the RF port. An optical double-sideband (ODSB) signal is obtained at the output of the MZM. To suppress one of the two sidebands, a wave-shaper serving as an optical notch filter to suppress one sideband is connected to the output of the MZM and an OSSB-modulated signal is thus obtained.

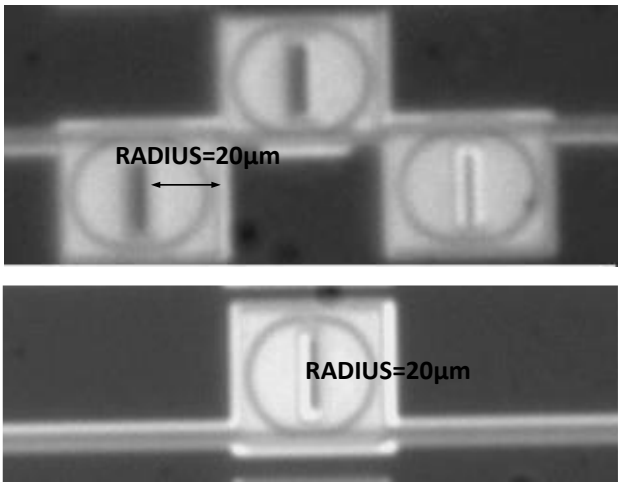

Fig. 4.5: An image of the fabricated single MRR, and 3 cascaded MRRs.

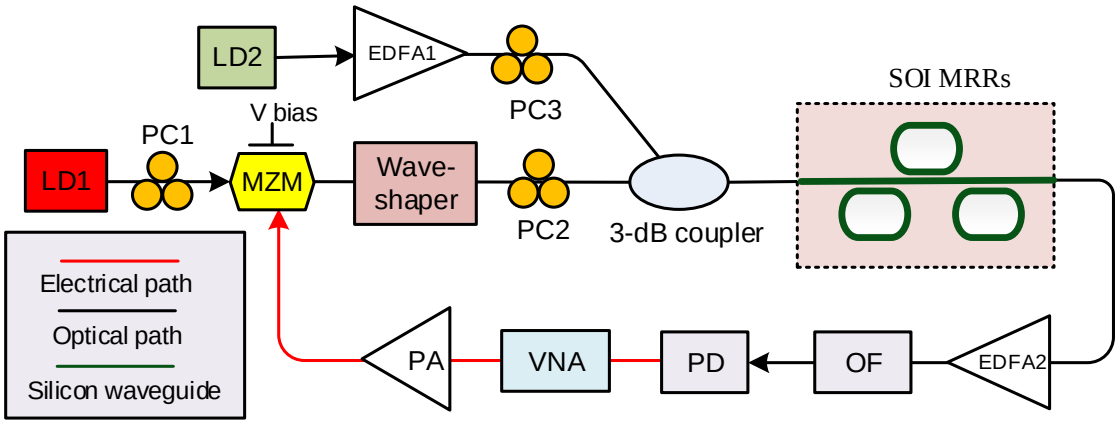

Fig. 4.6: Experimental set up. LD: laser diode, PC: polarization controller, MZM: Mach-Zehnder modulator, EDFA: erbium-doped fiber amplifier, OF: optical filter, PD: photodetector, VNA: vector network analyzer, PA: power amplifier.

The OSSB-modulated optical signal is then sent to the SOI-MRRs via a second PC (PC2). A pumping light wave from a second LD (LD2) is amplified by an erbium-doped fiber amplifier (EDFA1) and sent to the SOI MRRs via a 3-dB coupler. The MRRs are designed to only support the transverse electric (TE) mode. Thus, during the experiment, PC2 and PC3 are adjusted to ensure that the input signal to the MRRs is TE polarized. The output optical signal of the MRRs is amplified by a second EDFA (EDFA2) and sent to an optical filter (OF) to filter out the residual pumping light before applying to a PD. Fig. 4.7 shows the measured magnitude and phase response of an MRR at different pumping power levels of 27, 22, 18dBm. The response without pumping is also shown. By increasing the pump power, the magnitude and phase response is shifted to a longer wavelength. By placing the optical

carrier and sideband of an OSSB signal in the bandwidth of the phase response a phase shift will be introduced to the modulated signal. As shown in Fig. 4.7(b), the maximum value of RF phase shift is 228°. A full 360° RF phase shift is difficult to realize through a single MRR [26]. The single MRR has an extinction ratio of 12 dB and 0.06-nm 3-dB bandwidth slightly above the critical coupling condition. Since the RF power follows the optical power, the large RF power variation due to the high extinction ratio of the MRR hampers the application as an RF phase shifter. This problem can be resolved by using a low-Q MRR with a higher coupling coefficient (narrower coupling gap), which will give a lower extinction ratio.

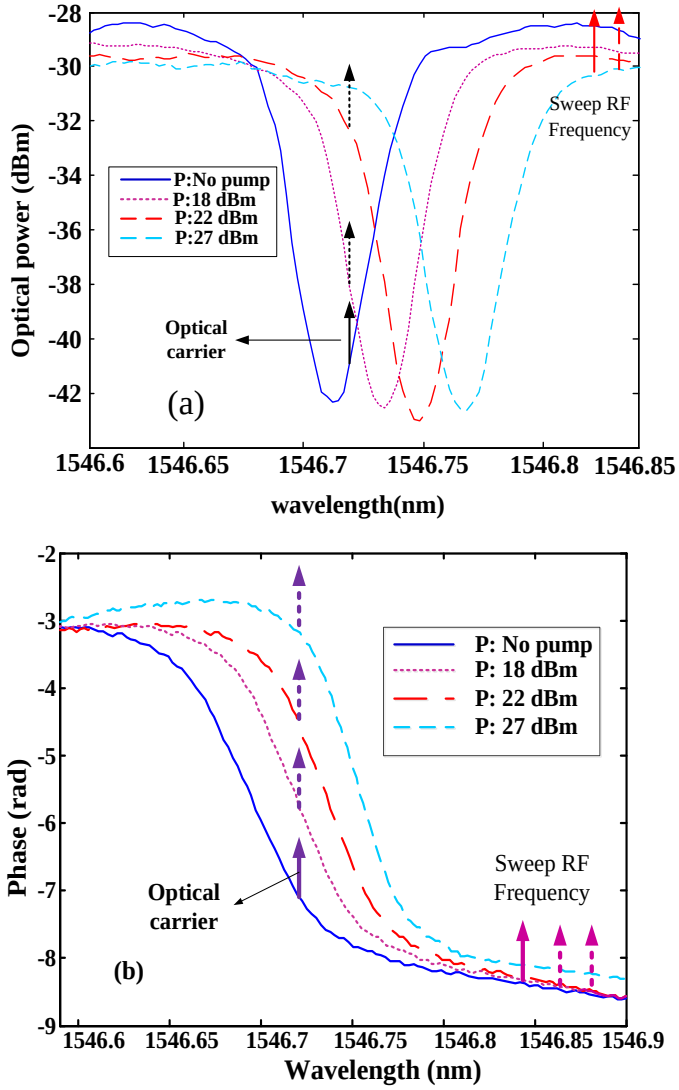

Fig. 4.7: (a) The magnitude response, and (b) the phase response of the single MRR showing a net red-shift of the magnitude and phase with the increase of the pump power from 0 (no pump) to 27dBm.

The MRR with higher Q-factor provides a larger RF phase shift. However, the lower-Q MRR gives a smaller RF power variation at the expense of reduced maximum RF phase shift. Since the RF power variation is a vital factor in many microwave applications, the low-Q MRR with small RF power variation and good phase-shift linearity would be a more practical option for the real applications. In this case, more than one MRR is necessary to achieve a full 360^{O} RF phase shift. Here three cascaded MRRs have been designed to achieve a linear 360° RF phase shift and the lowest RF power variations over a wide bandwidth. Fig.4.8 shows the transmission spectrum of the three cascaded MRRs for the TE mode where the spectral range from 1543 to 1549 nm covers two resonance notches at 1544.2 nm and 1548.03 nm. The notch depths for resonance notches are 5 dB and 16 dB, which are not equal due to the wavelength-dependent coupling conditions. Also, a zoom in view shows the first notch and its phase response. The optical carrier is placed in the bandwidth of the first notch because at this wavelength, the MRR works in the over-coupling condition and the extinction ratio is about 5 dB which cause small RF power variation. To demonstrate tunability of the phase shifter, the wavelength of the pumping light is selected to be at the wavelength of the second resonance notch, 1548.03 nm, to maximize the coupling of the light into the MRRs.

Fig. 4.9 shows the phase response of the MRRs corresponding to the first notch. The phase response is shifted from about 1544.20 to 1544.26 nm with a total wavelength shift of $\Delta\lambda$ = 0.06 nm by changing the pumping power from 0 (no pump) to 27dBm. A maximum phase shift of 855° is achieved. To realize a linear full 360° phase shift the optical carrier is set at λ = 1544.26 nm. By increasing pump power, the phase difference between the carrier and the sideband is also increasing. When the pump power is 27dBm, the phase difference between optical carrier and sideband reaches its maximum value.

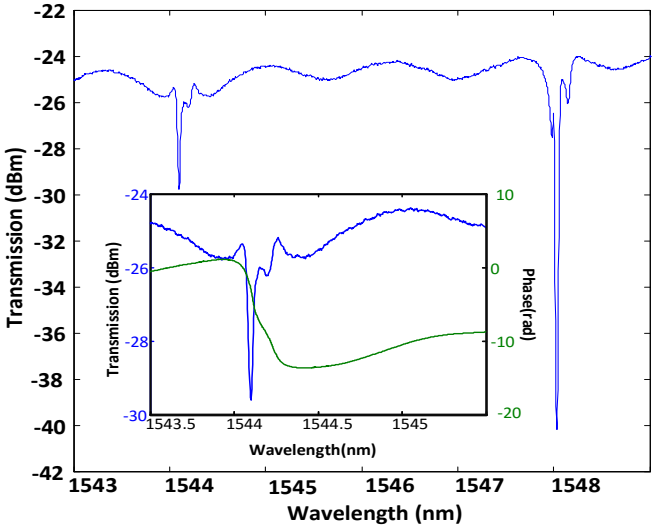

Fig. 4.8:.Transmission spectrum of the three cascaded MRRs for the TE mode.

This tunable phase shift can be used to introduce a tunable phase shift to the OSSB-modulated signal to obtain a phase-shifted microwave signal. Fig. 4.10 shows the phase shift measured using a VNA at different RF frequencies. As can be seen, a full 360° phase shift with a bandwidth of 7 GHz from 16 to 23 GHz is achieved. As expected, the phase shift is independent of the microwave frequency. This confirms that the system is a microwave phase shifter, rather than a true time delay line.

In the experiment, the phase shifter has a bandwidth of 7 GHz from 16 to 23 GHz. The higher frequency of 23 GHz is limited by the bandwidth of the PD (here the bandwidth of the PD was 25 GHz). For the proposed phase shifter, if a PD with a much wider bandwidth is used, the highest frequency will only be limited by the wavelength spacing between two resonance peaks which is about 4 nm or 500 GHz. The lower frequency of 16 GHz is limited by the notch width of the MRR. If an MRR with a narrower notch is used, the lower frequency can be smaller. Note that for a microwave phase shifter, we expect the power of the phase-shifted microwave signal at the output of the phase shifter is constant for different phase shift. In the proposed approach, the power variation is maintained small by slightly offsetting the resonance wavelengths of the three MRRs. As can be seen in the inset in Fig. 8, the notch depth is 5 dB, which is smaller than that of a single MRR. When optical carrier set in λ = 1544.26 nm , the amplitude difference between location of the optical carrier and sideband is less than 1 dB which leads to low range of RF power fluctuation after PD.

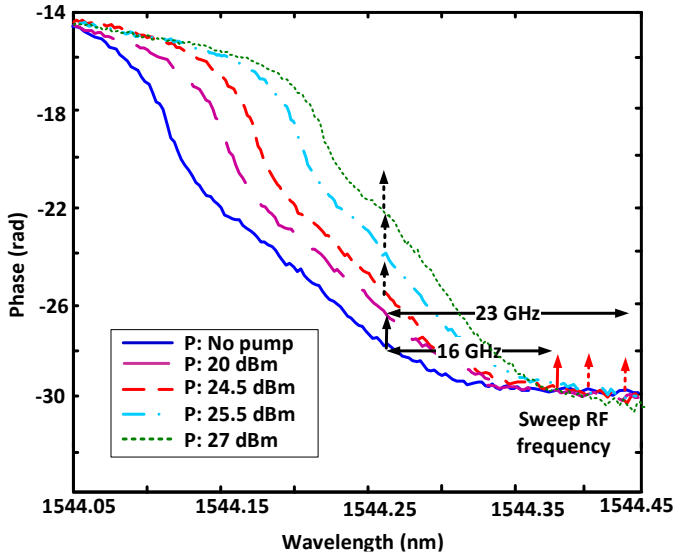

Fig.4.9: The phase response of the three cascaded MRRs showing a net red-shift of the phase response with the increase of the pumping power from 0 (no pump) to 27dBm.

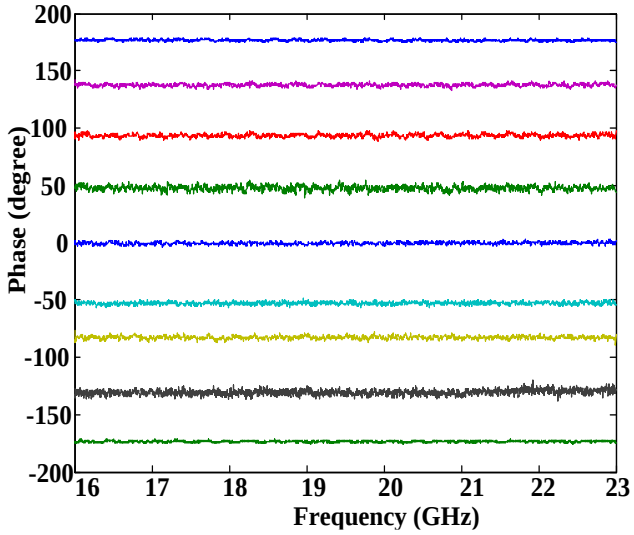

Fig. 4.10: Measured phase shifts at different pumping power levels. The phase shifts are independent of the microwave frequency.

In conclusion, a tunable microwave photonic phase shifter based on three cascaded SOI MRRs was proposed and experimentally demonstrated. The phase tuning was implemented by tuning the phase response through optical pumping. Due to the TPA-induced TO effect, the phase response was shifted to a longer wavelength, which led to the change of the phase shift of the microwave phase shifter. The use of the fabricated MRRs to implement a broadband microwave photonic phase shifter with a bandwidth of 7 GHz from 16 to 23 GHz with a tunable phase shift covering the entire 360^{o} phase shift range was demonstrated.

CHAPTER 5 MULTI TAP MWP FILTER USING SILICON-ON-INSULATOR RING MODULATOR

5-1. Silicon-on-insulator modulator

A critical component in an integrated MWP filter is the electro-optic modulator, the device which is responsible for the conversion of electrical signals into optical signals. Optical modulators were mainly limited to III-V semiconductor [62] and Lithium niobate (LiNbO3) [63] material platform. Applying an electric field to these materials may change the real and imaginary part of the refractive indices. A change in the real part of the refractive index (Δn) with an applied electric field is known as electro-refraction, whereas a change in the imaginary part of the refractive index ($\Delta \alpha$) is known as electro-absorption. Pockels effect, the Kerr effect and the Franz–Keldysh are three useful electric field effects in semiconductor materials for electro-absorption or electro-refraction based modulators [64]. However, these effects are extremely inefficient in silicon: silicon is transparent at the 1.55 μm optical communication wavelength and the second order susceptibility ($\chi^{(2)}$) required for electro-optic effects in silicon is zero [65]. Alternative methods are required to achieve modulation in silicon. The most conventional way to produce optical modulation in silicon is through the use of the plasma dispersion effect which conects changes in the electron and hole densities to changes in the refractive index and absorption [66]. Silicon optical modulator would typically consists of an interferometor (Mach-Zehnder interferometer (MZI) [67]) or a resonantor (microring [68], a racetrack [69],[70] or a microdisk [71]). Such structures typically use a PN diode structure around the optical waveguide to change the density of free carriers in interaction with propagating light. To be compatible with high-speed CMOS electronics, it is desired that the next generation of optical modulators operate at speeds exceeding 50 Gb/s, consume less than 10 fJ of energy per bit, operate with drive voltages under 2 V, and maintain footprint sizes under 10^3 μm^2 [72].

5-2. Plasma dispersion effect

The plasma dispersion effect is used for silicon modulators where the concentration of carriers is varied either by injecting or removing carriers from the device. The concentration of free charges in silicon changes the real and imaginary parts of the refractive index. Soref and Bennett [66] evaluated changes in the refractive index Δn from experimentally produced absorption curves for a wide range of electron and hole densities, over a wide range of wavelengths. They also quantified changes in both the refractive index and absorption, and produced the following expressions to evaluate changes in the carrier densities in silicon at a wavelength of 1.55 μm:

$$\Delta n = \Delta n_e + \Delta n_h = -[8.8\times10^{-22}\times\Delta N + 8.5\times10^{-18}\times(\Delta P)^{0.8}]$$
$$\Delta \alpha = \Delta \alpha_e + \Delta \alpha_h = 8.5\times10^{-18}\times\Delta N + 6\times10^{-18}\times\Delta P \quad (5\text{-}1)$$

where ΔN, ΔP are the carrier densities of electrons and holes [cm^{-3}] and $\Delta\alpha_e$ and $\Delta\alpha_h$ are the changes in absorption resulting from changes in the free-electron and free-hole carrier concentrations, respectively. In comparison to electrons, holes have a smaller absorption and larger index shift. Thus, holes are most effective for providing an index shift with minimal absorption; hence modulators typically use holes for offset junction designs. Carrier injection through a P-N junction is a slow process, and can only reach modulation bandwidths of a few GHz at most [73]. Hence, carrier depletion in P-N diodes is the common method for light modulation in silicon waveguides.

5-3. PN junction phase shifter

The impurity and carrier distributions in a carrier-depletion phase modulator are illustrated in Fig. 5.1. The rib waveguide is embedded with a lateral PN junction whose doping concentration is shown in Table. 5.1. These parameters correspond to typical values found in foundry processes of SOI modulation diodes. The two ohmic contact regions of the PN junction (p++ and n++) are heavily doped. There are two levels of contact vias and aluminum (Al) interconnects for electrical contact. The etching depth is 90 nm and the dimension of the rib waveguide accommodating the PN junction is 500 nm × 220 nm.

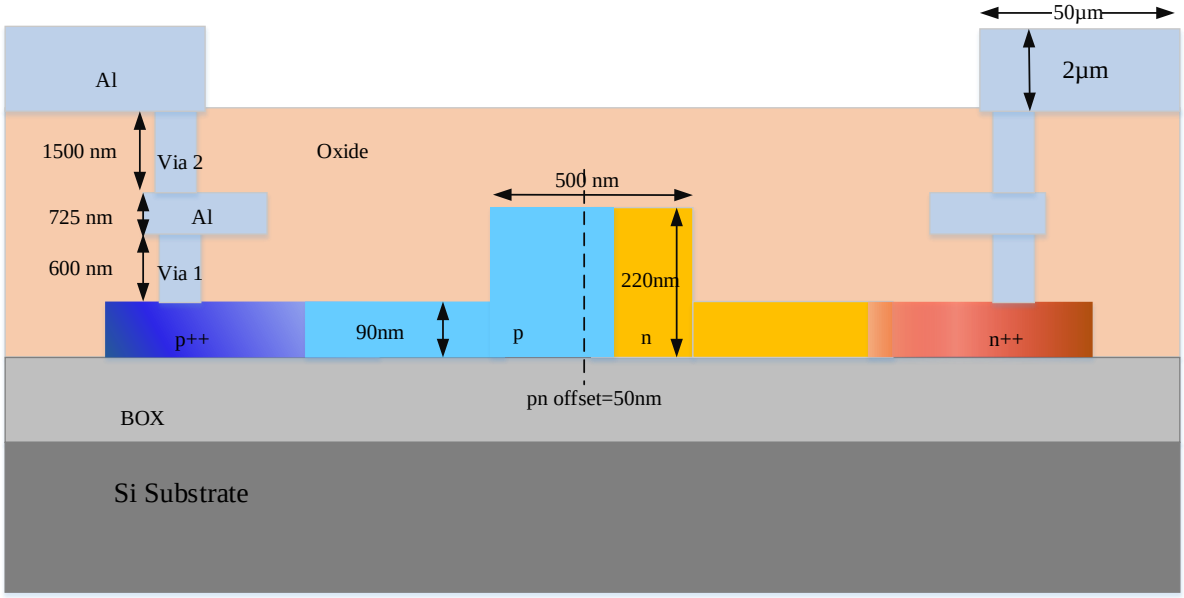

Fig. 5.1: Cross-sectional view of the PN-Junction in a rib waveguide with the carrier distribution

Table.5.1: PN junction parameters used in calculations.

Parameters	Value
Carrier concentration in p region	7×10^{17} cm^{-3}
Carrier concentration in n region	5×10^{17} cm^{-3}
Carrier concentration in p++ region	1.7×10^{20} cm^{-3}
Carrier concentration in n++ region	5×10^{20} cm^{-3}

The effective index (n_{eff}) and absorption (α_{pn}) as functions of applied voltage are given by:

$$n_{eff,i}(V) = n_{eff,i} + \frac{\int E^*(y).\Delta n(y,V)E(y)dy}{\int E^*(y).E(y)dy}.\frac{dn_{eff}}{dn_{co}}$$

$$\alpha_{pn}(V) = \frac{\int E^*(y).\Delta\alpha(y,V)E(y)dy}{\int E^*(y).E(y)dy} \qquad (5\text{-}2)$$

where $n_{\text{eff},i}$ is the effective index of the waveguide without any doping and dn_{eff}/dn_{co} (change of effective index mode versus change in effective index of the core) is typically very close to 1. *E(y)* is the field profile found using the effective index method. Then the voltage-dependent changes in effective index and phase are given by:

$$\Delta n_{eff}(V) = n_{eff}(V) - n_{eff}(0)$$

$$\Delta\phi = \frac{\Delta n_{eff}(V).2\pi}{\lambda}.L \qquad (5\text{-}3)$$

where *L* is the length of the phase shifter. Fig. 5.2 shows the electric field intensity of the guided mode calculated using Mode solution.

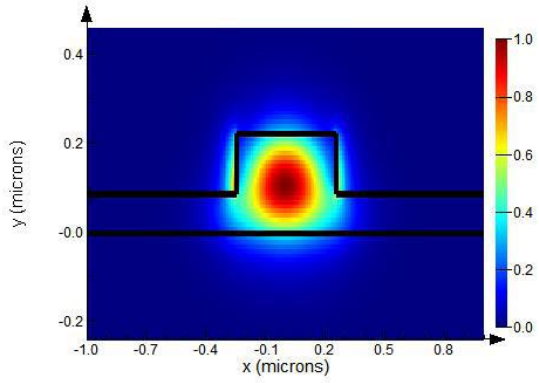

Fig. 5.2: Electric field intensity of the fundamental mode calculated using mode software (simulation result).

Holes have stronger effect on the effective index than electrons; therefore an offset can be used to optimize the modulation efficiency. A 50 nm doping offset is used in the calculation. Changes in effective index as a function of reverse applied voltage is calculated and shown in Fig. 5.3. By increasing the reverse voltage bias the effective index increases, because the carriers are removed from the waveguide by the applied voltage. The change in the phase is plotted in Fig. 5.4. A voltage of 1.8 V is needed to make a phase shift of π for a waveguide of 1 cm long.

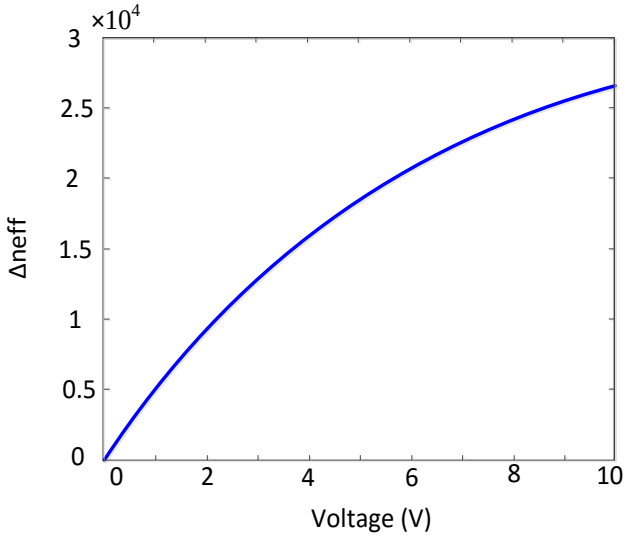

Fig. 5.3: Changes in effective index as a function of applied voltage (reverse biased) (numerical result).

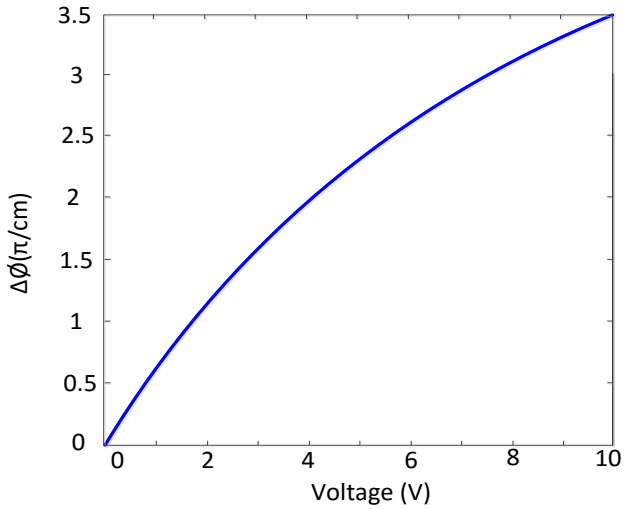

Fig.5.4: Phase change as a function of applied voltage (reverse biased). (numerical result).

The small-signal model equivalent the pn junction is illustrated in Fig. 5.5. The 3 dB cutoff frequency determined by the RC time constant can be found by

$$f_c = \frac{1}{2\pi R_j C_j} \tag{5-4}$$

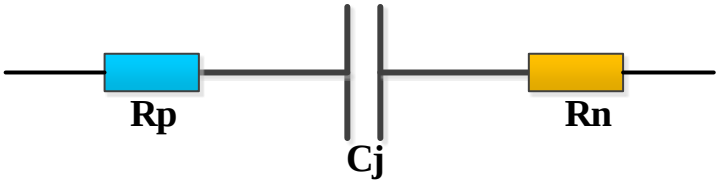

Fig.5.5: Small signal model for pn junction

Cj represent the capacitance of the reverse biased PN junction, Rn and Rp are the series resistances over the length of the diode due to the slab and rib sections and R_j is the equivalent resistance. As shown in Fig. 5.6, f_c increases by increasing the applied reverse bias due to simultaneous reduction of *Rj* and *Cj*, and as a result of the expanded depletion region. We can see that the frequency response of the PN-junction can easily go beyond tens of GHz; the resistance of the junction is an important parameter that can be reduced by optimizing the doping concentrations and the distances between dopants and junction. Minimizing the distance between the contact and junction will lead to a reduced *RC* time constant and increase the f_c.

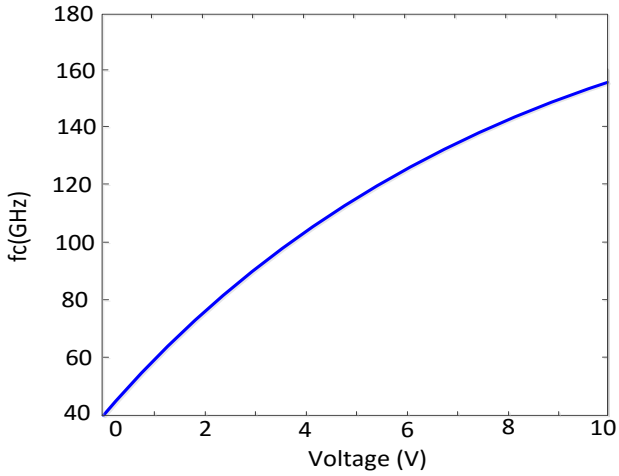

Fig.5.6: Cutoff frequency as a function of applied voltage (reverse biased). (numerical result).

The modulation speed of a silicon modulator based on the plasma dispersion effect can be determined by how fast the free carriers is injected or removed. Three different device configurations, namely, forward biased p-i-n diode [74], MOS capacitor [75], and reverse biased PN junction [76] have been proposed to achieve phase modulation in silicon. Despite of the high modulation efficiency in forward biased p-i-n diode the modulation speed is

usually limited due to the slow carrier generation and/or recombination processes, unless the carrier lifetime is significantly reduced. While both MOS capacitor and reverse biased PN junction rely on electric-field induced majority carrier that can potentially achieve >10 Gb/s operation.

So far, we have discussed how optical modulators in silicon can change the refractive index of the material, or how to induce absorption. Here there are two options available for converting a change in refractive index into intensity modulation. First, the refractive index change can be used to shift the relative phase of two propagating waves such that they interfere either constructively or destructively. Typically, a MZI is used to achieve this. Second, including a resonant structure such as ring resonator allows the refractive-index change induced in the modulator to change the resonant condition, thus allowing the device to be switched between on- and off resonance. Compared with MZIs, ring resonators offer plenty of advantages such as compact footprint, low driving voltage and ultra-low power consumption. In the next part a ring resonator modulator based on reverse biased PN junction is designed.

5-4. Reverse bias ring resonator modulator (RRM)

A MRR has strong wavelength selectivity; therefore, when operating at a wavelength close to the resonance, the transmission is very sensitive to the phase change in the cavity. By integrating a PN-junction into the resonator cavity and modulating the phase through the plasma effect (described in the previous section) an efficient RRM can be achieved. Two ring resonator configurations all-pass and add-drop filters are commonly used to obtain a micro-ring modulator, as shown in Fig. 5.7. A quarter of the optical cavity (in the directional coupler region) is integrated with a resistor heater for thermal tuning and wavelength stability (5.7(a)). As a result of this compromise, the modulation efficiency is lower as compared to the fully modulated cavity (5.7(b)).

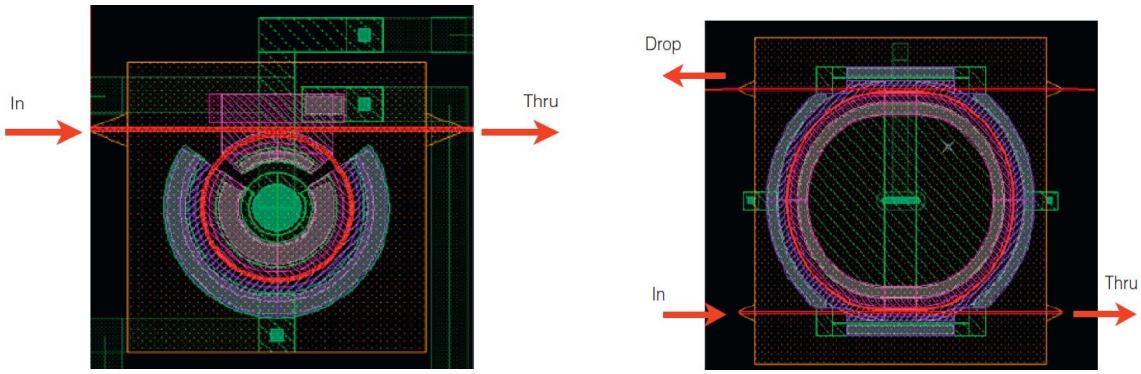

(a) (b)

Fig. 5.7: Mask layouts of micro-ring modulators. (a) All-pass (integrated with a heater for wavelength tuning), (b) Add-drop (fully modulated) [77]

First we incorporate the PN-junction model as shown in Fig.5.8 with the micro-ring resonator and then we can simulate its spectrum as a function of applied voltage. We consider a fully modulated structure (no thermal tuning is used).

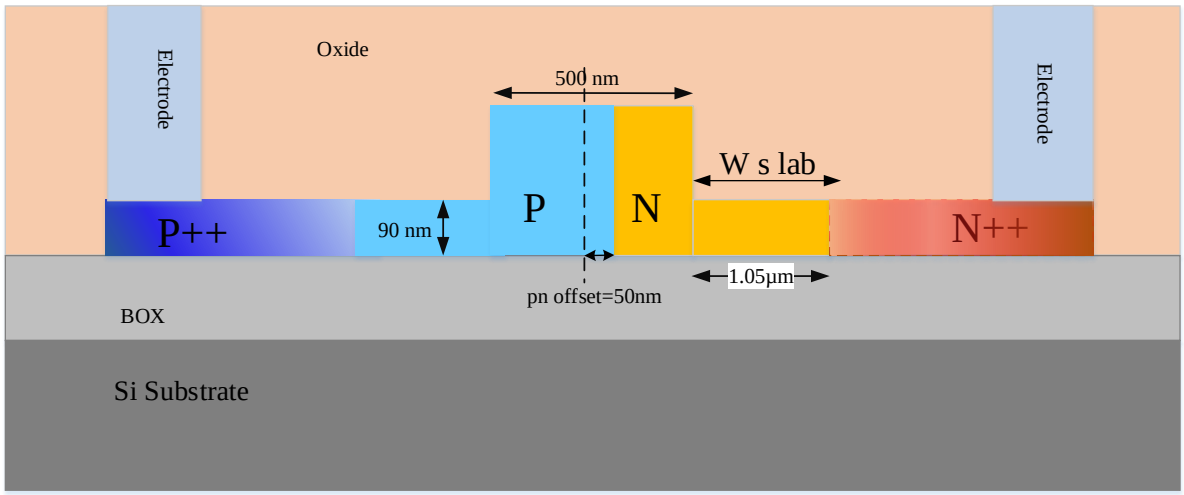

Fig 5.8: Reversed biased RRM cross-section.

The cutoff frequency (3 dB), *fc*, of the small-signal response of a RRM is determined by both the *RC* constant of the reverse-biased PN-junction and the photon lifetime, τ_p, in the optical cavity as follow [77]:

$$\frac{1}{f_c^2} = \frac{1}{f_{\tau_p}^2} + \frac{1}{f_{RC}^2} \tag{5-5}$$

The total bandwidth in ring modulator is mostly limited by photon lifetime, and RC time constant can be ignored. Then τ_p determined cutoff frequency is given by:

$$f_{\tau_p} = \frac{1}{2\pi\tau_p} \tag{5-6}$$

where τ_p is related to the total quality factor, Q_t, of the optical cavity and is given by:

$$\tau_p = \frac{Q_t}{\omega_0} \tag{5-7}$$

where ωo is the optical frequency and Q_t is determined by both the coupling and propagation losses:

$$\frac{1}{Q_t} = \frac{1}{Q_c} + \frac{1}{Q_i} \tag{5-8}$$

where the Q_i (interinsic qaulity factor) is given by:

$$Q_i = \frac{2\pi n_g}{\lambda\alpha} \tag{5-9}$$

where α is the attenuation coefficient in ring cavity and n_g is group index of the silicon waveguide. For the all-pass filter, the coupling-determined quality factor, Q_c, is given by:

$$Q_c = -\frac{\pi L_{rt} n_g}{\lambda \log_e |t|} \tag{5-10}$$

where L_{rt} is the ring circumference and t is the transmission coefficient as discussed in Chapter 3. If the add-drop configuration is used, the coupling-determined quality factor should be divided by 2 since two couplers are used in this case. Fig.5.9 shows that how the cut-off frequency changes versus total Q-factor (Q_t). The main factors in determining Q_t are losses and coupling coefficient. Loss can be manipulated by Wslab, pn-offset, waveguide width and bending radius. (The bending radius and waveguide width are fixed in 30μm and 500 nm, respectively). Fig. 5.10 shows the simulation results of excess loss versus different Wslab values. Decreasing Wslab to 350 nm at zero voltage induces about 2dB/cm more loss.

For Wslab = 750 nm and pn-offset of 0, 50, 100 nm the excess loss is shown in Fig. 5.11. As expected, by increasing the pn-offset the pn loss decreases (holes create less loss) and the modulation efficiency increases. On the other hand, lower losses increase the quality factor, and as a result decrease the bandwidth. The choice of pn-offset requires a trade-off between the speed and modulation efficiency.

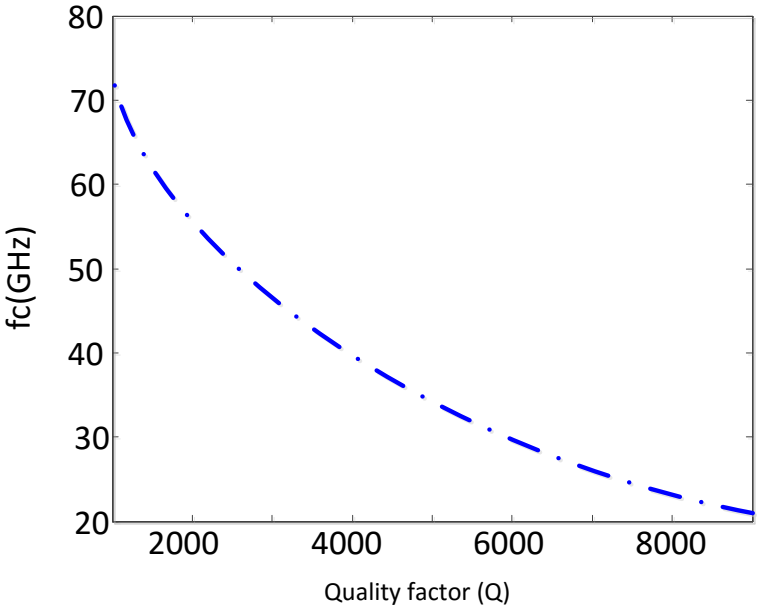

Fig. 5.9: Numerical results for cut off frequency response versus total Q-factor

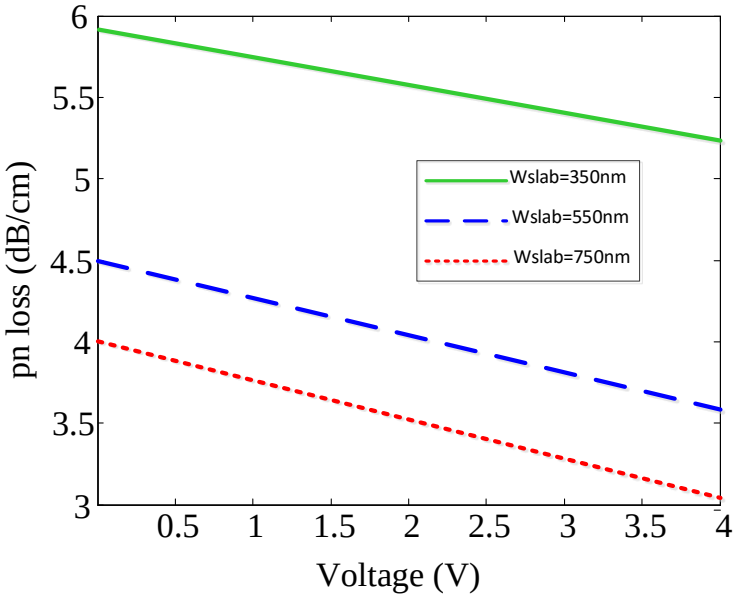

Fig.5.10: Numerical results for excess loss as a function of applied voltage (reverse bias)for various wslab. (pn-offset=0)

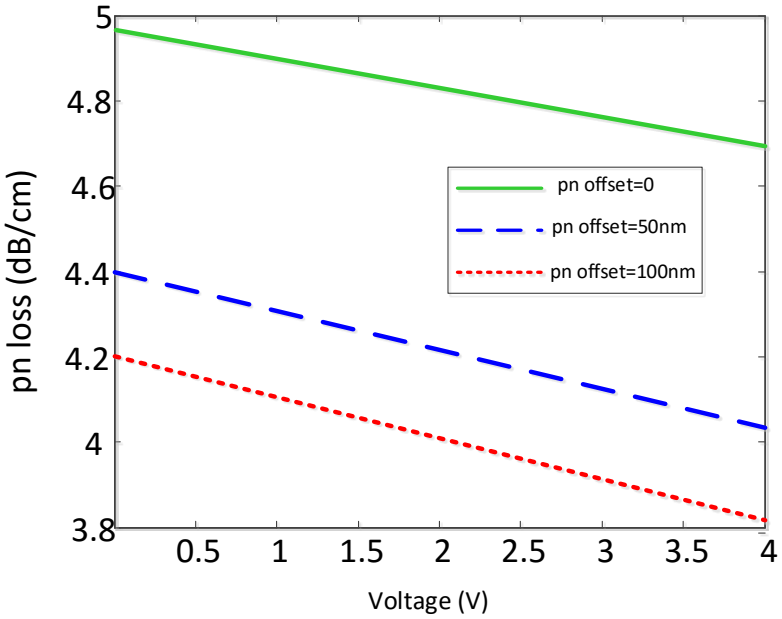

Fig.5.11: Numerical results for excess loss as a function of applied voltage (reverse bias) at various pn_offset. (Wslab=750nm)

The only degree of freedom left here is coupling coefficient. For an example, a coupling coefficient of k = 0.3 is needed to induce a quality factor around 8000 which results in 20 GHz bandwidth as shown in Fig.5.9. The effective index of the first and second super modes of the coupler structure in ring modulator is calculated in Lumerical Mode (Fig.5.12 and 5.13). Using these data, the coupling length (L_c) for k=0.3 has been calculated to be around 10 µm, the coupler is designed to work near critical condition.

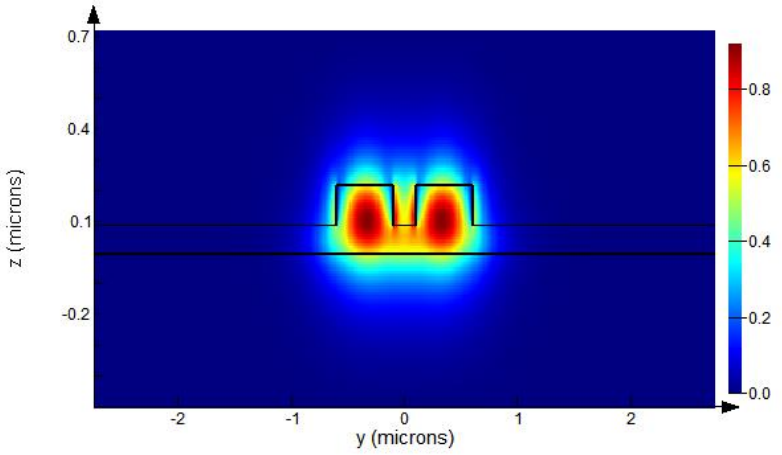

Fig. 5.12: Simulation result; electric field of the first super mode of the directional coupler structure.

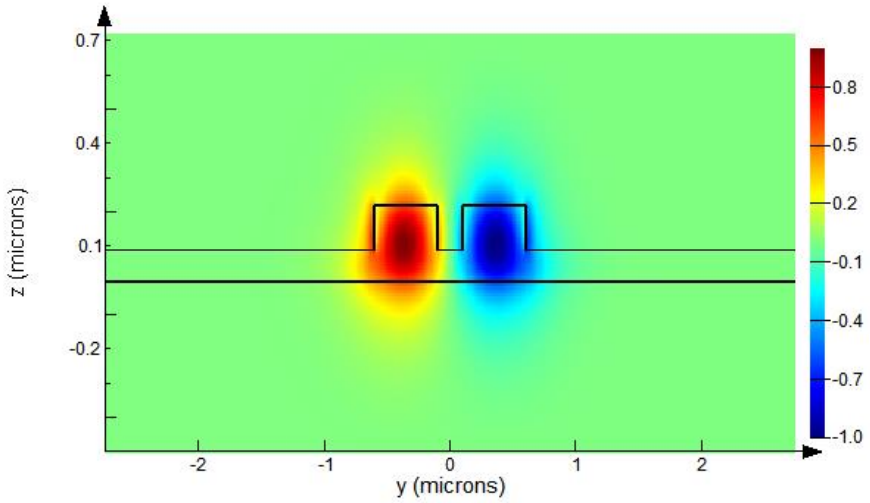

Fig. 5.13: Simulation result; electric field of the second super mode of the directional coupler structure.

Finally, the calculated through-port response for reverse bias voltage between 0 and 4 V is shown in Fig. 5.14. When the applied voltage (reverse biased) changes from 0 to 4V, the transmission drops by about 6 dB. In order to improve the modulation efficiency, we can increase the quality factor to make the transmission notch narrower. However, a higher *Q* means a longer photon lifetime, which will limit the frequency response of the modulator.

In general the following steps should be taken into account in design of the RRM: First we calculate the quality factor of the ring for the target modulation bandwidth. Then we calculate the design parameters to match the required *Q* and FSR: radius, and coupling coefficients. At this point, the optical transfer function can be verified and optimized, and a time-domain model can be constructed. Finally, the physical structure needs to be calculated, specifically the directional coupler for a desired coupling coefficient.

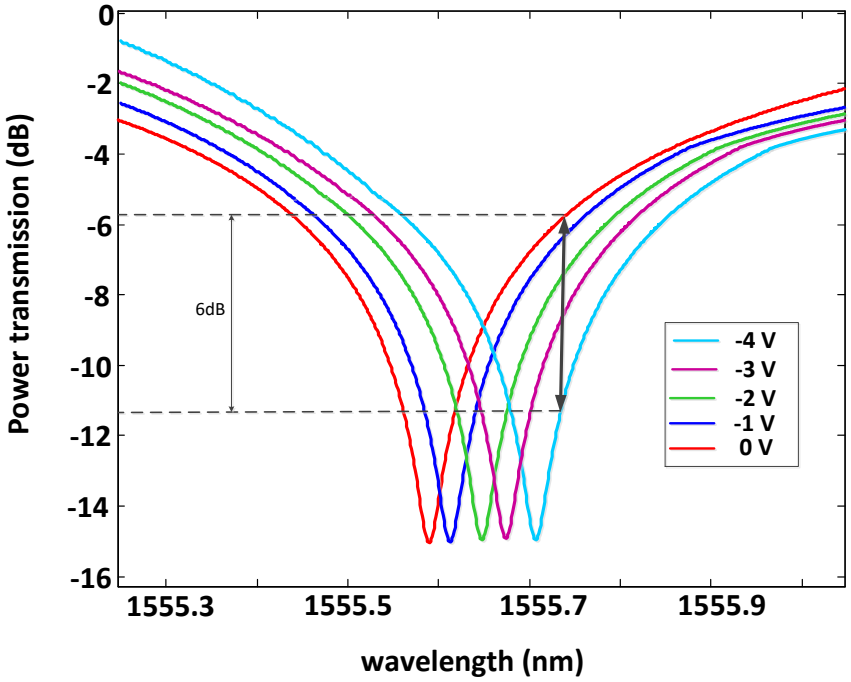

Fig.5.14: Numerical results for through port response versus wavelength for reverse bias voltage.

5-5. Small signal modulation in RRM

Fig .5.15 shows the basic MRR topology and an example of the transmission response. As discussed in detail in Chapter 3, the transmission spectra to the through port is given by

$$H(t)=\frac{E_{t1}}{E_{i1}}=\left[\frac{t-a\exp(j\varphi)}{1-ta\exp(j\varphi)}\right] \tag{5-11}$$

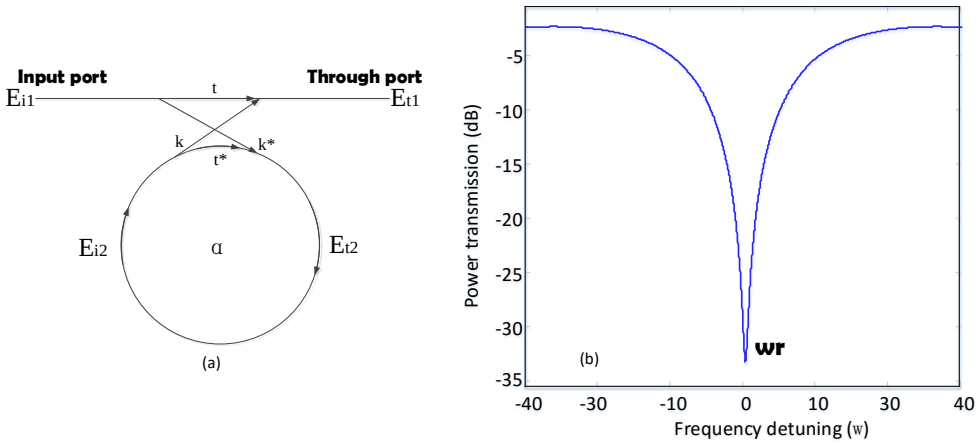

Fig. 5.15: (a) Basic MRR topology, (b) an example of transmission spectrum

The interesting features of this transmission occur around the resonant frequencies of the ring, which are located at $\omega_r = 2\pi c/(nL)$, L is the ring circumference. Optical modulation is achieved in a microring resonator by varying the parameters of its transfer characteristics, such as the resonant frequency or the coupling coefficient. For example, Fig. 5.16 shows that when the resonant frequency is shifted by $\delta = \omega - \omega r$, due to a applied voltage, then the transmission of the optical carrier is modified by $\Delta|Ht|^2$, which gives rise to intensity modulation.

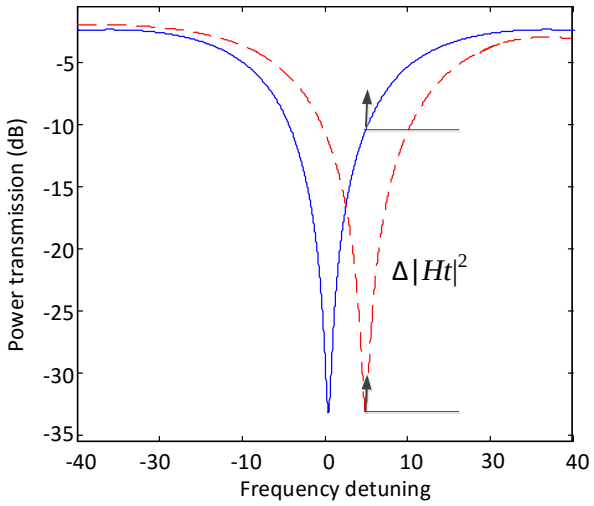

Fig.5.16: Transmission ($|Ht|^2$) as a function of the detuning from resonance $\delta = \omega - \omega r$.

In order to derive the optical response of the modulator, we start with the equations introduced in [78]

$$\frac{da}{dt} = (-i\omega_r - \frac{1}{\tau a})a + i\mu E_{i1} \qquad (5\text{-}12)$$

$$E_{t1} = E_{i1} + i\mu a \qquad (5\text{-}13)$$

where a is the amplitude of the field travelling inside the resonator, ω_r the resonant frequency of the resonator, τ_a the 1/e decay time of the field amplitude and μ the coupling strength between the resonator and the bus waveguide. By applying the sinusoidal drive voltage $\delta V \sin(\omega_m t)$ the resonant frequency of the resonator is shifted to $\omega_r + \delta\omega_r.\sin(\omega_m t)$,

where the nonlinearity of the transfer function is neglected. By assuming δV and $\delta\omega_r$ to be small quantities, the small signal response of the modulator is given by

$$S_{21} = \mu \mathrm{Re}\left(\left[\frac{\delta\omega_r \bar{a}(\bar{E}_{i1} + i\mu\bar{a})^*}{\frac{1}{\tau_a} - i\omega_m - (i\omega_0 - i\omega_r)} + \frac{\delta\omega_r^* \bar{a}^*(\bar{E}_{i1} + i\mu\bar{a})}{\frac{1}{\tau_a} - i\omega_m + (i\omega_0 - i\omega_r)} \right] e^{-i\omega_m t} \right) \qquad (5\text{-}14)$$

ω_0 is the frequency of the continuous wave optical carrier incoming from the laser, $E_{i1} = \bar{E}_{i1} e^{-i\omega_0 t}$ and $\bar{a}e^{-i\omega_0 t}$ is the value of a in the absence of modulation voltage. The two additive terms of equation (5-14) are correspondent to the generation of two side bands, which confirm the application of this RRM as an intensity modulator. The high modulation efficiency can be achieved when the laser frequency ω_0 is close to the cavity resonance ω_r.

5-6. Experimental results for fabricated RRM

Dual-bus RRM with a 30 μm radius is fabricated at the Institute of Microelectronics (IME). The starting material is an 8" SOI wafer with a Boron-doped top silicon layer of around 10 ohm-cm resistivity, a 2 μm bottom oxide thickness, and a 750 ohm-cm handle silicon wafer, needed for RF performance [79]. The image of the fabricated device is shown in Fig. 5.17. Fiber-coupling is achieved with grating couplers. The RRM is probed with standard ground-signal-ground (GSG) RF probes. An experimental set up is shown in Fig 5.18 to measure the electro-optic (E/O) S21 parameter of the RRM. An external high bandwidth photo-detector is used to convert the modulated optical signal back into RF input for a vector network analyzer. The E/O S21 of the RRM is shown in Fig.5.19. The 3dB bandwidth is measured at 0 V dc bias. The bandwidth is about 18.2 GHz.

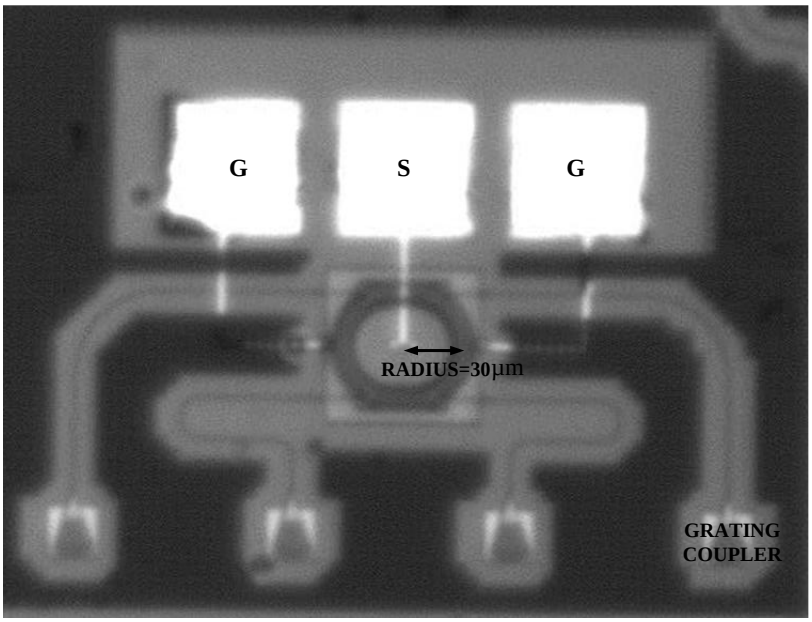

Fig.5.17: The image of the fabricated RRM

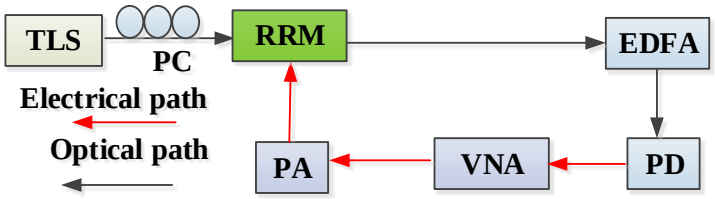

Fig.5.18: Experimental setup to measure S21 response of the RRM, TLS: tunable laser source, PC, polarization controller, VNA: vector network analyser, PA: power amplifier, RRM: ring resonator modulator

In next part we propose a simple technique to realize all-optical microwave filters with positive and negative coefficients using the above fabricated RRM. In our approach, the positive and negative coefficients are obtained by using opposite slopes of the modulation transmission response of the RRM.

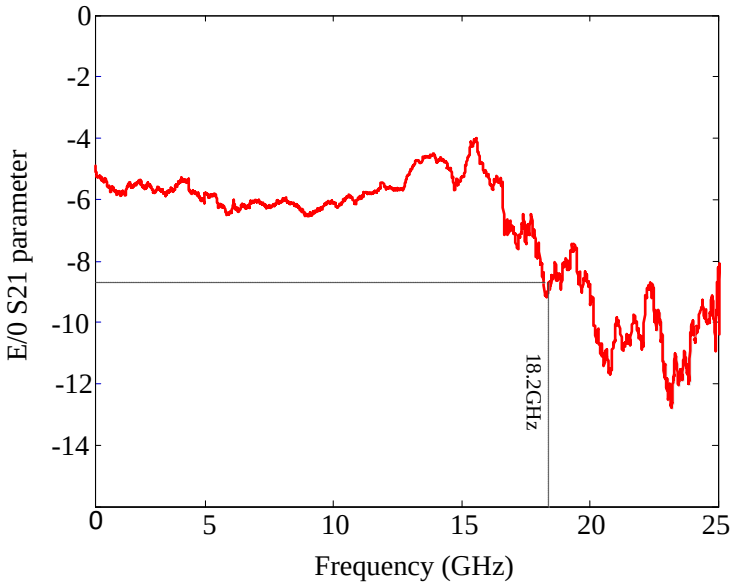

Fig. 5.19: Measured electro-optic S21 response for RRM. The device shows 18.2 GHz bandwidth.

5-7. Multiple-source microwave photonic filters (MSMPFs).

In MSMPFs, the output of an array of optical CW sources is optically combined and modulated by the RF input signal. The source array can be implemented by using an array of independent lasers. The electric field prior to RF modulation is given by

$$E(t) = \sum_{r=0}^{N-1} \sqrt{I_r} e^{j(\omega_r t + \varphi_r t)} \qquad (5\text{-}11)$$

where the number of filter coefficients, N, is determined by the number of optical wavelengths, Ir, ω_r, and $\varphi_r(t)$ represent, the optical intensity, the source central frequency, and the phase fluctuations of the rth component of the array ,respectively. Each source implements a filter sample that is selectively delayed usually by employing a dispersive medium. Fig. 5.20 shows the schematic of the MSMPF. The output electric field from impinging on the photodiode in this case is given by

$$E_o(t) = \sum_{r=0}^{N-1} \sqrt{a_r s_{in}(t - rT)} e^{j(\omega_r - rT) + \varphi_r (t - rT)} \qquad (5\text{-}12)$$

The dispersive delay element is chosen such that the differential group delay experienced by adjacent wavelengths of the source array is T. The output current from the photodiode is:

$$I_o(t) = \Re\left\langle |E_0(t)|^2 \right\rangle = \Re\sum_{r=0}^{N-1}[|a_r|s_i(t-rT)] \tag{5-13}$$

The phase variations from different optical sources can be assumed to be always uncorrelated. Thus, a linear relationship between the input and output RF/microwave signal is obtained. The amplitude of each coefficient, a_r, is controlled with the optical power of each wavelength. The main advantage of this filter architecture is a very stable response due to operation in the incoherent regime. Furthermore, the filter transfer function can be reconfigured by dynamically changing the relative power of the optical wavelengths, and it can be tuned by controlling the dispersive medium [80]. However, positive and negative filter coefficients are needed to allow a full versatility in the transfer function, thus enabling flat-pass bands or high out-of-band suppression.

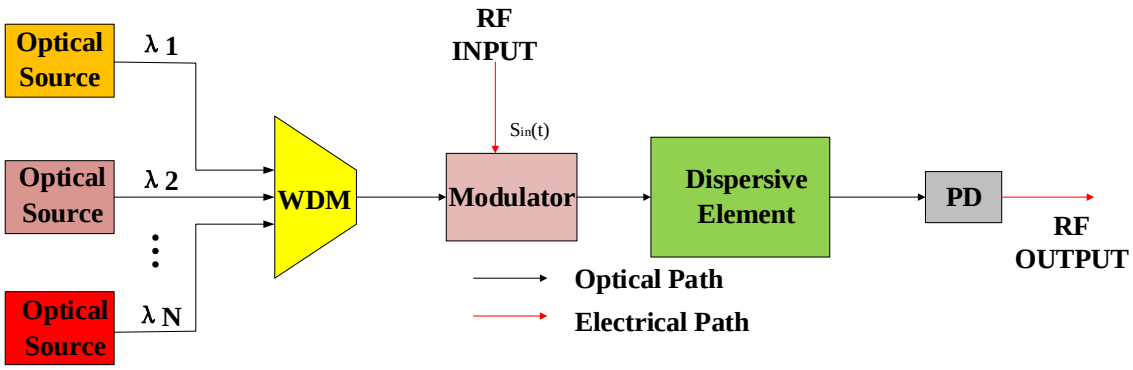

Fig.5.20: Schematic of the MSMPF, (WDM: wavelength division multiplexing)

Fig. 5.21 (a) shows the steady state transfer function of the RRM. The ring resonator is a cavity working on the principle of the constructive interference of light inside the resonator, resulting in a Lorentzian transfer function [79]. For small signal analysis, we assume that a traveling wave is circulating within the ring with constant amplitude then we can view the resonator as a lumped oscillator, the transfer function of the RRM in dynamic mode is periodic. Fig. 5.21(b) demonstrates the general RRM output power in response to a sinusoidal modulation frequency [81]. The fundamental concept for the implementation of

MWP with negative coefficients also is shown in Fig. 5.22. For instance, two optical carriers modulated by a microwave signal are placed at wavelengths that correspond with opposite slopes in the RRM response, the microwave signal after photo-detection will have the same average power but inverted phase (i.e., π-shifted) [82].

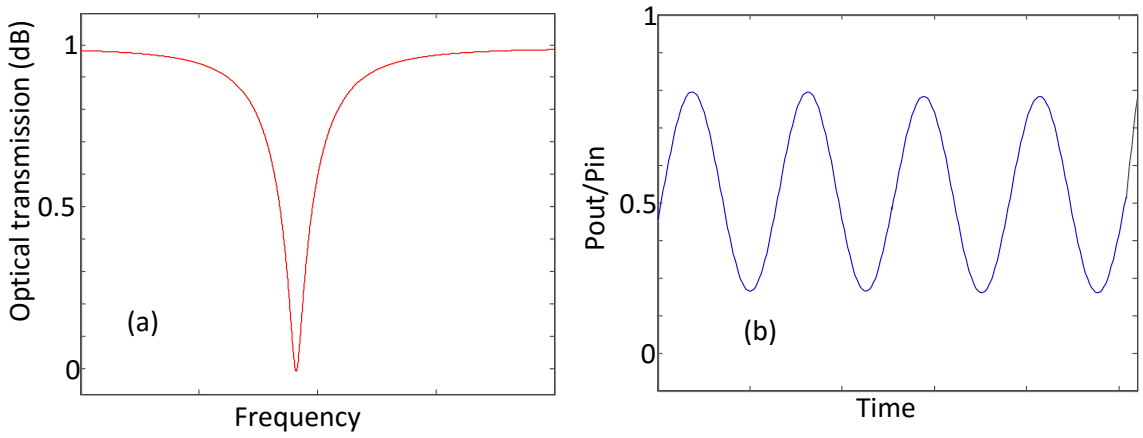

Fig. 5.21: (a) Steady state transfer function of the silicon ring modulator, (b) RRM output power in response to sinusoidal modulation frequency.

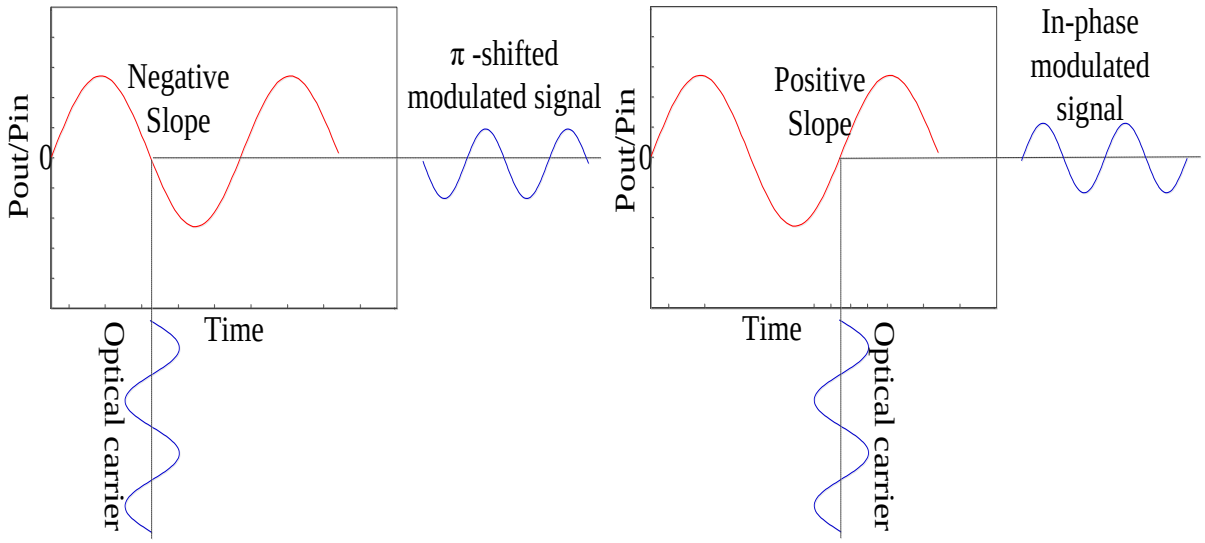

Fig. 5.22: Illustration of the phase inversion suffered by a microwave modulating signal.

5-8. Implementation of the MSMPF

The experimental setup is shown in Fig. 5.23. A set of optical continuous wave (CW) carriers are modulated by the silicon RRM. The RF signal from a VNA is combined with the DC bias using a bias-Tee and applied to the modulator through a broadband GSG probe. Before any measurement is made, we adjusted the power and the polarization state of each source to obtain the same average output power from the RRM for each wavelength, to guarantee the uniformity of all the samples. By choosing the wavelength of the optical carriers, it is possible to control the sign of the corresponding filter coefficient. Fig. 5.24 shows the measured transmission response of the RRM. The optical carriers modulated by a microwave signal are placed at wavelengths that correspond with opposite slopes to implement a microwave filter with positive and negative coefficients. After modulation, the signals are amplified with an EDFA and launched to a dispersive medium which in this case is done with a 10-km coil of standard single-mode fiber (SMF-28 fiber).

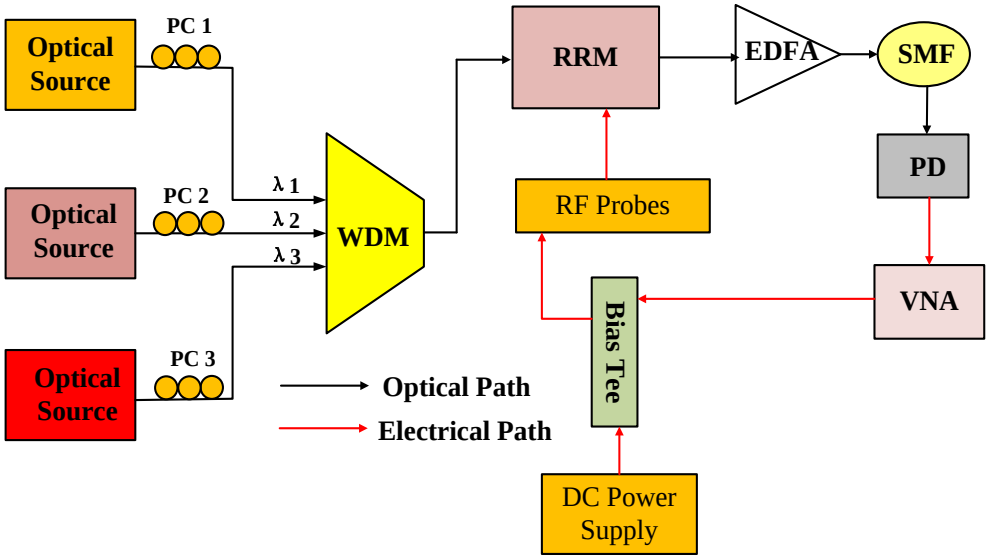

Fig.5.23: Experimental setup for three-tap microwave photonic filter architecture. RRM: ring resonator modulator, SMF: single mode fiber, VNA: vector network analyser, WDM: wavelength division multiplexer.

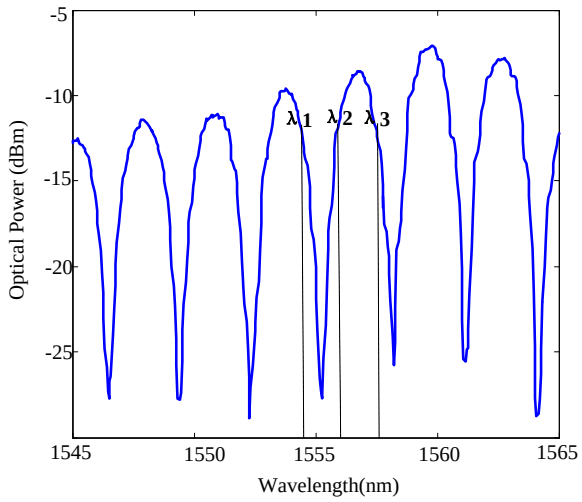

Fig.5.24: Measured RRM response (λ1, λ2 and λ3 show the location of the optical carriers in different slopes)

The fiber coil provides a dispersion of 17 ps/(nm.km), which, for a wavelength separation of 1.5 nm between adjacent carriers, corresponds to a time delay between adjacent samples of 255ps or, in other words, a free spectral range of 3.9 GHz for the RF filter. Then, the optical signal is photo-detected and injected into the VNA input for measurement of the filter transfer function. Fig. 5.25 shows the normalized filter response between 0-20 GHz when two optical carriers (λ_1=1554.5 nm and λ_2=1556nm) enter the modulator with the same output power at the input of the photodiode. These wavelengths are placed at the opposite slopes of the modulator response. Both the experimental (solid curves) and the theoretical (dashed curves) results are shown for reference and comparison. As expected, the filter resonance at baseband (typical of positive coefficient filters) has been eliminated, thus confirming the feasibility of the proposed scheme for the implementation of negative coefficients. The filter's free spectral range is close to 3.9 GHz, as predicted. Fig.5.26 shows the filter response when three optical carriers (1554.5, 1556, and 1557.5nm) are fed to the modulator. The RRM shows up to 18 GHz bandwidth and the measurement has been done between 0 to 20 GHz. At higher frequencies, the agreement is reduced due to an unbalance in the modulation efficiency between optical carriers and the higher accuracy needed in time-delay among taps.

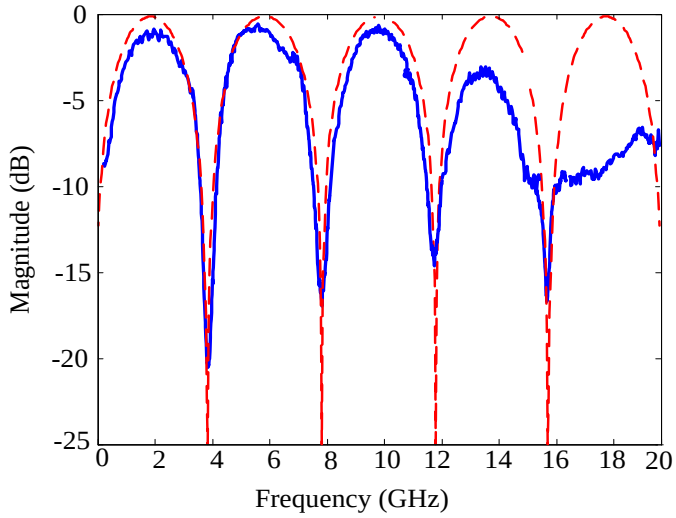

Fig.5.25. Experimental result for two-tap filter response with negative coefficient. (The solid line represents the experimental results and the dotted the theoretical estimation).

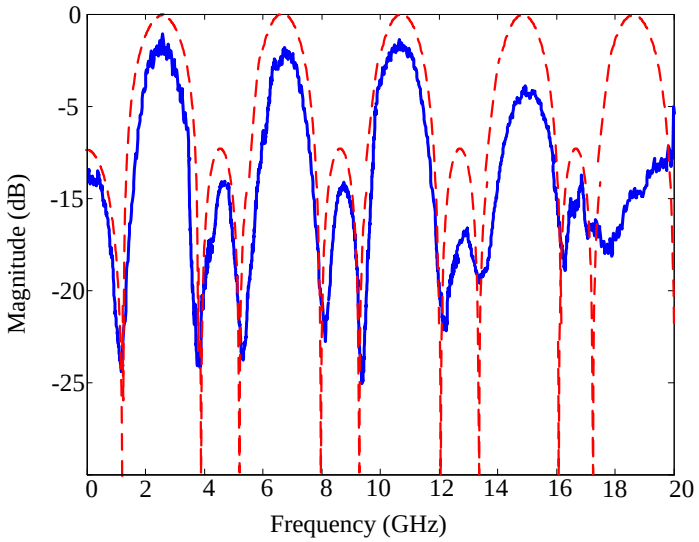

Fig.5.26: Experimental result for three-tap filter response with negative coefficient. (The solid line represents the experimental results and the dotted the theoretical estimation).

In conclusion, we demonstrated an approach to the implementation of MWP filter that was based on the phase inversion that a microwave modulating signal suffered in a RRM, depending on whether the positive or the negative linear slope of its modulation transfer function was employed. Experimental evidence of the feasibility of this approach was provided. RRM-based MWP filter has the advantages of simple configuration, small package, and easy to integrate. Also, RRM has lower power consumption and drive voltage compared to MZM-based MWP filters.

CHAPTER 6 MICROWAVE FREQUENCY MULTIPLICATION BASED ON ENHANCED FOUR WAVE MIXING IN AN ACTIVE SILICON WAVEGUIDE

6-1. Optically generation of microwave signal

In many microwave systems such as broadband wireless networks, and radar systems, a high- quality millimeter-wave (mm-wave) source is essential [1]. External modulation for frequency multiplication enjoys good tunability and simplicity, and thus becoming one of the most important methods for generating microwave signals at high frequencies. With external modulation method, normally a low frequency microwave signal is modulated onto an optical carrier to generate high order optical sidebands, and different methods are adopted to amplify the sidebands with desirable frequencies. In addition to the use of an external modulator to generate higher order sidebands (or phase-correlated multiple wavelengths), the use of four-wave mixing (FWM) in highly nonlinear fiber (HNLF) [83] or a semiconductor optical amplifier (SOA) [84] can also generate phase correlated multiple wavelengths to achieve microwave frequency multiplication. Recently, silicon photonics has been extensively investigated for microwave signal generation [29], [30]. Among the many different components, a silicon waveguide is a fundamental component which can be used not only to guide light waves in a silicon circuit, but also achieve various functions thanks to the strong light confinement due to a high refractive-index contrast. For example, optical nonlinear effects can occur in a silicon waveguide even in a relatively low input optical power. Light propagation in the waveguide can produce a wide variety of nonlinear phenomena, including self-phase modulation (SPM), cross phase modulation (XPM), two-photon absorption (TPA), and four-wave mixing (FWM). In the past few years, all-silicon active optical devices have been extensively studied in connection with these nonlinear effects [85]. On the other hand, extensive efforts have been directed to the generation of high frequency and low phase noise microwave or mm-wave signals based on photonics.

In this part, we propose an approach to implementing microwave frequency multiplication

based on enhanced FWM in an active silicon waveguide (SiWG). A SiWG-based FWM has the advantages of simple configuration, small package, and easy to integrate. The system mainly consists of an active SiWG and a LiNbO3 intensity modulator (MZM).

6-2. Four wave mixing effect in SiWG

All-optical wavelength conversion based on four–wave mixing (FWM) in silicon waveguides is an attractive area. As is well known that efficient FWM occurs only when phase-matching condition is satisfied [86] [87]. Fig. 6.1(a) illustrates the perspective view of the proposed active SiWG. It is fabricated on a silicon-on-insulator (SOI) substrate with a bottom silica layer of 2-μm in thickness. The cladding layer of silica is removed in Fig. 6.1(a) to clearly illustrate the internal structure of the device. To reduce the nonlinear optical loss due to the TPA-induced FCA, a lateral p-n structure is adopted which is reversed bias. Additional p++ and n++ implantations are utilized for electrode contact. The SiWG has a straight waveguide of 6 mm long with an embedded p-n structure. Silicon rib waveguide with 500-nm in width, 220-nm in height, and 90-nm in slab thickness is employed to ensure a single fundamental TE mode operation, as shown in Fig. 6.1(b). A major limitation for high conversion efficiency is the strong nonlinear absorption that occurs at high pump powers. Although linear optical absorption in silicon at wavelengths of 1.3-1.7 μm is small, two-photon absorption (TPA) induced free carrier absorption (FCA) causes the optical loss to increase with the pump power. We have demonstrated that the TPA induced FCA in silicon can be significantly reduced by introducing a reverse biased p-n diode structure embedded in a silicon waveguide [88]. The p and n implants are performed on the exposed silicon, prior to any oxide fill. It is followed by the formation of contact vias and two levels of aluminum (Al) interconnect for electrical connection. The in and out coupling is achieved through standard grating couplers. The waveguides is designed with three different lengths: a straight waveguide of 6mm long which the p-n structure is embedded in this length, two straight waveguide of 600 μm for connection to grating couplers and two curve of radius 50 μm. This device is probed with standard ground-signal-ground (GSG) probe to introduce a reverse DC bias into the system.

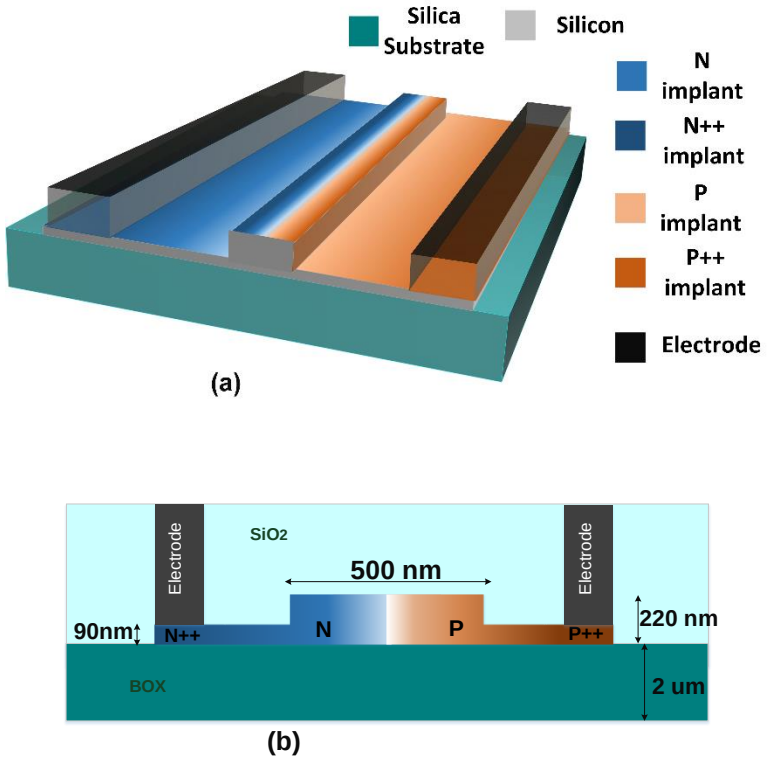

Fig.6.1. (a) Perspective view of the SiWG, (b) a cross-sectional view of the SiWG, The clad is covered by silica layer (SiO2). (BOX: buried oxide).

A schematic of the experimental setup is shown in Fig. 6.2. The pump and signal are combined with a 3dB coupler into erbium doped fiber amplifier (EDFA). The output of the EDFA is coupled into a SIWG via a single mode fiber. Fig. 6.3 is a typical spectrum of the output beam from the SIWG. According to the theory of FWM the pump and the input signal (λ_1, λ_2), mix together to create new wavelengths ($\lambda_3=2\lambda_2-\lambda_1$ and $\lambda_4=2\lambda_1-\lambda_2$). Such FWM components will grow with increased input signal and pump powers. For easy comparison with other published works, we follow the definition of wavelength conversion efficiency as the ratio between the peak levels of the converted signal at $\lambda 3$ and the original signal at λ_1 in Fig. 6.3. The conversion efficiency shown here is -25 dB (Fig.6.3. blue line) with pump power of 27dBm into the waveguide. At high pump powers, two-photon absorption (TPA) generates free carriers in the waveguides. In the TPA process, two photons are absorbed simultaneously and an electron-hole pair is created in the silicon waveguide. These generated carriers cause additional optical loss. This nonlinear absorption starts to reduce the effective pump power and the conversion efficiency drops. By applying the reverse bias to the p-n structure in the waveguide, sweeping out the two-photon absorption generated free carriers,

the conversion efficiency significantly increases. The conversion efficiency of -19 dB is obtained by applying -20V DC bias. (Fig.6.3. redline). The TPA induced free carriers absorption (FCA) in silicon can be significantly reduced by introducing a reverse biased p-n structure embedded in a silicon waveguide, shortening the free carrier life time. In the next section, we have used this characteristic to generate mm-wave signal based on the enhanced FWM in active SiWG.

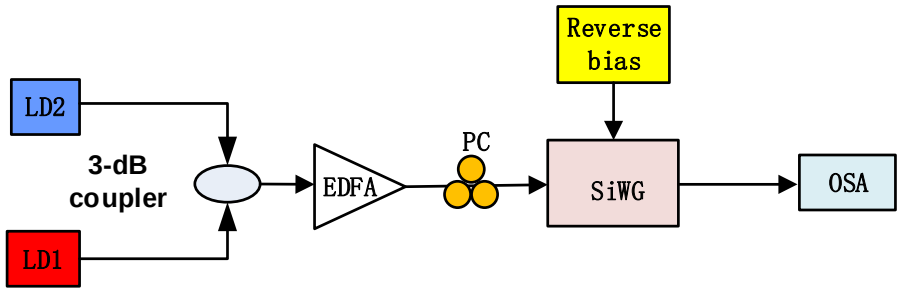

Fig.6.2: Schematic experimental set up of the FWM effect in SiWG

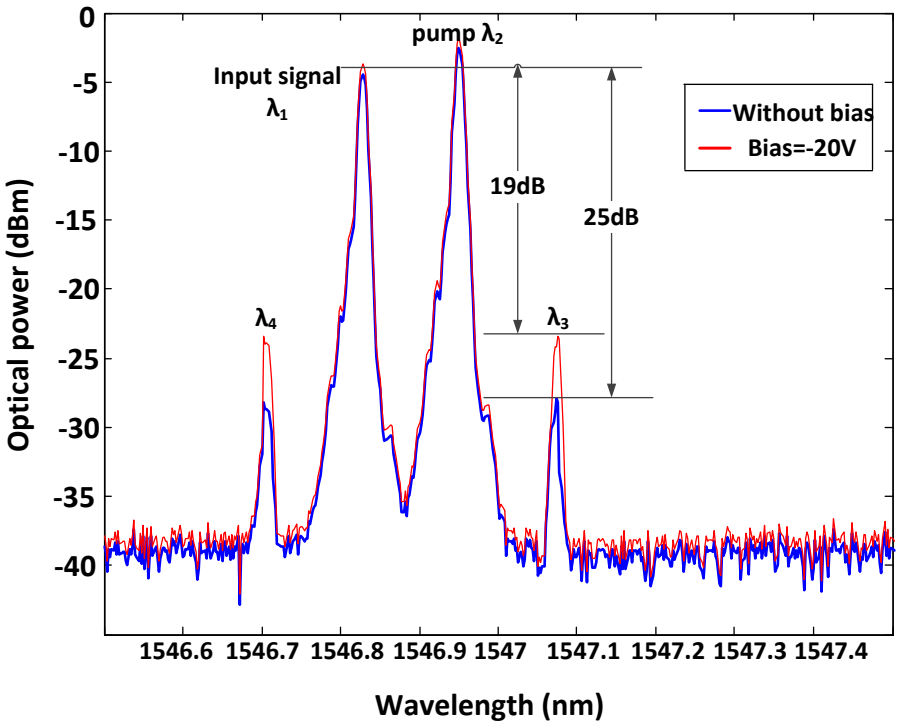

Fig.6.3. Spectrum of the output beam from SiWG. Pump power is 27dBm

6-3. Microwave signal generation based on enhanced FWM in an active SiWG

The configuration of the proposed mm-wave generation system is shown in Fig. 6.4. A microwave signal is applied to the LiNbO3 modulator (MZM), which is biased by $V_\pi/2$ in order to achieve carrier suppression. The field of the light source is $E_{in} = A_{in}\exp[j\omega_0 t + \varphi_0(t)]$ and the microwave signal is $\phi(t) = V_\pi / 2\sin(\Omega t + \psi_0(t))$, where $\varphi_0(t)$ phase noise of the input light, $\psi_0(t)$ phase noise of the microwave signal and V_π is the half wave voltage. Considering that the higher order sidebands have much lower power than the first-order sidebands, the optical signals mainly consists of only two first-order sidebands. The optical signal at the output of the MZM can be written as

$$E_{out} \approx -j\frac{A_{in}}{2}\exp[j(\omega_1 + \varphi_1(t)]\exp(-j\beta L) - j\frac{A_{in}}{2}\exp[j(\omega_2 + \varphi_2(t)]\exp(-j\beta L) \quad (6\text{-}1)$$

where

$$\omega_1 = \omega_0 + \Omega, \quad \omega_2 = \omega_0 - \Omega$$
$$\varphi_1(t) = \psi_0(t) + \varphi_0(t), \quad (6\text{-}2)$$
$$\varphi_2(t) = -\psi_0 + \varphi_0(t) + \pi$$

Because both optical pumps are derived from the same single source, the phase noise $\varphi_1(t)$ and $\varphi_2(t)$ are totally correlated and $\varphi_2(t) - \varphi_1(t) = -2\psi_0(t) + \pi$. The two first-order sidebands in ω_1 and ω_2 at the output of the $LiNbO_3$ are amplified by an EDFA, and are sent to the SiWG. Based on FWM theory; two new frequencies in ω_3 and ω_4 are generated. The frequency and phase noise of the generated signal can be written as

$$\omega_3 = 2\omega_1 - \omega_2 = \omega_0 + 3\Omega, \quad \omega_4 = 2\omega_2 - \omega_1 = \omega_0 - 3\Omega \quad (6\text{-}3)$$

$$\varphi_3(t) = 2\varphi_1(t) - \varphi_2(t) = 3\psi_0(t) + \varphi_0(t) - \pi$$
$$\varphi_4(t) = 2\varphi_2(t) - \varphi_1(t) = -3\psi_0(t) + \varphi_0(t) + 2\pi \quad (6\text{-}4)$$

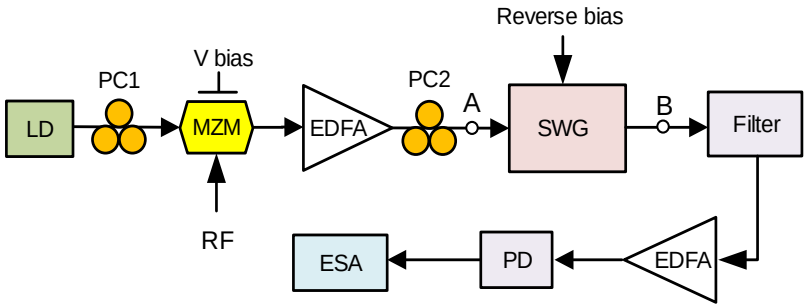

Fig.6.4: Schematic diagram of the mm-wave generation (LD: Laser Diode, PC: Polarization Controller, MZM: Mach-Zehender modulator, EDFA: Erbium-doped Fiber Amplifier, SIWG: silicon waveguide, PD: Photodetector, ESA: Electrical Spectrum Analyzer)

The phase difference between the two idlers is given by $\varphi_3(t)-\varphi_4(t)=3\varphi_1(t)-3\varphi_2(t)=6\psi_0(t)-3\pi$. Thus the phase noise of the beat signal is independent of the phase noise of the light source and is six times the phase noise of the microwave reference signal due to the frequency sextupling. The phase noises of the two mixing waves are correlated, and the phase noise of the beat signal is only determined by the driver signal, which is always as narrow as several Hertz. In our experimental setup, the laser diode (LD) output is set at 1549.9 nm, and the MZM is driven by a microwave signal at 4GHz. The spectrum at the point A is shown in Fig. 6.5(a). It can be seen that the optical carrier is suppressed, and the two first-order sidebands have same power levels, which are about 30 dBm higher than the other higher order sidebands.

The optical spectrum at the output of the SiWG, at point B, is shown in Fig. 6.5 (b). Two idlers are generated due to FWM in the SiWG. In high input power, free carriers would be generated in the SiWG due to the TPA effect. In a TPA process, two photons are absorbed simultaneously to produce an electron-hole pair. These generated free carriers would cause additional optical loss. This nonlinear absorption starts to reduce the effective input power and the conversion efficiency drops. By applying a reverse bias to the p-n structure in the waveguide, to sweep out the TPA-generated free carriers, the conversion efficiency would significantly increase. The SiWG is biased at -20 V to achieve a maximum conversion efficiency, as shown in Fig. 6.5 (c). The conversion efficiency has been increased by about 6 dB. The wavelength spacing between the two idlers is 24 GHz, which is six times the frequency of the microwave reference signal. The optical signal at the output of the SiWG is sent to the optical filter to remove the two pump waves. After amplification by EDFA2, the

two idlers are applied to the PD (50 GHz, DSC10ER) to generate a frequency sextupled microwave signal, which is monitored by an electrical spectrum analyser (ESA, Keysight, E4448A).

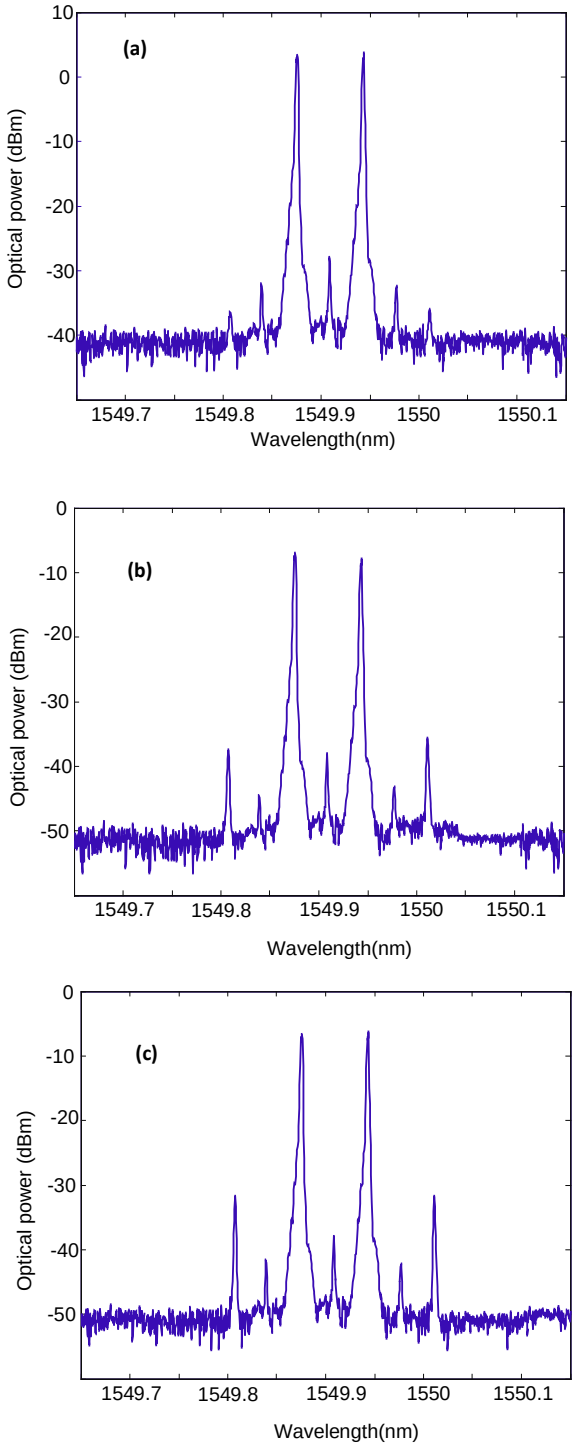

Fig.6.5: (a) Optical spectrums (a) at the output of the MZM (point A), (b) the output of the SiWG (point B) without bias and (c) the output of the SiWG (point B) with the reverse bias voltage of -20 V.

Fig. 6.6 shows the spectrum of the generated frequency sextupled signal at 24 GHz without bias (red line) and in -20 V bias (blue line). As can be seen the microwave signal generation efficiency has been improved by about 8 dB. The spectral width is ultra-narrow, which is only dependent on the spectral width of the microwave reference source. The phase noise from the light source from the LD is fully cancelled, which ensures a good phase noise performance. To compare the phase noise between the generated microwave signal with maximum efficiency and the microwave reference signal, the phase noises of the two signals are measured, which are shown in Fig. 6.7. As can be seen the generated frequency sextupled signal at 24 GHz has a phase noise of around -85 dBc/Hz at a 10-kHz offset, which is about 15-dB higher than that of the 4-GHz microwave reference signal. Theoretically, the phase noise of a frequency-sextuple signal will have a phase noise degradation of about $10\log_{10} 6^2 \approx 15\ dB$ as compared with its reference signal.

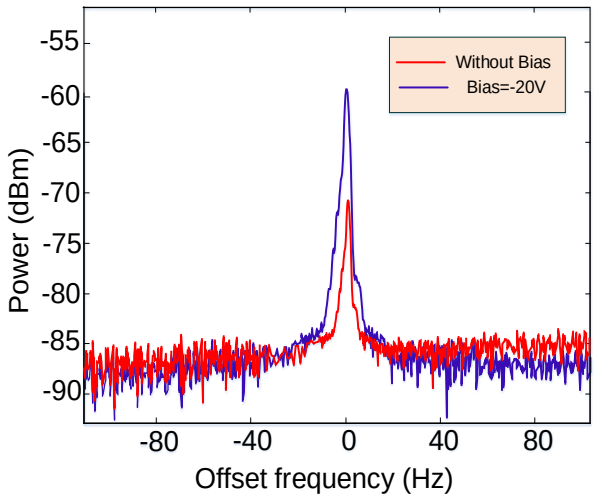

Fig.6.6. Spectrum of the generated frequency sextupled microwave signal at 24 GHz without bias and with the reverse bias voltage of -20 V.

In conclusion, the generation of a frequency-sextupled microwave signal based on FWM in an active SiWG was experimentally demonstrated. The key contribution of the work was the use of the active SiWG that was designed to have a p-n junction across the SiWG. When the p-n junction was reversed biased, the conversion efficiency of the FWM was improved, which led to the improvement in the frequency multiplication efficiency. An active waveguide was fabricated on a SOI substrate and was used to achieve frequency multiplication to generate a frequency-sextupled microwave signal. When a microwave

reference signal at 4 GHz was applied to the MZM, a frequency-sextupled microwave signal at 24 GHz was generated. The phase noise of the generated signal was independent of the light source and only dependent the phase noise of the microwave reference source. For a microwave reference source with a phase noise of 100 dBc/Hz at 10-kHz offset, the phase noise of the frequency sextupled microwave signal was -85 dBc/Hz at 10-kHz offset. The frequency multiplication efficiency was improved by about 8 dB when the p-n junction was reversed biased by a bias voltage of 20 V. The proposed system can be improved by integrating the MZM, the optical filter and the PD in a single chip to minimize the size and the coupling losses.

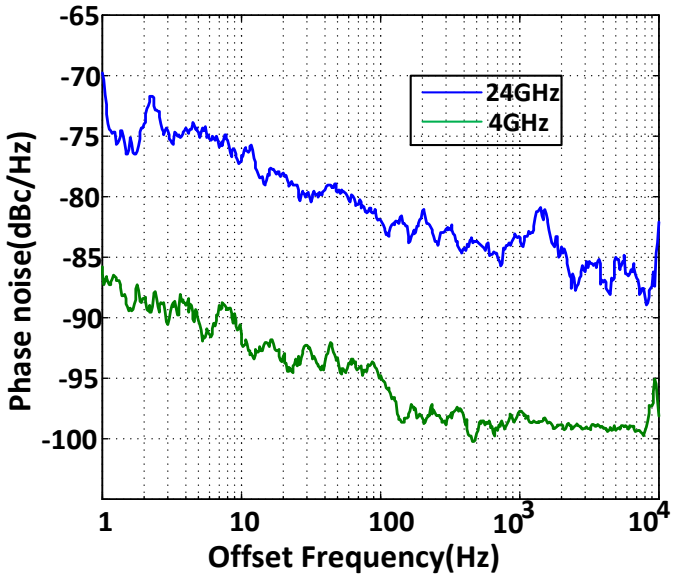

Fig.6.7. Phase noise of the 4-GHz signal from the microwave source and the generated 24.0-GHz signal

CHAPTER 7 SUMMARY AND FUTURE WORK

7-1. Summary

This research focused on the silicon photonic design for microwave photonic signal generation and processing. The design procedures of passive and active devices including strip and rib waveguide, directional coupler, ring resonator were studied. A single pass-band and frequency-tunable MWP filter based on PM-IM conversion in an SOI MRR was proposed and experimentally demonstrated. The fundamental concept of the approach was to filter out one sideband of a phase-modulated signal, to convert the phase-modulated signal to an intensity-modulated SSB signal. The optical carrier and the first-order sideband were then applied to a photodetector. The beating between these two components generated a microwave signal which was equivalent to a pass-band filter response with the central frequency tunable by tuning the resonance wavelength of MRR. A tunable MWP phase shifter based on three cascaded SOI MRRs was proposed and experimentally demonstrated. The phase tuning was implemented by tuning the phase response through optical pumping. Due to the TPA-induced TO effect, the phase response was tuned. The use of the fabricated MRRs to implement a broadband microwave photonic phase shifter with a bandwidth of 7 GHz from 16 to 23 GHz with a tunable phase shift covering the entire 360^{o} phase shift range was demonstrated. Four wave mixing (FWM) effect in silicon waveguide was studied and a silicon waveguide with lateral PN junction was designed to generate microwave signal based on enhanced FWM. With reverse biasing this waveguide the loss corresponding with two photon absorption decreased and the FWM conversion efficiency increased. Modulators are one of the key components in microwave photonic systems. Conventional modulators based on LiNob3 and III-V are large and bulky which leads to high power consumption in the system. Silicon photonic provides the opportunity to design and fabricated a modulator in micrometer size. A RRM with 18.2 GHz bandwidth which worked based on carrier depletion effect was designed and fabricated. This modulator used to implement a multi tap microwave photonic filter with positive and negative coefficients.

7-2. Future works

Limitations of the MWP system (high cost, bulkiness, high power consumption etc.) can be removed by realization of entire functionalities (filtering, phase shifting, modulation, detection) on a chip. In Chapter 3 we demonstrated a single pass-band MWP filter using a discrete phase modulator cascaded with a SOI MRR. The system was still bulky. Integration of the SOI phase modulator and MRR in single chip can be a good approach to reduce the size and power consumption of the system.

Optical comb generation on a chip [89] has drawn too much attention in microwave photonics as it enables several applications such as wavelength division multiplexing (WDM) networks [90], optical arbitrary waveform generation (O-AWG) [91], and rapid arbitrary millimeter wave generation [92]. A suitable approach for frequency comb generation is based on periodic modulation of a continuous-wave (CW) laser. The number of comb lines depends on the modulation depth and the number of cascaded devices. Up to now most of the reported comb generators are based on discrete components such as MZM and phase modulator [93-95], the system is so bulky, costly, and power consuming. Integration of the SOI modulators on a single chip for comb generation [96], [97] can reduce the size of the system significantly. As a part of this research work we designed a RRM as an intensity modulator cascaded with phase modulator on a single chip for comb generation. The size of the chip was 6mm×3mm, which was significantly small compared to discrete modulators. The bandwidth and modulation efficiency of the designed modulators was not high enough for comb generation. This design can be improved by increasing the modulation efficiency of the cascaded SOI modulators. For example the modulation efficiency of the RRM improved by increasing its Q-factor. The resistance of the PN junction in SOI modulators is another important parameter that can be reduced by optimizing the doping concentrations and the distances between dopants and junction. Minimizing the distance between the contact and junction will lead to a reduced *RC* time constant and eventually increase the bandwidth of the modulator.

LIST OF REFERENCES

[1] J. P. Yao, "Microwave photonics," *J. Lightw. Technol*., vol. 27, no. 3, pp. 314-335, Feb. 2009.

[2] R. A. Minasian, E. H. W. Chan, and X. Yi, "Microwave photonic signal processing," *Opt. Express*., vol. 21, no. 19, pp. 22918-22936, Aug. 2013.

[3] J. Capmany, J. Mora, I. Gasulla, J. Sancho, J. Lloret, and S. Sales, "Microwave Photonic Signal Processing," *J. Lightw. Technol*., vol. 31, no. 4, pp. 571-586. Feb. 2013

[4] I. Gasulla, J. Lloret, J. Sancho, S. Sales, and J. Capmany, "Recent Breakthroughs in Microwave Photonics," *IEEE Photonics J*., vol. 3, no. 2, pp. 311–315, Apr. 2011.

[5] J. Capmany, I. Gasulla, and S. Sales, "Microwave photonics, harnessing slow light," *Nature Photon.*, vol. 5, pp. 731–733, Dec. 2011.

[6] D. Marpaung, C. Roeloffzen, R. Heideman, A. Leinse, S. Sales, and J. Capmany, "Integrated microwave photonics," *Laser Photonics Rev*., vol. 7, no. 4, pp. 506–538. Jan. 2013.

[7] M. Smit, J. van der Tol, and M. Hill, "Moore's law in photonics," *Laser & Photonics Rev*, vol. 6, no. 1, pp. 1–13, Jan. 2012.

[8] L. Coldren, S. Nicholes, L. Johansson, S. Ristic, R.Guzzon, E. Norberg, and U. Krishnamachari, "High Performance InP-Based Photonic ICs—A Tutorial," *J. Lightw. Technol*., vol. 29, no. 4, pp. 554–570, Feb. 2011.

[9] S. Koehl, A. Liu, and M. Paniccia, "Integrated silicon photonics: Harnessing the data explosion," *Opt. Photon. News*, vol. 22, no. 3, pp. 24–29, Mar. 2011.

[10] K. K. Lee, D. R. Lim, L. C. Kimerling, J. Shin, and F. Cerrina, "Fabrication of ultralow-loss Si-SiO2 waveguides by roughness reduction," *Opt. Lett.*, vol. 26, no. 23, pp. 1888–1891, Dec. 2001.

[11] W. M. Green, M. J. Rooks, L. Sekaric, and Y. A. Vlasov, "Ultra-compact, low RF power, 10 Gb/s silicon mach-zehnder modulator," *Opt. Express*, vol. 15, no. 25, pp. 17106–17113, Dec. 2007.

[12] S. Manipatruni, Q. Xu, and M. Lipson, "PINIP based high-speed high extinction ratio micron-size silicon electro-optic modulator," *Opt. Express*, vol. 15, no. 20, pp. 13035–13042, Oct. 2007.

[13] L. Chen and M. Lipson, "Ultra-low capacitance and high speed germanium photodetectors on silicon," *Opt. Express*., vol. 17, no. 10, pp. 7901-7906, May. 2009.

[14] H. Rong, R. Jones, A. Liu, O. Cohen, D. Hak, A. Fang, and M. Paniccia, "A continuous-wave raman silicon laser," *Nature photon*., vol. 433, pp. 725–728, Feb. 2005.

[15] J. Capmany, B. Ortega, D. Pastor, and S. Sales, "Discrete-Time Optical Processing of Microwave Signals," *J. Lightw Technol*., vol. 23, no. 2, pp. 702-723, Feb. 2005.

[16] J. Capmany, B. Ortega, and D. Pastor, "A Tutorial on Microwave Photonic Filters," *J. Lightw Technol*., vol. 24, no.1, pp. 201-229, Jan. 2006.

[17] P. Alipour et.al, "Fully reconfigurable compact RF photonic filters using high-*Q* silicon micro-disk resonators," *Opt. Express*., vol. 19, no. 17, pp. 15899-15907, Aug. 2011.

[18] D. Zhang, X. Feng, and Y. Huang, "Tunable and Reconfigurable Bandpass Microwave Photonic Filters Utilizing Integrated Optical Processor on Silicon-on-Insulator Substrate," *IEEE Photon. Technol. Lett*., vol. 24, no. 17, pp. 1502-1505, Sep. 2012.

[19] N. N. Feng, P. Dong, D. Feng, W. Qian, H. Liang, D. C. Lee, J. B. Luff, A. Agarwal, T. Banwell, R. Menendez, P. Toliver, T. K.Woodward, and M. Asghari, "Thermally-efficient reconfigurable narrowband RF-photonic filter," *Opt. Express.*, vol. 18, no. 24, pp. 24648–24653, Nov. 2010.

[20] S. Ibrahim, N. K. Fontaine, S. S. Djordjevic, B. Guan, T. Su, S. Cheung, R. P. Scott, A. T. Pomerene, L. L. Seaford, C. M. Hill, S. Danziger, Z. Ding, K. Okamoto, and S. J. B. Yoo, "Demonstration of a fast-reconfigurable silicon CMOS optical lattice filter," *Opt. Express.*, vol.19, no. 14, pp. 13245–13256, Jul. 2011.

[21] A. M. Gutierrez, P. Sanchis, A. Brimont, D. J. Thomson, F. Y. Gardes, G. T. Reed, J.-M. Fedeli, and B. Vidal, "A Photonic Microwave Filter Based on an Asymmetric Silicon Mach-Zehnder Modulator," *IEEE Photon. J.*, vol. 5, no.4, pp. 5501006, Aug. 2013.

[22] S. Yegnanarayanan, P. Trinh, F. Coppinger, and B. Jalali, "compact silicon-Based Integrated Optic Time Delays," *IEEE Photon. Technol. Lett.*, vol. 9, no, 5, pp. 634–635, May. 1997.

[23] S. Khan, M. A. Baghban, and S. Fathpour, “Electronically tunable silicon photonic delay lines,” *Opt. Express*., vol. 19, no. 12, pp. 11780-11785, June. 2011.

[24] I. Giuntoni, D. Stolarek, D. I. Kroushkov, J. Bruns, L. Zimmermann, B. Tillack, and K. Petermann, “Continuously tunable delay line based on SOI tapered Bragg gratings,” *Opt. Express.,* vol. 20, no. 10, pp.11241–11246, May. 2012.

[25] M. Burla, D. Marpaung, L. Zhuang, C. Roeloffzen, M. R. Khan, A. Leinse, M. Hoekman, and R. Heideman, “On-chip CMOS compatible reconfigurable optical delay line with separate carrier tuning for microwave photonic signal processing,” *Opt. Express.*, vol. 19, no. 22, pp. 21475–21484, Oct. 2011.

[26] M. Pu, L. Liu, W. Xue, Y.Ding, L.H. Frandsen, H. Ou, K. Yvind, and J. Hvam, “Tunable Microwave Phase Shifter Based on Silicon-on-Insulator Microring Resonator,” *IEEE Photon. Technol. Lett,* vol. 22, no.12, pp. 869-871, Jun. 2010.

[27] M. Pu, L. Liu, W. Xue, Y. Ding, H. Ou, K. Yvind, and J. M. Hvam, “Widely tunable microwave phase shifter based on silicon-on-insulator dual-microring resonator,” *Opt. Express*, vol. 18 , no 6, pp. 6172-6182, Mar. 2010.

[28] Q. Chang, Q. Li, Z. Zhang, M. Qiu, T. Ye, and Y. Su, “A Tunable Broadband Photonic RF Phase Shifter Based on a Silicon Microring Resonator,” *IEEE Photon. Technol. Lett.*, vol. 21, no .1, pp. 60–62, Jan. 2009.

[29] M. H. Khan, H. Shen, Y. Xuan, L. Zhao, S. Xiao, D. E. Leaird, A. M. Weiner, and M. Qi, “Ultrabroad-bandwidth arbitrary radiofrequency waveform generation with a silicon photonic chip-based spectral shaper,” *Nature. Photon*, vol. 4, no. 2, pp.117–122, Feb. 2010.

[30] H. Shao, H. Yu, X. Li, Y. Li, J. Jiang, H. Wei, G. Wang, T. Dai, Q. Chen, J. Yang, and X. Jiang, “On-chip microwave signal generation based on a silicon microring modulator,” *Opt. Lett*., vol. 40, no. 14, pp. 3360-3363, July. 2015.

[31] A. M. Guti´errez, A. Brimont, J. Herrera,M. Aamer, J.Mart´ı, D. J. Thomson, F. Y. Gardes, G. T. Reed, J. M. Fedeli, and P. Sanchis, “Silicon slow-light-based photonic mixer for microwave-frequency conversion applications,” *Opt. Lett*, vol.37, no. 10, pp. 1721–1723, May. 2012.

[32] Y. Jiang, W. Jiang, X. Chen, L. Gu, B. Howley, and R. T. Chen, "Nano-Photonic Crystal Waveguides for Ultra-Compact Tunable True Time Delay Lines", *Proc. SPIE 6182, Photonic Crystal Materials and Devices III*, vol. 5733, pp. 166-175, Apr. 2005.

[33] M. S. Rasras, K. Y. Tu, D. M. Gill, Y. K. Chen, A. E. White, S. S. Patel, A. Pomerene, D. Carothers, J. Beattie, M. Beals, J. Michel, and L. C. Kimerling, "Demonstration of a Tunable Microwave-Photonic Notch Filter Using Low-Loss Silicon Ring Resonators", *J. Lightw. Technol*, vol. 27, no. 12, pp. 2105–2110, Jun. 2009.

[34] M. Rasras, D. Gill, S. Patel, K. Y. Tu, Y. K. Chen, A. White, A. Pomerene, D. Carothers,M. Grove, D. Sparacin, J. Michel, M. Beals, and L. Kimerling, "Demonstration of a fourth-order pole-zero optical filter integrated using CMOS processes," *J. Lightw. Technol*., vol. 25, no. 1, pp. 87-92, Jan. 2007.

[35] J. Cardenas,M.A. Foster, N. Sherwood-Droz,C.B. Poitras, H. L. R. Lira, B. Zhang, A. L. Gaeta, J. B. Khurgin, P. Morton, andM. Lipson, "Wide-bandwidth continuously tunable optical delay line using silicon microring resonators," *Opt. Express*., vol. 18, no. 25, pp. 26525–26534, Dec. 2010.

[36] P. Toliver, R. Menendez, T. Banwell, A. Agarwal, T. K. Woodward, N. N. Feng, P. Dong, D. Feng, W. Qian, H. Liang, D. C. Lee, B. J. Luff, and M. Asghari, "A programmable optical filter unit cell element for high resolution RF signal processing in silicon photonics," *Optical Fiber Communication Conference* , paper OWJ4. 2010.

[37] P. Dong, N. N. Feng, D. Feng, W. Qian, H. Liang, D. C. Lee, B. J. Luff, T. Banwell, A. Agarwal, P. Toliver, R. Menendez, T. K.Woodward, andM. Asghari, "GHz-bandwidth optical filters based on high order silicon ring resonators," *Opt. Express*., vol.18, no. 23, pp. 23784–23789, Nov. 2010.

[38] Y. Ding, C. Peucheret, J. Xu, H. Hou, X. Zhang, and D. Huang, "ultra-wide band signal generation using a silicon micro ring resonator," in: *Proceedings of the 2011 IEEE Photonics Conference*, Arlington, VA, USA, pp.258–259. 2011.

[39] P. A. Morton, J. Cardenas, J. B. Khurgin, and M. Lipson, "Fast Thermal Switching of Wideband Optical Delay Line With No Long-Term Transient," *IEEE Photon. Technol. Lett*., vol. 24, no.6, pp. 512–514, Mar. 2012.

[40] J. Dong, Li Liu, D. Gao, Y. Yu, A. Zheng, T. Yang, X. Zhang, "Compact Notch Microwave Photonic Filters Using On-Chip Integrated Microring Resonators," *IEEE photon. J.*, vol. 5, no. 2, pp. 5500307, Apr. 2013.

[41] José Capmany, David Domenech, and Pascual Muñoz, "Silicon graphene waveguide tunable broadband microwave photonics phase shifter," *Opt. Express*., vol. 22, no. 7 pp. 80947 -8100. Apr. 2014.

[42] J. Wang1, H. Shen, L. Fan, R. Wu, B. Niu, L. T. Varghese, Y. Xuan, D. E. Leaird, X. Wang, F. Gan, A. M. Weiner and M. Qi, "Reconfigurable radio-frequency arbitrary waveforms synthesized in a silicon photonic chip," *Nat. Commun*., 6:5957 doi: 10.1038/ncomms6957. 2015.

[43] H. H. Li. "Refractive index of silicon and germanium and its wavelength and temperature derivatives," *J. Phys. Chem. Ref. Data*., vol. 9, no.3, pp. 561-658, Dec. 1979.

[44] C. Z. Tan and J. Arndt. "Temperature dependence of refractive index of glassy SiO2 in the infrared wavelength range," *J. Phys. Chem. Solids*., vol. 61, no. 8, pp. 1315–1320, Aug. 2000.

[45] I. Giuntoni, D. Stolarek, D. I. Kroushkov, J. Bruns, L. Zimmermann, B. Tillack, and K. Petermann, "Continuously tunable delay line based on SOI tapered Bragg gratings," *Opt. Express*., vol. 20, no. 10, pp. 11241–11246, May. 2012.

[46] M. Gnan, S. Thorns, D. Macintyre, R. De La Rue, and M. Sorel, "Fabrication of low-loss photonic wires in silicon -on-insulator using hydrogen silsesquioxane electron beam resist," *Electron. Lett*., vol. 44, no. 2, pp. 115–116, Jan. 2008.

[47] W. Bogaerts. et.al, "Nano-photonic waveguides in silicon on insulator fabricated with CMOS technology," *J. Lightw. Technol*., vol. 23, no. 1, pp. 401-412, Jan. 2005.

[48] A. Yariv. "Coupled-mode theory for guided-wave optics," *IEEE J. Quantum Electron*., vol. QE-9, no. 9, pp. 919–933. Sep.1973

[49] W. Bogaerts et al, "Silicon microring resonators," *Laser Photonics Rev*., vol. 6, no. 1, pp. 47–73, Jan. 2012.

[50] X. Chen, C. Li and H. K. Tsang, "Device engineering for silicon photonics," *NPG ASIA MATERIALS*., vol. 3, no. 1, pp. 34-40, Jan. 2011.

[51] W. Li, M. Li, and J. P. Yao, "A narrow-passband and frequency-tunable microwave photonic filter based on phase-modulation to intensity-modulation conversion using a

phase-shifted fiber Bragg grating," *IEEE Trans. Microw. Theory Tech*., vol. 60, no. 5, pp. 1287-1296, May 2012.

[52] J. Mora, L R Chen, and J. Capmany, "Single-bandpass microwave photonic filter with tuning and reconfiguration capabilities," *J. Lightw. Technol*., vol. 26, no. 15, pp. 2663-2670, Aug. 2008.

[53] F. Zeng and J. P. Yao, "Investigation of phase modulator based all optical bandpass microwave filter," *J. Lightw. Technol*., vol. 23, no. 4, pp. 1721–1728, Apr. 2005.

[54] Q. Xu and M. Lipson, "Carrier-induced optical bistability in silicon ring resonators," *Opt. Lett*., vol. 31, no. 3, pp.341-343, Feb. 2006.

[55] L. W. Luo, G. S. Wiederhecker, K. Preston, and M. Lipson, "Power insensitive silicon microring resonators," *Opt. Lett*., vol. 37, no. 4, pp.590-592, Feb. 2012.

[56] M. Ahmad, G. Papaioannou, R. Plana, and P. Russer, "Bandpass filter modeling employing Lorentzian distribution," *Microwave Opt. Technol. Lett*., vol. 51, no. 5, pp. 1167-1169, May. 2009.

[57] E. Dulkeith and Y. A. Vlasov, "Self-phase-modulation in submicron silicon-on-insulator photonic wires," *Opt. Express*, vol. 14, no. 12, pp. 5524-5534, June. 2006.

[58] P. E. Barclay, K. Srinivasan, and O. Painter, "Nonlinear response of silicon photonic crystal microresonators excited via an integrated waveguide and fiber taper," *Opt. Express*, vol. 13, no. 3, pp. 801-820, Feb. 2005.

[59] Y. Chen and S. Blair, "Nonlinear phase shift of cascaded microring resonators," *J. Opt. Soc. Am. B.*, vol. 20, no. 10, pp. 2125-2132, Oct. 2003.

[60] F. De Flaviis, "Phase shifters," *Encyclopedia of RF and Microwave Engineering*, Apr. 2005.

[61] H. Shahoei and J. P. Yao, "Tunable microwave photonic phase shifter based on slow and fast light effects in a tilted fiber Bragg grating ," *Opt. Express*. , vol. 20, no. 13, pp. 14009-14014, Jun. 2012.

[62] T. Ido, S. Tanaka, M. Suzuki, M. Koizumi, H. Sano, and H. Inoue, "Ultrahigh- speed multiple-quantum-well electro-absorption optical modulators with integrated waveguides," *J. Lightw. Technol*., vol. 14, no. 9, pp. 2026-2034, Sep. 1996.

[63] K. Noguchi, O. Mitomi, and H. Miyazawa, “Millimeter-wave Ti: Linbo3 optical modulators," *J. Lightw. Technol*., vol. 16, no. 4, pp. 615-619, Apr. 1998.

[64] M. Lipson, “Compact Electro-Optic Modulators on a Silicon Chip,” *IEEE J. Sel. Topics Quantum Electron*., vol. 12, no. 6, pp. 1520-1526, Dec. 2006.

[65] R. Soref, “Electro-optical and nonlinear optical coefficients of ordered group IV semiconductor alloys,” *J. Appl. Phys*., vol. 72, no. 2, pp. 626-630, Jul. 1992.

[66] R. Soref and B. Bennett, “Electro-optical effects in silicon,” *IEEE J. Quantum Electron*., vol. 23, no. 1, pp. 123-129, Jan. 1987.

[67] D. J. Thomson, F. Y. Gardes, J.-M. Fedeli, S. Zlatanovic, H. Youfang, B. P. P. Kuo, E. Myslivets, N. Alic, S. Radic, G. Z. Mashanovich, and G. T. Reed, “50-Gb/s Silicon Optical Modulator,” *IEEE Photon. Technol. Lett.*, vol. 24, no. 4, pp. 234–236, Feb. 2012.

[68] Q. Xu, B. Schmidt, S. Pradhan, and M. Lipson, “Micro-meter-scale silicon electro-optic modulator,” *Nature. Photon*, vol. 435, no. 7040, pp. 325-327, May. 2005.

[69] J. C. Rosenberg, W. M. Green, S. Assefa, T. Barwicz, M. Yang, S. M. Shank, and Y. A. Vlasov, “Low-power 30 Gbps silicon microring modulator,” *in Conf. on Lasers and Electro-Optics*. Optical Society of America, p. PDPB9. 2011.

[70] W. D. Sacher, W. Green, S. Assefa, T. Barwicz, H. Pan, S. Shank, Y. Vlasov, and J. Poon, “28 Gb/s silicon microring modulation beyond the linewidth limit by coupling modulation,” *in Optical Fiber Communication Conf*. Optical Society of America, p. OM3J.2, 2012.

[71] M. R. Watts, D. C. Trotter, R. W. Young, and A. L. Lentine, “Ultralow power silicon micro-disk modulators and switches,” *in Proc. 5th IEEE Int. Conf. Group IV Photonics*. *IEEE*, pp. 4 -6, 2008.

[72] A. Krishnamoorthy, K. Goossen, W. Jan, X. Zheng, R. Ho, G. Li, R. Rozier, F. Liu, D. Patil, J. Lexau et al., “Progress in low-power switched optical interconnects,” *IEEE J. Sel. Topics Quantum Electron*., vol. 17, no. 2, pp. 357-376, Apr. 2011.

[73] Q. Xu, S. Manipatruni, B. Schmidt, J. Shakya, and M. Lipson, “12.5 Gbit/s carrier-injection-based silicon micro-ring silicon modulators,” *Opt. Express*., vol. 15, no. 2, pp. 430-436, Jan. 2007.

[74] R. A. Soref, P. J. Lorenzo, “All-silicon active and passive guided-wave components for λ=1.3 and 1.6 μm*,” IEEE J. Quantum Electron*., vol.QE-22, no. 6, pp. 873-879, Jun. 1986.

[75] A. Liu, R. Jones, L. Liao, D. Samara-Rubio, D. Rubin, O. Cohen, R. Nicolaescu, M. Paniccia, “A high-speed silicon optical modulator based on a metal-oxide-semiconductor capacitor,” *Nature. photon*, vol. 427, pp. 615-618, Feb. 2004.

[76] F. Y. Gardes, G. T. Reed, N. G. Emerson, C. E. Png, “A sub-micron depletion-type photonic modulator in Silicon on Insulator,” *Opt. Express*., vol. 13, no. 22, pp. 8845-8853, Oct. 2006.

[77] L. Chrostowski, M. Hochberg, “Silicon Photonics Design,” *Cambridge University Press.*, Chapter. 6, pp.217-258, 2015.

[78] J. Mu¨ller, F. Merget, S. Sharif Azadeh, J. Hauck, S. Romero Garcı´a, B. Shen & J. Witzens, “Optical Peaking Enhancement in High-Speed Ring Modulators,” *Sci. Rep*. vol. 4, pp. 1-8, Sep. 2014.

[79] A. Ayazi, T. Baehr-Jones, Y. Liu,1 A. Eu-Jin Lim and M. Hochberg, “Linearity of silicon ring modulators for analog optical links,” *Opt. Express*, vol. 20, no. 12, pp. 13115-13122, May. 2012.

[80] B. Vidal, V. Polo, J. L. Corral, and J. Martı´, “Photonic microwave filter with tuning and reconfiguration capabilities using optical switches and dispersive media,” *Electron. Lett*. vol. 39, no. 6, pp. 547–549, Mar. 2003.

[81] B. Pile1 and Geoff Taylor, “Small-signal analysis of microring resonator modulators,” *Opt. Express.*, vol. 22, no. 12, pp. 14913-14928, Jun. 2014.

[82] J. Wang, F. Zeng, and J. Yao, “All –optical microwave band-pass filter with negative coefficients based on PN-IM conversion,” *IEEE Photon. Technol. Lett.*, vol. 17, no. 10, pp. 2176-2178, Oct. 2005.

[83] A. Wiberg, P. P-Millán, M. V. Andrés, and P. O. Hedekvist, “Microwave-photonic frequency multiplication utilizing optical four-wave mixing and fiber Bragg gratings,” *J. Lightw. Technol*., vol. 24, no. 1 pp. 329–334, Jan. 2006.

[84] Q. Wang, H. Rideout, F. Zeng, and J. P. Yao, “Millimeter-wave frequency tripling based on four-wave mixing in a semiconductor optical amplifier,” *IEEE Photon. Technol. Lett.*, vol. 18, no. 23, pp. 2460-2462, Dec. 2006.

[85] J. Leuthold, C. Koos and W. Freude, “Nonlinear silicon photonics,” *Nature Photon*., vol. 4, pp. 535 – 544, Jul. 2010.

[86] D. Dimitropoulos, V. Raghunathan, R. Claps, and B. Jalali, “Phase-matching and nonlinear optical processes in silicon waveguides,” *Opt. Express,* vol.12, no.1, pp. 149-160, Jan. 2004.

[87] Turner, A. C., Manolatou, C., Schmidt, B. S., Lipson, M., Foster, M. A., Sharping, J. E., and Gaeta, A. L., “Tailored anomalous group-velocity dispersion in silicon channel waveguides,” *Opt. Express*., vol. 14, no. 10, pp. 4357-4362, May. 2006.

[88] H. Rong, Y. Kuo, A. Liu, and M. Paniccia, “High efficiency wavelength conversion of 10 Gb/s data in silicon waveguides,” *Opt. Express.,* vol. 14, no. 13, pp. 1182-1188, Feb, 2006.

[89] T. J. Kippenberg, R. Holzwarth, and S. A. Diddams, “Micro-resonator-Based Optical Frequency Combs,” *Science*., vol. 332, pp. 555–559, Apr. 2011.

[90] N. Takachio, H. Suzuki, M. Fujiwara, J. Kani, K. Iwatsuki, H. Yamada, T. Shibata, and T. Kitoh, “Wide area gigabit access network based on 12.5 GHz spaced 256 channel super-dense WDM technologies,” *Electron. Lett*., vol. 37, no. 5, pp. 309–311, Mar. 2001.

[91] Z. Jiang, C. B. Huang, D. E. Leaird, and A. M. Weiner, "Optical arbitrary waveform processing of more than 100 spectral comb lines," *Nature. Photon*., vol. 1, pp. 463-467, Aug. 2007.

[92] C.-B. Huang, D. E. Leaird, A. M. Weiner, “Time-multiplexed photonically enabled radio frequency arbitrary waveform generation with 100 ps transitions,” *Opt. Lett*., vol. 32, no. 22, pp. 3242-3244, Nov. 2007.

[93] M. Ziyadi, et al, “Tunable radio frequency photonics filter using a comb-based optical tapped delay line with an optical nonlinear multiplexer,” *Opt. Lett*., vol. 40, no. 14, pp. 3284-3287, Jul. 2015.

[94] R. Wu, V. R. Supradeepa, C. M. Long, D. E. Leaird, and A. M. Weiner, “Generation of very flat optical frequency combs from continuous-wave lasers using cascaded intensity and phase modulators driven by tailored radio frequency waveforms,” *Opt. Lett*., vol 35 , no. 19, pp. 3234-3236, Oct. 2010.

[95] Y. Dou, H. Zhang, and M. Yao, “Generation of Flat Optical-Frequency Comb Using Cascaded Intensity and Phase Modulators,” *IEEE Photon. Technol. Lett.*, vol. 24, no. 9, pp. 727-729, May. 2012.

[96] M. A. Foster, J. S. Levy, O. Kuzucu, K. Saha, M. Lipson, and A. L. Gaeta, “Silicon-based monolithic optical frequency comb source,” *Opt. Express*., vol. 19, no. 15, pp. 14233–14239, Jul. 2011.

[97] F. Ferdous, H. Miao, D. E. Leaird, K. Srinivasan, J. Wang, L. Chen, L. T. Varghese, and A. M.Weiner, “Spectral line-by-line pulse shaping of on-chip micro-resonator frequency combs,” *Nature Photon*., vol. 5, pp. 770–776, Dec. 2011.

Publication List:

1. **N. Ehteshami**, W. Zhang, and J. P. Yao, "Optically tunable full 360^{o} microwave photonic phase shifter using three cascaded silicon-on-insulator microring resonators," *Opt. Comm.*, accepted.

2. **N. Ehteshami**, W. Zhang, and J. P. Yao, "Optically tunable single passband microwave photonic filter based on phase-modulation to intensity-modulation conversion in a silicon-on-Insulator microring resonator," MWP2015, 26-29 Oct. 2015, Paphos, Cypru.

3. W.Zhang, **N. Ehteshami**, W. Liu, and J. P. Yao, "Silicon-based on-chip electrically tunable sidewall-Bragg-grating Fabry-Perot filter," *Opt. Lett.*, vol. 40, no. 19, pp. 3153-3156, Jul.2015.